INSTITUTE OF SPACE AND ASTRONAUTICAL SCIENCE
YOSHINODAI, CHUO, SAGAMIHARA, KANAGAWA 252-5210

ISAS RESEARCH NOTE

ISAS RN 875

X-ray Study on Extended Emissions from Radio Lobes of Active Galaxies

Hiromi Seta

February 2013

Department of Physics, Rikkyo University
3-34-1 Nishi-Ikebukuro, Toshima, Tokyo, 171-8501, Japan
seta@rikkyo.ac.jp

Reproduced from the thesis submitted to
Saitama University for
the Degree of Doctor of Science (Physics)
March, 2012

X-ray Study on Extended Emissions from Radio Lobes of Active Galaxies

Hiromi Seta

Department of Physics, Graduate School of Science & Engineering,
Saitama University
255 Shimo-Okubo, Sakura, Saitama, 338-8570, Japan
seta@heal.phy.saitama-u.ac.jp

Thesis submitted to the Department of Physics,
Graduate School of Science & Engineering, Saitama University
on February 17, 2012
in partial fulfillment of the requirements
for the degree of Doctor of Philosophy in physics

March 3, 2012

Abstract

Jets, which emit from active galactic nuclei (AGN), product a mount of energy into the universe. The understanding of the mechanism of the activity of the AGN jet is quite important to reveal the nature not only of AGN but also of several effect such as cooling flow in the galaxy and the re-ionization of the universe. However it is very difficult to observe the AGN activity because the variability is very long scale, which is much longer beyond a human time scale. With an appropriate choice of object, we can unveil a part of the time-varying nature of the AGN jet.

We present the results of two different objects in two different view points: an differential and integral view of the time-varying quantities. The former is blazar OJ 287, which is suggested the binary black hole. The latter is radio lobe Fornax A, which is one of the nearest and brightest radio lobes. The highlights of the results are (1) from the results of OJ 287, the detection of the difference of the periodic flares, (2) from the results of Fornax A, the discovery of the thermal diffuse emission in the radio lobe, and (3) from the results of Fornax A, the observation of the difference of the physical parameters in the parts of the lobe. Finally, we interpret the jet activity combined with these results of OJ 287 and Fornax A.

Contents

List of Figures

List of Tables

Chapter 1

Introduction

The jet from active galactic nucleus (AGN) is one of the most gigantic feature of energy concentration and release in the universe. At the center of AGNs lies a super massive black hole (10^7-10^9 $M_\odot$), which powers the jet fueled by mass accretion. The jet with a relativistic velocity releases a massive amount of energy in the intergalactic medium while the super massive black hole exhibits AGN activities. However, the life time and the duty cycle of jet is not determined by observational study.

In the universe, the thought to be two types of black holes; Galactic stellar mass (~ 10 $M_\odot$) black holes and super massive black holes. From the observational point of view, the largest difference is in the time scale of evolution, the scale of Galactic black holes is in the order of weeks to years, while the scale of super massive black holes is much longer beyond a human time scale, reflecting the > 6 orders of magnitudes difference in mass. Because of the rapid variability and the brightness, Galactic black holes have been studied deeply about their evolution. On the other hand, the long time scale of variation and faintness make it difficult to study the evolution of the super massive black holes.

The power of the AGNs is suggested to be a key in order to reveal the history of the universe. In the age of the re-ionization of the universe, it is considered that the large radiation of the AGNs caused the neutral hydrogen ionization to divide the electrons and protons. When the AGN jets emit long distances, it is suggested that the energy of motion of the AGN jet caused to the ionization in the intergalactic space. The power of the AGN is important to understand the history of the universe. However, we cannot understand that amount of the AGN power contribute in the evolution of the universe. We wonder how much

energy the AGN input into the universe. We wonder how long time the AGN jets emit in the active time. We wonder whether the jet emitting time is continual or intermissive. These parameters are important for understanding of the re-ionization of the universe.

However, with an appropriate choice of object, we can unveil a part of the time-varying nature of the AGN jet. In this thesis, we study two different objects in two different view points: an differential and integral view of the time-varying quantities. The former is a blazar, which change its activity periodically in a human time scale. The latter is a radio lobe, in which the energy injection by jet is accumulated. The combination of the two complementary view points can reveal the history of the AGN jet activity.

Chapter 2

Review

Contents

2.1 Jets from Active Galactic Nucleus (AGNs)

In the universe, some of galaxies produce very high luminosity in a very concentrated region. They are called as active galactic nuclei's (AGNs). The AGNs are observed brightly across a wide range of wavelength; in radio, optical, infrared, X-ray, and γ-ray. Based on their high bolometric luminosity (10^{40-46} erg s^{-1}) and rapid variability with a scale of days, the center of the AGNs is thought to host a super massive black hole. The mass of the black hole is estimated to be $10^{7-9} M_{\odot}$

The AGNs are classified into two types depending on the radio brightness: radio-loud galaxies and radio-quiet galaxies. The radio intensity of radio-loud galaxies is about 100–

1000 times as high as that of radio-quiet galaxies. Radio-loud galaxies account for about 10% of AGNs, and have a collimated plasma outflow called jet.

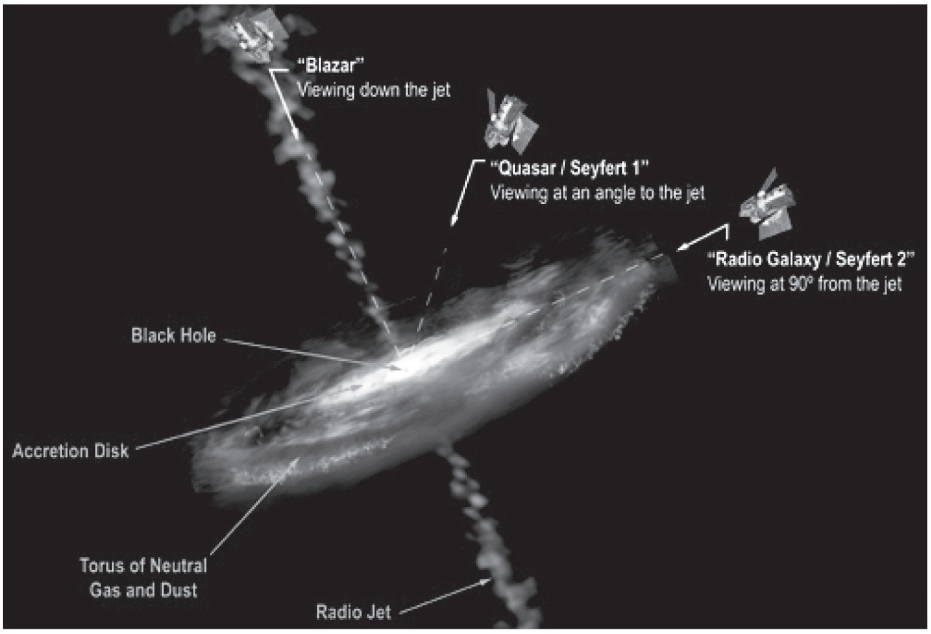

Figure 2.1: Picture of the classification of the radio-loud galaxy.

Figure 2.1 shows the observable features of radio-loud galaxies. Radio-loud galaxies have different features depending on with the direction of observations. An AGN consists of a black hole, an accretion disk, and a thick plasma called torus. When we observe in the edge-on direction, we can observe a double sided jet. When we observe in the face-on direction, we can observe a beaming jet as a compact source, which is called a blazar.

2.1.1 Radiation Mechanism

The jet contains a large amount of the relativistic electrons. Due to interact between these electrons and circumference plasma, non-thermal radiation is processed. We summarize the basics of the radiation processes: synchrotron radiation and inverse Compton radiation. These processes are important tools to estimate the energetics in the radio galaxies.

2.1.1.1 Synchrotron Radiation

Relative electrons interacting with a magnetic field B radiates emissions via synchrotron radiation. The total emitted power per frequency is

$$P(\nu) = \frac{\sqrt{3}q^3 B \sin\theta}{2\pi mc^2} F(\frac{\nu}{\nu_c}) \text{ [erg s}^{-1}\text{Hz}^{-1}\text{]}. \tag{2.1}$$

Here the q and m are a charge and a mass of an electron, respectively. θ is an angle between the magnetic field and the electron velocity. The $F(x)$ function is

$$F(x) \equiv x \int_x^\infty K_{\frac{5}{3}}(\xi) d\xi, \tag{2.2}$$

, where the function $K_{\frac{5}{3}}$ is Bessel function of an order 5/3. The cut-off frequency ν_c is

$$\nu_c = \frac{3\gamma^2 qB}{4\pi mc} \sin\theta \text{ [Hz]}. \tag{2.3}$$

Since the peak of $F(x)$ is around $x = 0.29$, the peak frequency of the synchrotron spectrum is

$$\nu = 0.29\nu_c = 120 \left(\frac{\gamma}{10^4}\right) \left(\frac{B}{1\ \mu\text{G}}\right) \sin\theta \text{ [MHz]} \tag{2.4}$$

For an isotropically distributed electrons with γ, we obtain the synchrotron power from one electron, which is obtained by integrating equation 2.1 over the frequency and the pitch angle,

$$P_{\text{SR}} = \frac{4}{3}\sigma_{\text{T}} c\gamma^2 u_{\text{m}} \text{ [erg s}^{-1}\text{]}. \tag{2.5}$$

2.1.1.2 Inverse Compton Scattering

Relativistic electrons scattered by photons radiate inverse Compton emission. The total power emitted in the observer's frame can be described as

$$P_{\text{e}} = \sigma_{\text{T}} c\gamma^2 \left(1 + \frac{1}{3}\beta\right) u_{\text{ph}}. \tag{2.6}$$

σ_{T} is the Thomson cross section, γ is the electron energy in the unit of mc^2, and $\beta = \frac{v}{c}$. The energy density of the seed photons u_{ph} is

$$u_{\text{ph}} = \int \epsilon n(\epsilon) d\epsilon. \tag{2.7}$$

The power of the inverse Compton radiation, is

$$P_{\rm IC} = \frac{4}{3}\sigma_{\rm T} c \gamma^2 u_{ph}. \tag{2.8}$$

Comparing equation 2.5 with equation 2.8, we have a general relation.

$$\frac{P_{\rm SR}}{P_{\rm IC}} = \frac{u_{\rm m}}{u_{\rm ph}}. \tag{2.9}$$

2.1.2 Energy Loss Rate

When the electrons interact with magnetic fields, radiation field, and thermal plasma, they loss their energy. We show four cooling processes: (1) Synchrotron cooling, (2) Inverse Compton cooling, and (3) bremsstrahlung.

When the electrons interact with magnetic fields, they emit synchrotron radiation (Rybicki & Lightman 1979). The fractional loss rate of the synchrotron radiation $b_{\rm sync}$ is

$$b_{\rm sync} = \frac{4\sigma_{\rm T}\gamma^2 u_{\rm m}}{3 m_e c} = 1.29 \times 10^{-21} \frac{B}{10^{-6}}^2 \gamma^2 \ [s^{-1}], \tag{2.10}$$

where $u_{\rm m}$ is the density of the magnetic field and $\sigma_{\rm T}$ is the Thomson cross section. When the electrons interact with radiation fields, they emit inverse Compton radiation (Rybicki & Lightman 1979).

$$b_{\rm IC} = \frac{4\sigma_{\rm T}\gamma^2 u_{\rm ph}}{3 m_e c} = 3.24 \times 10^{-8} \gamma^2 U_{\rm ph} \ [s^{-1}], \tag{2.11}$$

where $u_{\rm ph}$ is the photon density of up-scattered. If we assume that $U_{\rm ph}$ is the cosmic microwave background (CMB), the density of CMB $U_{\rm CMB}$ of $4.1 \times 10^{-13}(1+z)^4$ erg cm^{-3} yields,

$$b_{\rm IC} = 1.33 \times 10^{-20} \gamma^2 U_{\rm ph} (1+z)^4 \ [s^{-1}]. \tag{2.12}$$

Also the electron suffers the loss by bremsstrahlung emission. The fractional energy loss rate of bremsstrahlung is

$$b_{\rm brems} \simeq 1.5 \times 10^{-16} n_e \gamma [\ln \gamma + 0.36] \ [s^{-1}]. \tag{2.13}$$

2.2 Objects

2.2.1 Blazars

2.2.1.1 History

The blazars are objects, in which the direction of the jet is aligned with the sight of observers. Since the jet propagates at a relativistic velocity, we can observe the jet near the nucleus (0.001–0.1 pc), using the relativistic beaming effect. By this effect, blazars are very bright in multi-wavelengths.

2.2.1.2 Classification

The multi-wavelength spectral energy distribution (SED) of blazar indicates that the spectrum has two peaks. The relative height of the two peaks differ from object to object(figure 2.2). Blazars are classified using the frequency of the low energy peak. Blazars have the peak, which a peak in the IR/optical band are called LBLs (low-energy peaked BL Lacs), while the blazars with a peak in the UV/X-ray band are called HBLs (high-energy peaked BL Lacs). The difference is explained by different electron Lorentz factors.

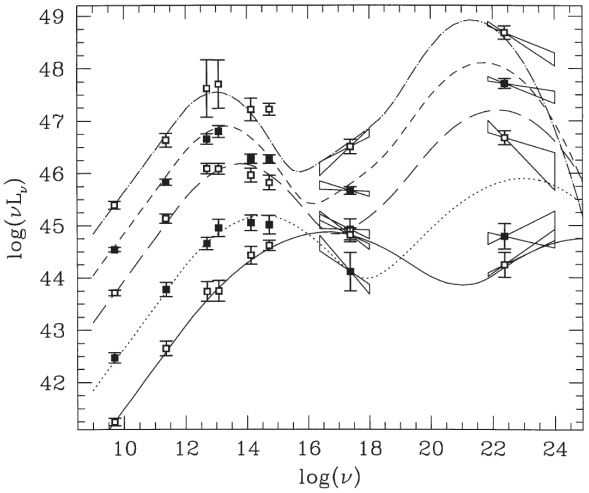

Figure 2.2: SEDs of some representative blazars. (Fossati et al. 1998).

2.2.1.3 Emission mechanism

In general, the SED of blazars is characterized by two broad humps (e.g., Fossati et al. 1998); the low-energy component, with wavelengths from radio to ultraviolet and X-rays, is widely regarded as synchrotron radiation (SR) from relativistic electrons within the jet. The high-energy component, with wavelengths from X-rays to γ-rays, is interpreted as inverse-Compton scattering. In one of the simple emission models named "synchrotron self-Compton (SSC) model", relativistic electrons scatter SR photons produced by the same population of electrons (e.g., Ghisellini et al. 1998). For LBLs, the SR peak is located in the range between sub-mm and optical wavelengths (Padovani & Giommi 1995). Inverse-Compton scattering in LBLs can emit radiation up to very-high-energy (VHE: E>50 GeV) γ-rays during their optical high states; VHE γ-ray emission has been detected, for example, from BL Lacertae (Albert et al. 2007) and S5 0716+714 (Teshima & The MAGIC Collaboration 2008). These two components usually intersect with each other in the X-ray band (e.g., Giommi et al. 1999). Therefore, the X-ray spectrum of LBLs should be highly sensitive to the change of the magnetic field (B) and/or the maximum Lorentz factor ($\gamma_{\rm max}$) of the electrons, since the SR peak scales as $\propto B\gamma_{\rm max}^2$. In fact, the X-ray spectrum of the object, obtained in previous observations, can be successfully interpreted on the basis of the interplay between the SR and the inverse-Compton component (Idesawa et al. 1997; Isobe et al. 2001).

2.2.2 Radio lobes

2.2.2.1 History

The first discovery of the jet was made in the optical in the galaxy M87 (Curtis 1918). The radio galaxy Cygnus A was detected by radio in 1944 (Reber 1944). After that, the radio observations for the radio galaxies have been performed intensively. Radio galaxies emit a jet, which produces a shock with the interstellar galaxy medium. The point of the shock is called a hotspot. After the shock, the electrons and protons, which are carried by the jet, expand in a the interstellar galaxy space. This extended structure, which is called a radio lobe, is size of few to several Mpc. The radio lobe is the storage of the energy carried by the jet.

2.2.2.2 Classification

The radio galaxies are classified into types depending on the morphology of the radio lobe. Fanaroff & Riley (1974) defined the classification using the ratio of the distance between the regions of highest radio brightness in both sides of the central galaxy, to the total extent of the radio lobe measured from the lowest contour. The sources with a ratio less than 0.5 are called FR I type, while the sources with a ratio more than 0.5 are called FR II type. The characteristics of the FR I include a bright jet and an obscure hot spot, while those of the FR II include an obscure jet and a bright hot spot. In general, the lobe of the FR II type galaxies is brighter in radio and X-ray than that of the FR I. The cause for this difference is unknown.

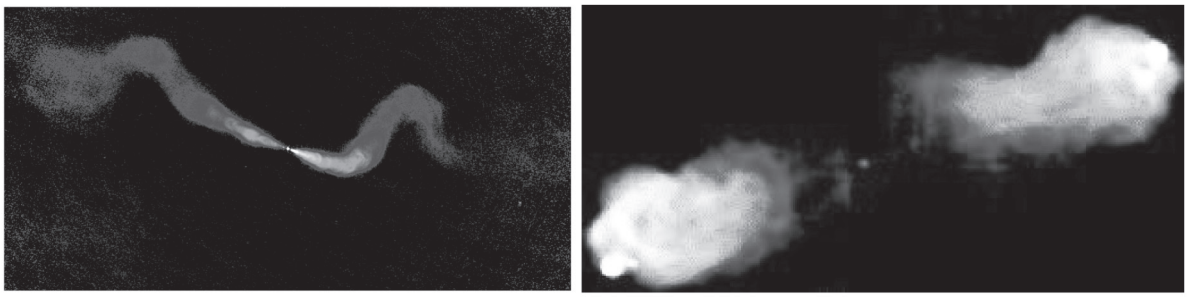

Figure 2.3: Radio image of radio galaxies, FR I type (left, 3C 31) and FR II type (right, Cygnus A) (http://ned.ipac.caltech.edu/).

2.2.2.3 Radiative mechanism

The radio lobes are observed by synchrotron radiation and inverse Compton emission. Since the lobes are extended in a large scale, the seed photons of the inverse Compton scattering are the photons of the CMB emission. The energy density of the CMB is precisely known as (Harris & Romanishin 1974)

$$u_{\rm CMB} = 4.1 \times 10^{-13}(1+z)^4 \ [\rm erg\ s^{-1}]. \tag{2.14}$$

We can determine the magnetic field B using observable parameters; redshift z, synchrotron flux density $S_{\rm SR}$ (unit of Jy) at an observed frequency $\nu_{\rm SR}$ (Hz), and inverse Compton flux

density $S_{\rm IC}$ at an observed frequency $\nu_{\rm IC}$,

$$B = \left(5.75 \times 10^{-17} (5.05 \times 10^4)^{\alpha} (1+z)^{\alpha+3} \left(\frac{C(\alpha)}{1.15 \times 10^{31}} \right) \left(\frac{G(\alpha)}{0.5} \right) \frac{S_{\rm SR} \nu_{\rm SR}^{\alpha}}{S_{\rm IC} \nu_{\rm IC}^{\alpha}} \right)^{-(\alpha+1)} f \tag{2.15}$$

Here the function $C(\alpha)$ of radio/X-ray spectral index α is approximately 1.15×10^{31} in $0.5 < \alpha < 2.0$, and the function $G(\alpha)$ is approximately 0.5 in $0.6 < \alpha < 1.0$. We can determine $u_{\rm e}$ between the minimum of electron energy γ_1 and the maximum of that γ_2 as

$$u_e = mc^2 \int_{\gamma_1}^{\gamma_2} \gamma N(\gamma) d\gamma \tag{2.16}$$

$$= 7.69 \times 10^6 \frac{D^2 (1.07 \times 10^3)^{2\alpha+1}}{V(1+z)^2(1-2\alpha)} S_{\rm IC} \left(\frac{\epsilon_{\rm IC}}{1 \text{ keV}} \right)^{\alpha} (\gamma_2^{1-2\alpha} - \gamma_1^{1-2\alpha}) \text{ [erg s}^{-1}] \tag{2.17}$$

Here, the D is the luminosity distance in cm, V is the volume of the lobe in cm^3, and $\epsilon_{\rm IC}$ is the characteristic energy of the IC-boosted X-ray photons.

2.2.2.4 Summary of previous X-ray studies

Using these equations shown in section 2.1 and observable parameters, we can estimate $u_{\rm e}$ and $u_{\rm m}$ from a radio lobe. The emitted jet expands the lobe with a velocity of $0.01c$–$0.1c$ (c is the speed of light), from a size of sub-kpc (e.g., Nagai 2006) to ~ 100 kpc (e.g., Alexander 1987). Thus, the size of the lobe is indicated the age of the lobe. We can investigate the evolution of the accumulated energy in the lobe using several scale lobes. Recently, thanks to Suzaku satellite having a low-background imager, Mpc scale lobes have observed. These radio galaxy is called a giant radio galaxy. We show latest results of the energetics and the evolution of the lobe. This is described in Isobe et al. (2011a,b, 2009)in detail.

Figure 2.4 shows a relation between $u_{\rm e}$ and $u_{\rm m}$ of radio lobes with different sizes of few 10 kpc $\sim$ Mpc. The lobes typically have an electron dominance of $u_{\rm e}/u_{\rm m} = 1$–100, over a wide of range of $u_{\rm e}$ and $u_{\rm m}$. The relation between $u_{\rm e}$ and $u_{\rm m}$ (figure 2.4 left) trend to be distributed in two parts: (a) around the bottom-left corner and (b) around the center. The $u_{\rm m}$ for the giant radio galaxies distributed in such as (a) is indicated to be lower than the CMB energy density (equation 2.14). This suggests that the dominance of radiative loses via Inverse Compton over those via synchrotron radiation is a common properties in the lobes of giant radio galaxies (Ishwara-Chandra & Saikia 1999).

The dependence of $u_{\rm e}$ on the size D of the radio lobes is shown in figure 2.4 left. It has a tight correlation with $u_{\rm e} \propto D^{-1.9 \pm 0.4}$ for the radio galaxies with $D < 900$ kpc (the black

diamond). The size of the lobe is reported to scale roughly as $D \propto \tau$ over a wide range, where τ is the age of the AGN activity. This simple idea is supported by an observed relation $u_{\rm e} \sim E/V \sim D^{-2}$, where V is the volume of the lobe.

On the other hand, in the radio galaxies with $D > 900$ kpc (blue diamond), some giant radio galaxies have lower $u_{\rm e}$ than this relation. For example, an image of the giant radio galaxy DA 240 is shown in figure 2.5. Although the bright hotspot is indicative of a jet activity, this giant radio galaxy, together with others, has a relatively steep synchrotron radio and inverse-Compton X-ray spectra with a photon index $\Gamma = 1.8$–2.0. It indicates that the lobe suffers a strong cooling. Some of them have a very faint core with a luminosity of $\sim 10^{40}$ erg s^{-1}. These indicate that the current energy supply to the lobe is negligible or absent, in comparison to the cooling. In contrast, the giant radio galaxy 3C 457 in figure 2.4 right is located higher than the D-$u_{\rm e}$ relation. The image of the 3C 457, is shown in figure 2.5, which indicates very bright hotspots and a core in radio and X-rays, respectively. The nucleus of 3C 457 is more than three orders of magnitude higher than that of DA 240. These indicate that the current energy supply to the lobe of 3C 457 is on-going.

In the evolution of the radio galaxy, the lobes, which are supplied energy effectively, relate $u_{\rm e} \propto D^{-2}$, while the lobes, which are supplied energy ineffectively, reside lower of the relation. This future is consistent with Fornax A, which is reported to host a dormant nucleus (Iyomoto et al. 1998). Fornax A is found to be lower than the relation.

2.2.2.4.1 High-energy particle acceleration Croston et al. (2009) discovered the high-energy particle acceleration at the termination shock of the lobe. Centaurus A is one of the nearest, largest, and brightest radio galaxies in the sky. Figure 2.6 left shows the X-ray image of Centaurus A. Thanks to the Chandra satellite having the high spatial resolution, a shell-like structure was detected at the edge of the lobe. In the paper, it is described that the region, in which the shock is the strongest and the ambient gas density is the lowest, the inflation of the lobe is accelerating particles to X-ray synchrotron emitting energies, similar to supernova remnants such as SN1006. The lobe expanding velocity is calculated as $\sim$ 2600 km s^{-1}, which corresponds to a Mach number of 8 relative to the ambient medium. From these results, it is expected that the ultra-high energy cosmic ray and TeV emission are produced at Centaurus A (figure 2.6 right).

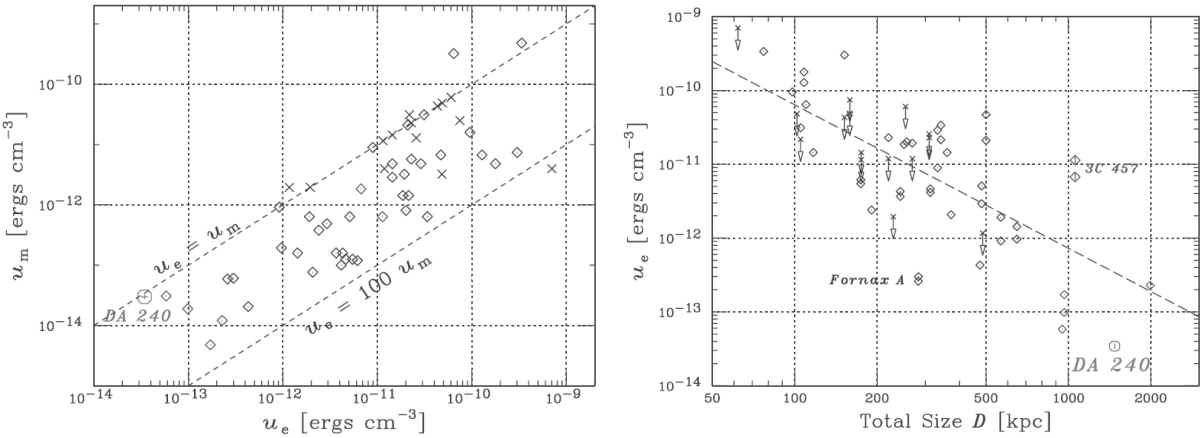

Figure 2.4: Relation between u_e and u_m in lobes of radio galaxies (Isobe et al. 2011a). The lobes, from which a significant inverse-Compton X-ray detection was reported, are plotted with diamonds, while those with only the upper limit on the inverse-Compton flux are shown with crosses. The blue and red symbols indicate giant radio galaxies with a lobe size larger than 1 Mpc. The two dashed lines represent the equipartition and a particle dominance ($u_e/u_m = 1$ and 100), respectively.

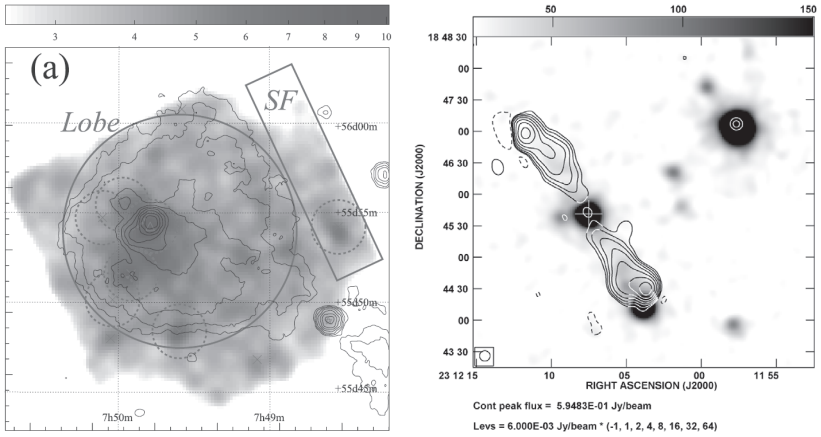

Figure 2.5: The image of the giant radio galaxies, DA 240 (left, Isobe et al. 2011b), 3C 457 (right, Konar et al. 2009). For DA 240, the X-ray intensity, which is obtained with Suzaku, is shown in blue colors, while the radio intensity is shown with contours. The star indicates the position of the nucleus. The red circle and box defined the regions used for the spectral analysis, which are described in the paper in detail. For 3C 457, the X-ray intensity, which is obtained with XMM-Newton, is shown in gray scale, while the radio is shown with contours. The cross indicates the position of the nucleus.

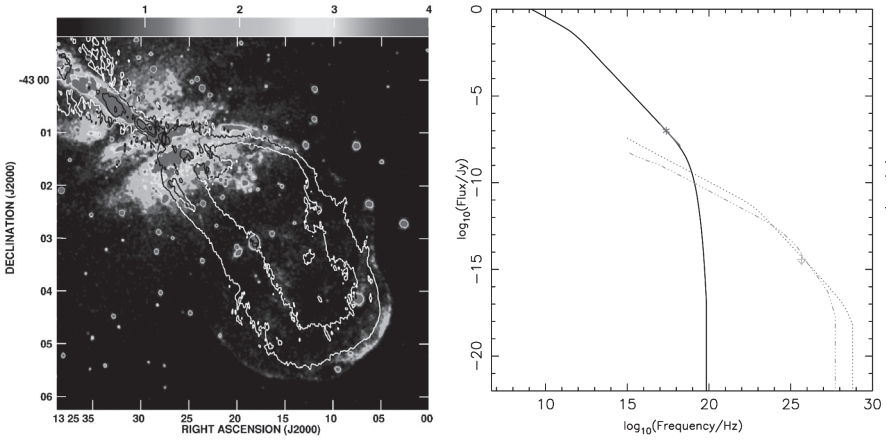

Figure 2.6: X-ray shell image by Chandra (left) and a multi-wavelength spectrum (right) of Centaurus A. In the image, the color scale and contours are X-ray 0.4–2.5 keV band and radio 1.4 GHz intensity, respectively. In the spectrum, the red and green points are X-ray data in the shell region and the upper limit obtained by HESS, respectively. The model predicts the synchrotron radiation (black) and the inverse Compton radiation from scattering of star light (red) and the CMB (blue).

2.2.2.4.2 Weak shock structure in the interacluster medium Some radio galaxies inhabits the center of the cluster of the galaxy. These radio galaxies form the lobes in the hot interacluster medium (ICM). It is suggested that these lobe activity can suppress the cooling flow (Fabian 1994). One of the famous cluster of galaxy having the radio galaxy in the center is Perseus A. Figure 2.7 shows the X-ray image of Perseus A observed from Chandra. The two bubble structures are the lobes, while the surrounding gas is the ICM. The swirl — the edge structures in the north-east outer radio lobe exhibits a surface brightness decrease by 20–30 per cent without any obvious temperature changes. This indicates propagation of weak shocks and viciously dissipating sound wave by the continuous blowing of the lobes Fabian et al. (2003, 2006).

2.3 Questions addressed in thesis

In the above, we have reviewed some aspects of the jet phenomena from super massive black holes (10^7-10^9 $M_\odot$) at the center of AGNs. A vast of knowledge was obtained through intensive studies across wavelengths. The picture of jets depicted in previous studies, however, mostly static. We are interested in jet phenomena and their environmental impacts

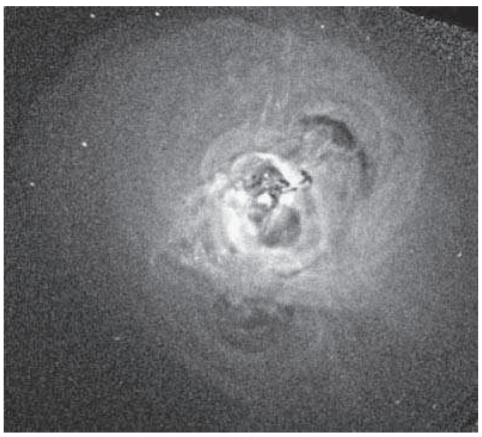

Figure 2.7: Weak shock image of Perseus A.(Fabian et al. 2006)

as time-varying entities. This is quite comparable as a drastic time variation is one of the most distinctive characteristics of jets seen in Galactic stellar mass ($\sim 10\ M_{\odot}$) black holes. The largest difference is in the time scale of evolution; the scale is shorter for the Galactic black holes in the order of weeks to years, but it is much longer beyond a human time scale, reflecting the > 6 orders of difference in mass.

We do consider, however, that it is possible to unveil a part of the time-varying nature of the AGN jets with an appropriate choice of objects. In this thesis, we choose two completely different subjects, which complement with each other with an differential and integral view point of the time-varying quantities. We chose the most appropriate objects in each subject for our study.

One is a blazar, which has a fast time-varying of the jet. We choose OJ287, which is a binary super massive black hole at the center of an AGN. It is known to exhibit changes of the black hole states in a human time scale (or at least in the time scale of this thesis work).

The other is a radio lobe, which is a reservoir of injected energies by the jet integrated over a long span of time. We choose Fornax A, which is the closest, and thus largest in visible size, among radio lobes. The large apparent size allows us to investigate the spatial difference of the energy distributions, in which the jet activities in the recent past may be imprinted.

The plan of this thesis is as follows. In Chapter 3, we summarized to use the astronomical

satellites and the ground-based instruments in the thesis. In Chapter 4 and 5, we described the results of our observations of the binary super massive black hole and the radio lobe. In Chapter 6, we discussed about the obtained results for each sources. Finally in Chapter 7, we combine the results of the two objects to draw a picture bridging the results of the two by considering the jet as a time-varying agent.

Chapter 3

Observing Facilities

Contents

3.1 Suzaku satellite

3.1.1 Overview

The Suzaku satellite is Japan's fifth X-ray astronomical satellite in collaboration with the USA (figure 3.1). Suzaku was launched in 2005 July 10 with a M-V-6 rocket from the Uchinoura Space Center of Japan Aerospace Exploration Agency (JAXA). The satellite orbit is circular with a height of 570 km from the earth with an inclination angle of 31°, and the orbital period is 96 minutes. The spacecraft has a weight of 1706 kg, and a height of 6.5 m. The electric power is $\sim$ 1700 W and $\sim$ 660 W for total and scientific instruments, respectively. The spacecrafts pointing accuracy is $\sim 0.24'$. Because the pointing direction of the telescope is limited by the orientation constraint of the solar paddle, the observable area is 65°–115° from the Sun. Due to earth occultation, the mean observing efficiency of the satellite is 45%. Because of the relatively low altitude, the background environment by charged particles is low and stable. This is one of the unique features of Suzaku, which is not expected in other satellites in a high altitude orbit. Suzaku is thus suited for observations of extended emission of low surface brightness. The detailed performance of Suzaku mission is shown in table 3.1. More details can be found in Suzaku technical description (Suzaku team 2011).

The satellite has three instruments: the X-ray Imaging Spectrometer (XIS; Koyama et al. 2007), which has four sets of X-ray charge-coupled devices (CCD) detectors at the focal plane of four X-ray telescope (XRT) modules (Serlemitsos et al. 2007), the Hard X-ray Detector (HXD; Takahashi et al. 2007; Kokubun et al. 2007), which has GSO crystal scintillators and silicon PIN diodes, the X-ray Spectrometer (XRS; Kelley et al. 2007), which is a microcalorimeter system at the focal plane of another XRT module.

The XRS was the first orbiting X-ray microcalorimeter spectrometer. During the early verification phase, it was demonstrated that the instrument achieved an energy resolution of 6.7 eV in the full width at a half maximum for Mn Kα lines from a calibration source in the orbit. However, due to a failure in the cryogen system, the operation was terminated just before the first light.

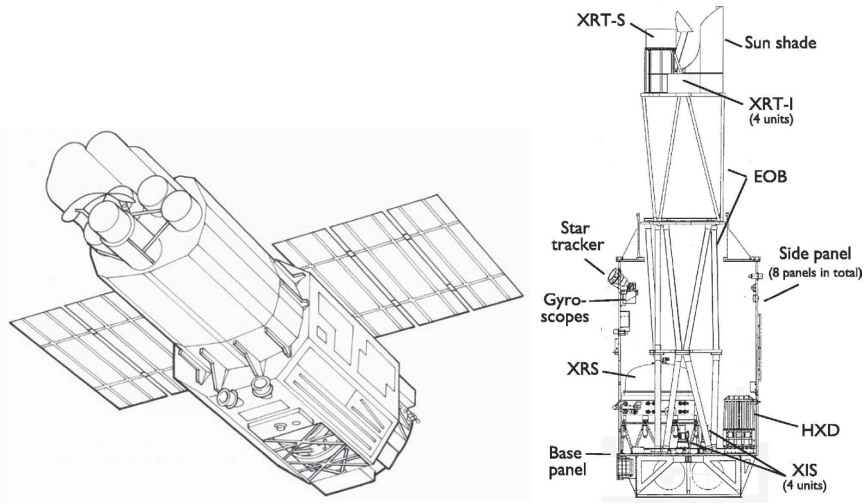

Figure 3.1: Schematic view (left) and of cross-section (right) of Suzaku satellite (Mitsuda et al. 2007).

3.1.2 Telescopes

3.1.2.1 Mirror Assembly

The XRT (figure 3.2) is the mirror assembly carried on Suzaku. It consists of five thin-foil-nested Wolter-I type telescope. One of the five XRT modules is dedicated for the XRS, which is called XRT-S, the others are for each CCD of the XIS, which are called XRT-I0, I1, I2, and I3. The XRT-Is have 175 thin-foil-nested mirrors. The schematic view of the Wolter-I type mirror is shown in figure 3.3. The Wolter-I type telescope is composed of a paraboloid-hyperboloid mirror. In order to reflect X-rays efficiently, the incident grazing angle of the reflector must be shallow (0.18°–0.60° for XRT-I). The focal length, the inner and outer diameters, and the weight are 4.75 m, 0.1m, 0.4 m, and 20 kg, respectively.

3.1.2.2 Effective Area

The total effective area of XRT is shown in figure 3.4 in comparison with two other X-ray satellites: XMM-Newton and Chandra. The effective area of Suzaku is similar to that XMM-Newton at about 6 keV. Figure 3.5 shows the off-axis angle dependence of the effective area, which is called vignetting. The effective area is smaller as the larger distance from the optical axis. The vignetting also depends on the incident photon energy. The effective area

Table 3.1: Detail of Suzaku (Suzaku team 2011).

	Parameter	Value
Spacecraft	Orbit apogee	$\sim$ 568 km
	Orbital period	$\sim$ 96 m
	Observing Efficiency	$\sim$ 45%
XRT	Focal length	4.75 m
	Field of view	$17'$ at 1.5 keV
		$13'$ at 8 keV
	Plate scale	0.724 $'$/mm
	Effective area	440 cm^2 at 1.5 keV
		250 cm^2 at 8 keV
	Angular resolution	$2'$ (HPD)
XIS	Field of view	$17.8' \times 17.8'$
	Band pass	0.2–12 keV
	Pixel grid	1024×1024
	Pixel size	24 μm × 24 μm
	Energy resolution	$\sim$130 eV (FWHM) at 6 keV
	Effective area	340 cm^2 (FI) , 390 cm^2 (BI) at 1.5 keV
		150 cm^2 (FI) , 100 cm^2 (BI) at 8 keV
	Timing resolution	8 s
HXD	Field of view	$4.5^\circ \times 4.5^\circ$ above 100 keV
		$34' \times 34'$ below 100 keV
	Band pass	10–70 keV (PIN)
		40–600 keV (GSO)
	Energy resolution	$\sim$ 4 keV (FWHM, PIN)
		$7.6/\sqrt{E_{\rm MeV}}$ % (FWHM, GSO)
	Effective area	160 cm^2 at 20 keV
		260 cm^2 at 100 keV
	Timing resolution	61 μs

ratio between the field edge and the center is 0.5 and 0.3 in the 3–6 keV and 8–10 keV, respectively.

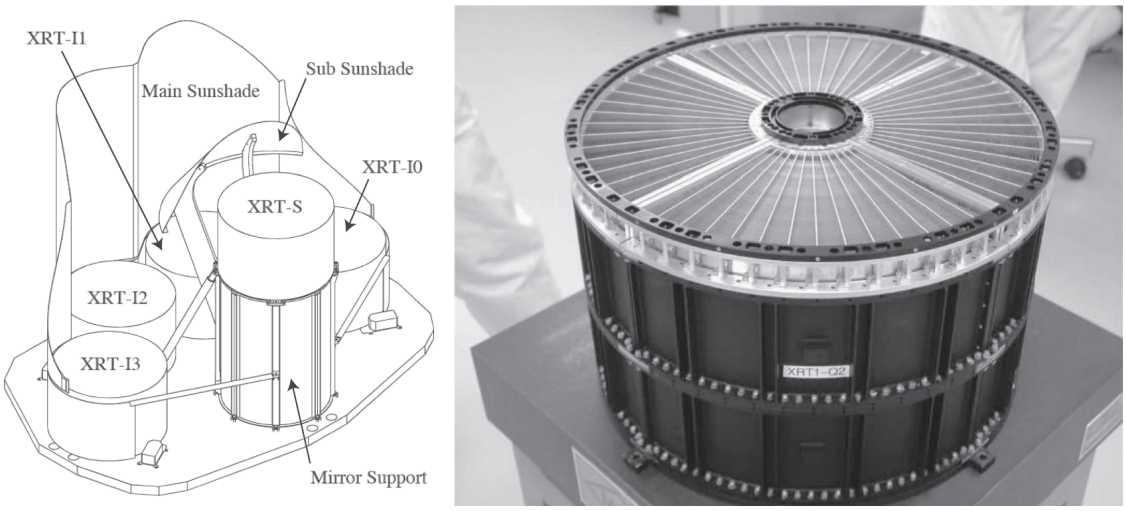

Figure 3.2: Schematic view of the XRT mounted on top plate (left) and a picture of an XRT-I module (right) (Serlemitsos et al. 2007).

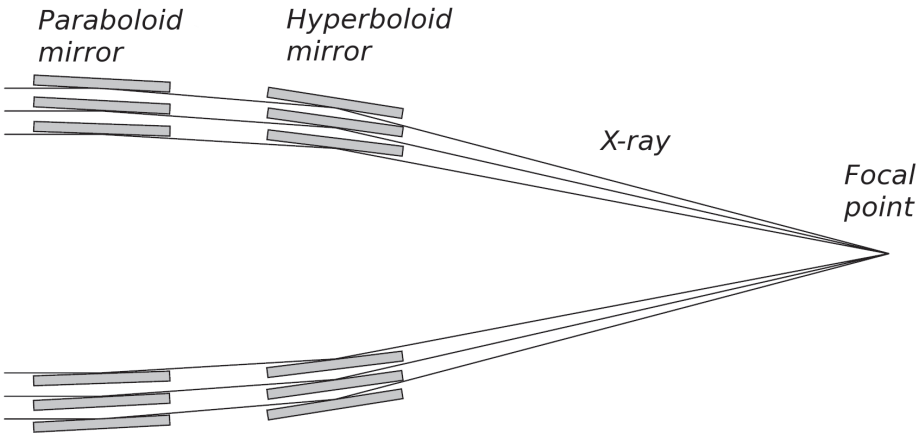

Figure 3.3: Schematic cross-section of Wolter-I type X-ray mirror. Incident X-rays are reflected twice at a very shallow angle and concentrated at the focal point (Hyodo 2009).

3.1.2.3 Angular Resolution

Point spread function (PSF) is a spatial distribution function over the detector surface of incident X-ray photons at a given energy for a point-like source at infinity. For the XRT, the PSF is approximately shaped Gaussian, and independent of the photon energy position. The

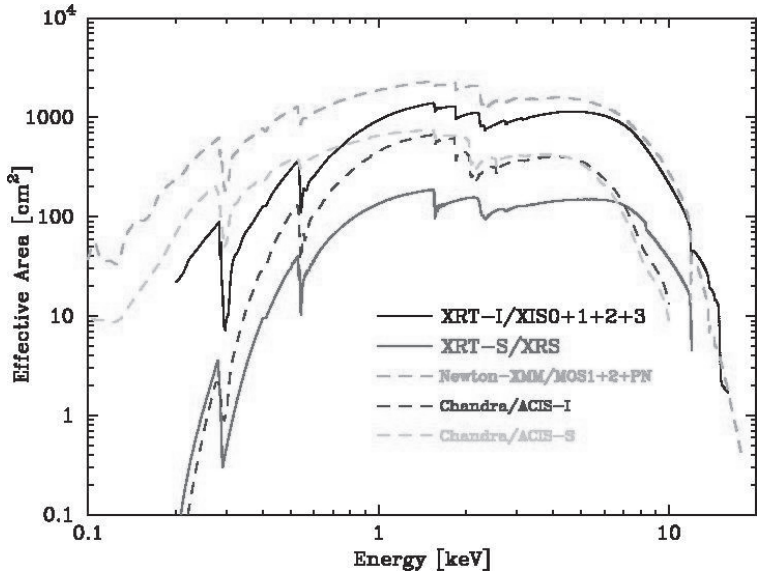

Figure 3.4: Total effective area of the four XRT-I modules combined with the transmissions of the thermal shield, the optical blocking filter, and the quantum efficiency of the XIS (Serlemitsos et al. 2007). Other X-ray missions are compared.

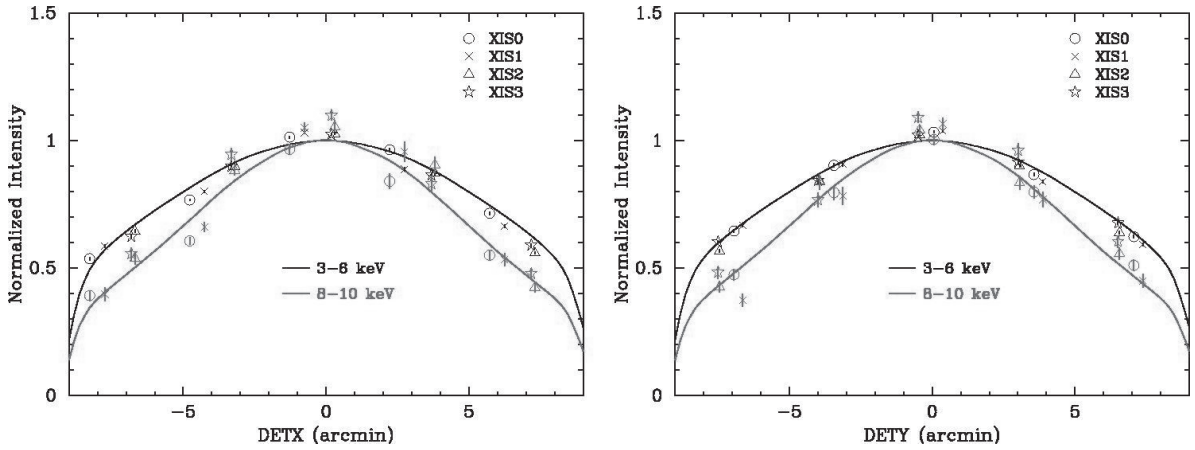

Figure 3.5: Off-axis angle dependence of the effective area normalized at the optical axis in two energy bands 3–6 keV (black) and 8–10 keV (red) band (Serlemitsos et al. 2007). The data are obtained by a observation of the Crab Nebula taken in 2005 August 22–27. The model curves are calculated with a ray-tracing simulator.

sharpness of images is evaluated either by the full width at a half maximum (FWHM) or the encircled energy radius of PSF. A circle of 50% encircled energy radius, which is called a half

power radius and equals to the half of FWHM if the PSF is exactly Gaussian, accumulates 50% of incident photons. Figure 3.6 shows the images, the radial profile, and the encircled energy function (EEF) of the PSF for each CCD. The half power diameter (HPD) is 1.8′, 2.3′, 2.0′, and 2.0′ for XRT 0, 1, 2, and 3, respectively.

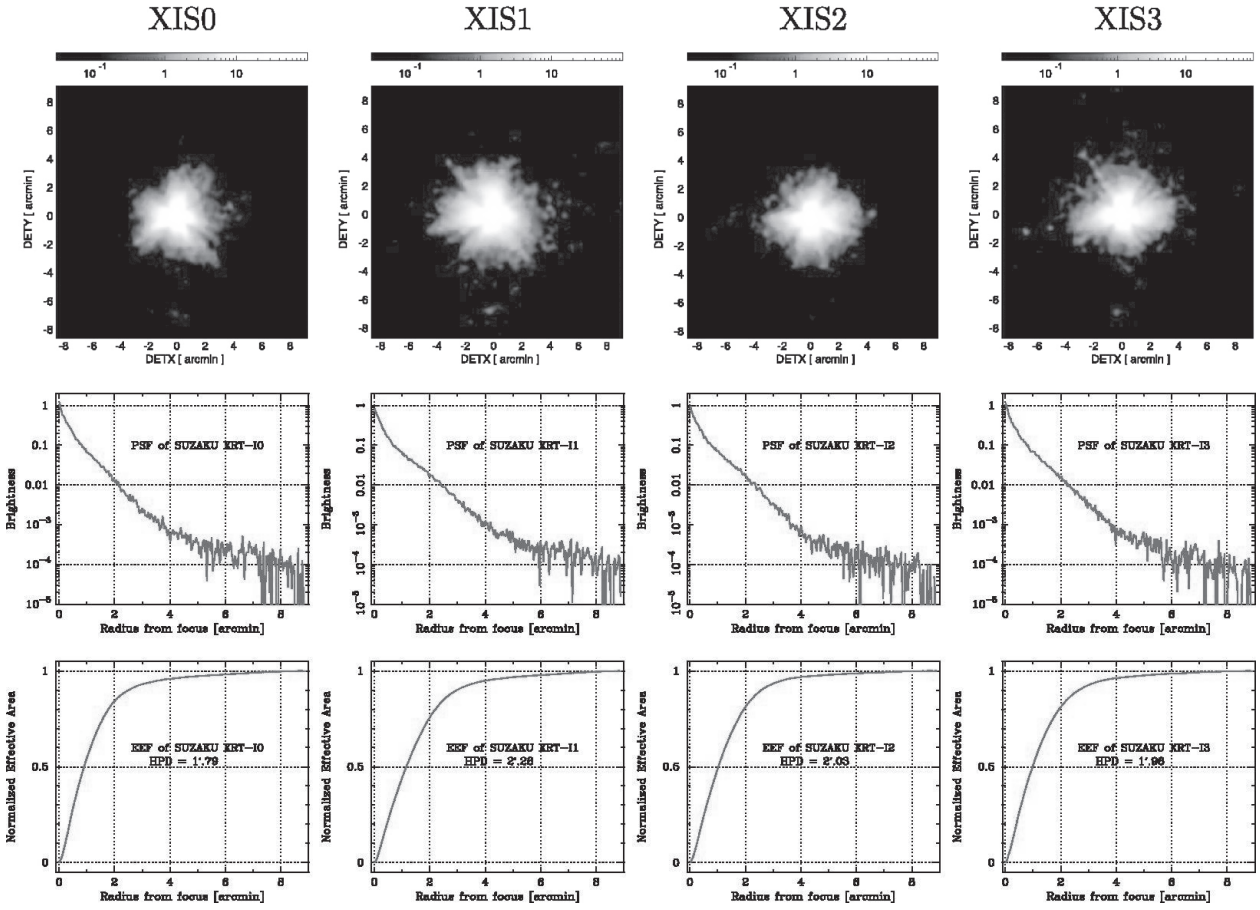

Figure 3.6: Image (top), radial profile (middle), and encircled energy function (bottom) of the XRT for the four XIS sensors. A bright point-like source (SS Cyg) was placed at the optical axis (Serlemitsos et al. 2007).

3.1.3 Instrument I : X-ray Imaging Spectrometer

3.1.3.1 Overview

The XIS has four X-ray CCDs, which are called XIS 0, 1, 2, and 3. Each sensor is placed at the focal plane of the XRT. Figure 3.7 shows a picture and a cross section of a CCD sensor. The XIS 0, 2, 3 use a front illumination (FI) CCD, and the XIS 1 uses a back illumination (BI) CCD. Because of putative micrometeorite hits, the entire XIS 2 and a part of the XIS 0 became dysfunctional respectively since 2006 November and 2009 December.

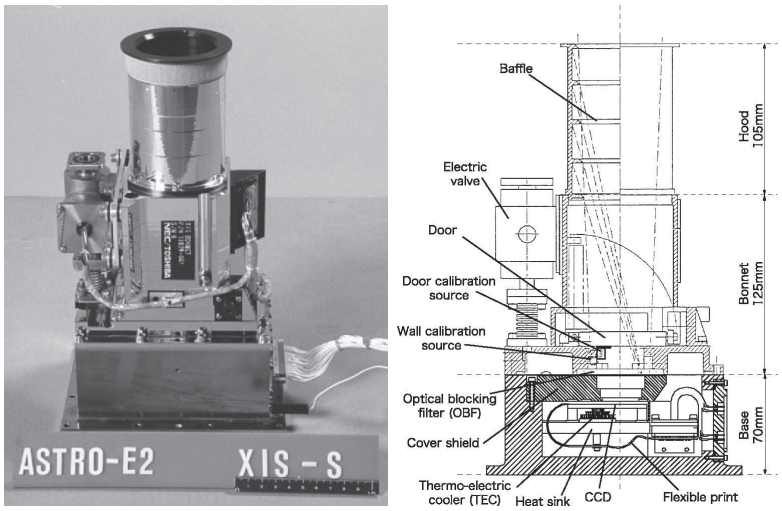

Figure 3.7: Picture of the XIS (left) and cross section of the XIS sensor (right) (Koyama et al. 2007).

3.1.3.2 Structure of CCDs

An X-ray CCD converts an incident X-ray photon to a cloud of electrons by photoelectric absorption and following ionization. The amount of electrons is proportional to the energy of the absorbed X-ray photon. The cloud made in the depletion layer at each pixel is transferred to the gate of the output transistor by a three-phase electric potential clocking.

The gate structure is made of thin Si and SiO_2 layers. The FI CCDs detect X-rays that penetrate the gate structure with a thickness of about 0.7 μm, whereas the surface dead layer of the BI CCD has a thickness of about 10 nm shown in figure 3.8. Due to the absence of the gate structure, the BI CCD achieves a high quantum efficiency (QE) even

below about 1 keV. On the other hand, the FI CCDs have a thicker depletion layer than the BI CCD (about 76 μm for FIs and about 42 μm for BI) and have a higher QE for high energy photons.

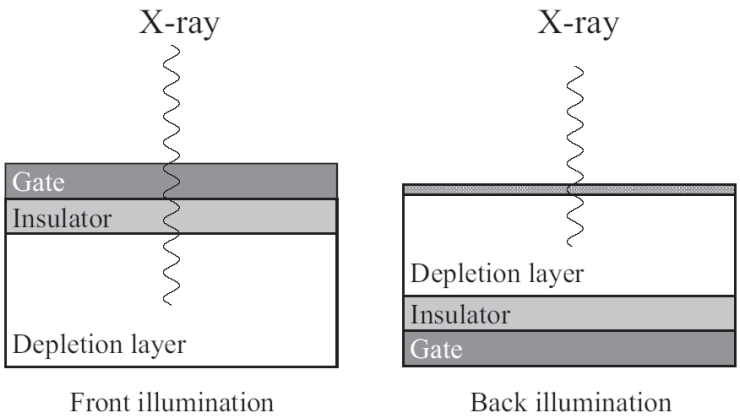

Figure 3.8: Structure of the FI (left) and BI (right) CCD. The CCD is composed of a gate, an insulator and a depletion layer. The difference of these CCDs is the side for the incident photon.

3.1.3.3 Configuration

The XIS CCD consists of four segments (A, B. C, and D) with a dedicated read-out node shown in figure 3.9. The imaging area has 1024 $\times$ 1024 pixels, which covers an $18' \times 18'$ region on the sky with the XRT. The pixel size is 24 μm $\times$ 24 μm, giving a total size of 25 mm $\times$ 25 mm. The calibration sources, which are two ^{55}Fe radio isotope, are placed in two corners of each CCD.

3.1.3.4 Effective Energy Range

The QE for the FI and the BI sensors are shown in figure 3.10. The FI CCDs detect photons that penetrate the gate structure, providing a low background observations. In construct, the BI CCD detect photons that comes from a back side without the gate structures, providing a high QE for low energy photons.

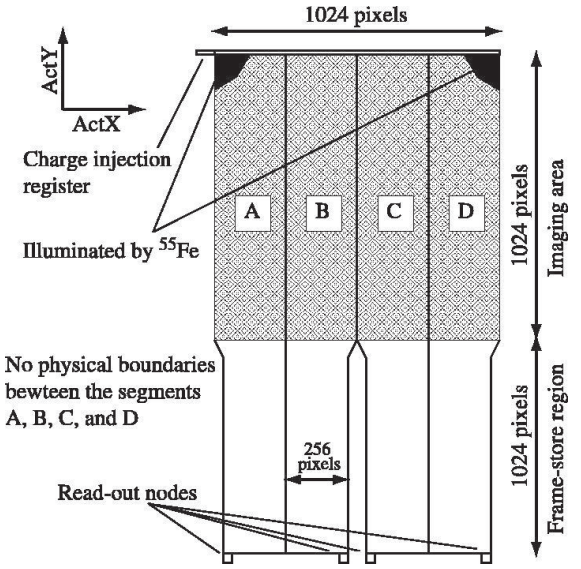

Figure 3.9: Schematic view of the XIS CCD (top view) (Koyama et al. 2007). A CCD consists of four segments, which have imaging area, frame stored area, and a dedicated read-out node.

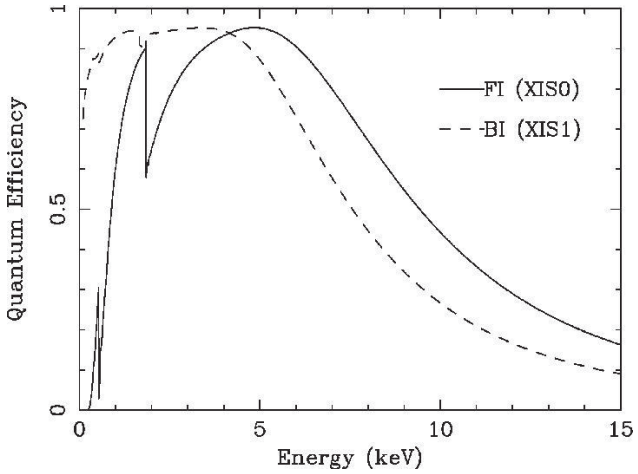

Figure 3.10: QE as a function of incident energy calculated using the best estimate values of the thickness of the dead and depletion layers (Koyama et al. 2007). The solid curve is for an FI CCD (XIS 0) and the dashed curve is for an BI CCD (XIS 1).

3.1.3.5 Energy Resolution

The energy resolution is shown in figure 3.11. Because of radiation damages in orbit, the energy resolution is degraded day by day. In order to mitigate the degradation, the XIS employs the spaced-raw charge injection (SCI) technique. Electrons are injected artificially form one side of the chip and are read out along with charges produced by X-ray events. The artificial charges are injected periodically in space. They fill up charge traps and thereby alleviate the increase in charge transfer inefficiency for the X-ray events. Since the installation of the SCI technique, the energy resolution was improved as shown in figure 3.11.

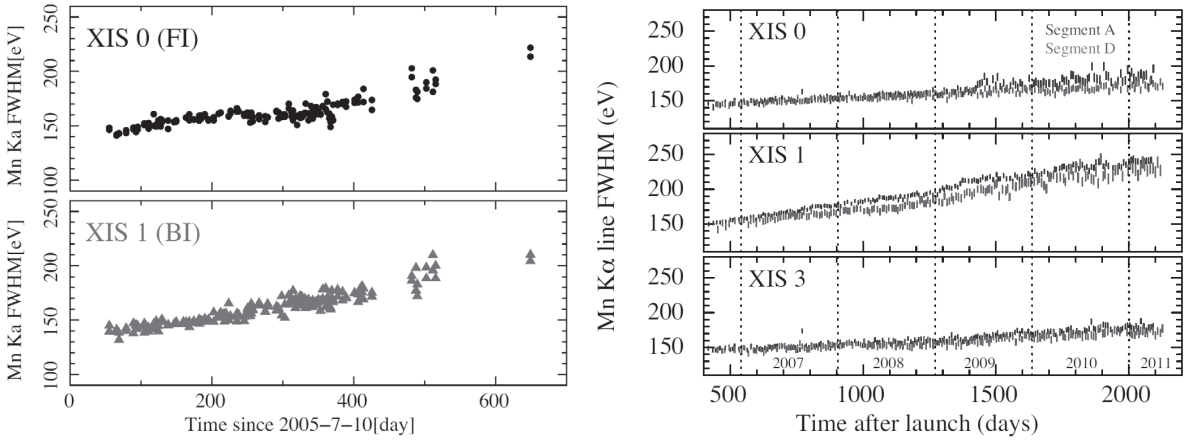

Figure 3.11: Time history of the energy resolution of Mn Kα derived from the ^{55}Fe calibration sources (Suzaku team 2011). The left and right panels respectively show the data before and after the SCI technique is used.

3.1.3.6 Background Events

The background of the X-ray detector in the orbit consists of two components: X-ray background and non-X-ray (or cosmic-ray) background (NXB). The X-ray background mainly consists of cosmic X-ray background (CXB), a Galactic component, and a solar component.

The CXB originates from the ensemble of numerous faint extragalactic sources. Based on observations from the ASCA satellite, the spectra of of the CXB is described with a power-law model with a photon index about $1.412 \pm 0.007 \pm 0.025$. The flux in the 2-10 keV range is $(6.38 \pm 0.04 \pm 0.64) \times 10^{-8}$ erg cm^{-2} s^{-1} sr^{-1}. Here, the first and second errors are 1σ statistical and systematic error. The characteristic of the CXB is that the flux

fluctuate about 10% in different directions (Kushino et al. 2002). The Galactic component is optically-thin thermal emission, which originates from the local hot bubble and Galactic halo. The intensities vary significantly from field to field by $52\ ^{+4}_{-5}$ % (1 sigma) recording the maximum toward the Galactic Center (Kushino et al. 2002). The temperature is 0.204 $\pm$ 0.009 keV (Lumb et al. 2002). The solar component is the emission form Earth's albedo and solar wind charge exchange.

The NXB is caused in the radiation environment of the satellite. Because the altitude of the orbit of Suzaku is lower than that of XMM-Newton (§ 3.1.4) and other X-ray satellites, the NXB level of Suzaku are lower. The NXB spectra of Suzaku are shown in figure 3.12. The spectra are characterized by the fluorescence lines of Al, Si, Au, Mn, and Ni. For example, the Ni-Kα (7.470 keV) and the Ni-Kβ (8.265 keV) lines originate from the fluorescence by the materials used in the housing and the heatsink of the XIS.

Because the NXB is caused by charged particle, it is strongly correlated with geomagnetic cut-of-rigidity (COR). Thus, the NXB is predictable based on a model considering the histogram of the COR in each observation. The reproducibility of the NXB model with cut-of-rigidity is 5 % for each XIS in the 1–7 keV band (Tawa et al. 2008).

3.1.3.7 On-ground event selection

The background due to charged particles can be efficiently eliminated using the spatial distribution pattern of charge clouds on CCD pixels (grade), the position (status), and time of events. The definition of grades is shown in figure 3.13. Most X-ray events take the grade = 0, 2, 3, 4, and 6. The grades 1 and 5, which consist of a single pixel event with one or more detached corner events, should be ignored because most are particle events. The status parameter stores the information of pixel quality of events. Known hot pixels, bad columns transfer efficiency, flickering pixels can be removed by selecting the events with the status $<$ 524287. The parameters used in the good time interval (GTI) filtering are shown in table 3.2

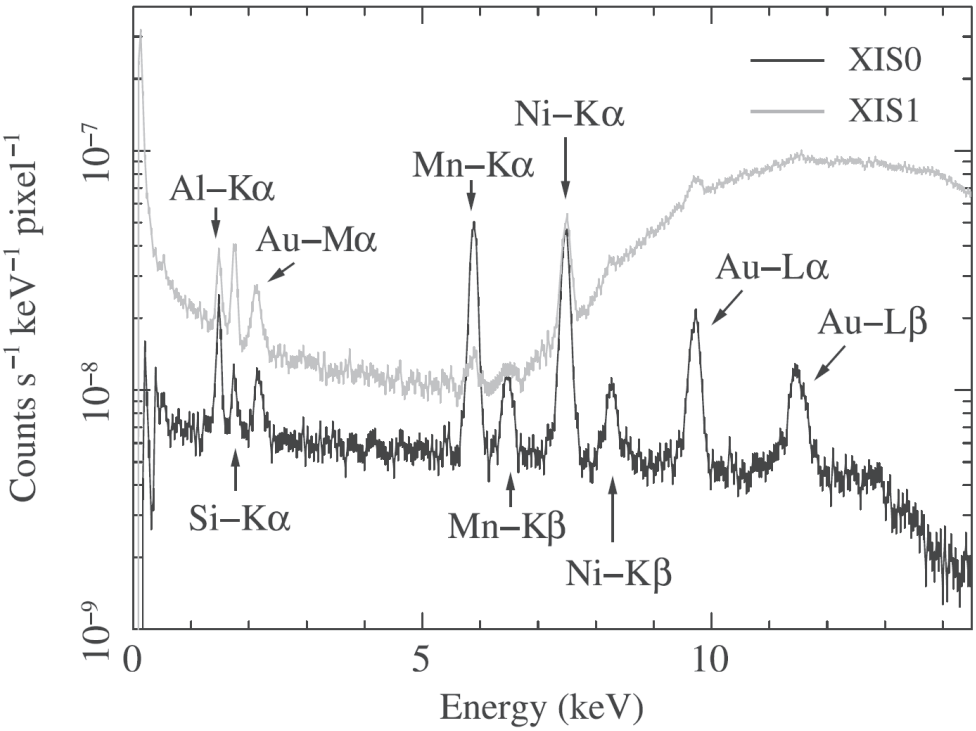

Figure 3.12: Obtained spectra of the NXB for the FI (XIS 0; black) and the BI (XIS 1; gray) CCD. (Tawa et al. 2008).

Table 3.2: Parameters used in GTI selection.

Parameter	Definition	Value
SAA	Whether the satellite was in the South Atlantic Anomaly (SAA) or not	not (0)
T_SAA	Time after the last SAA duration (s)	255
ELV	Elevation angle from the Earth limb (degree)	5
DYE_ELV	Elevation angle from the day Earth limb (degree)	20
COR	Cut off rigidity of the cosmic ray (GeV/C)	6

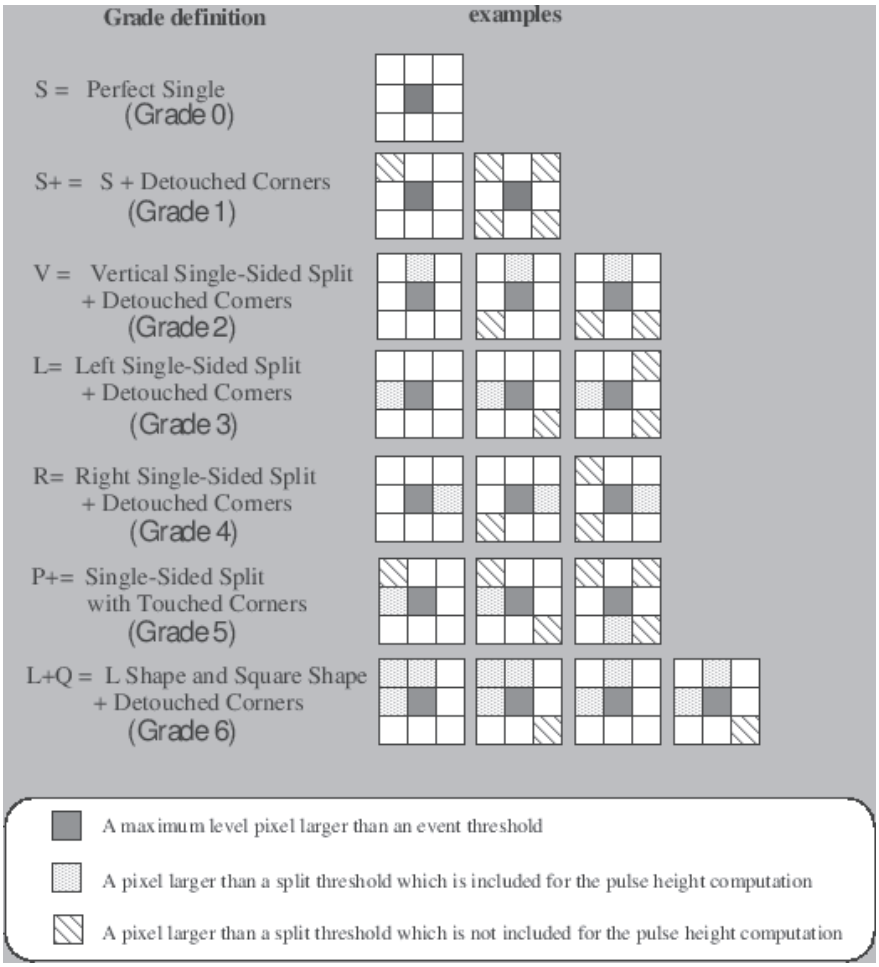

Figure 3.13: Definition of event grades (ASCA Data Reduction Guide 2011).

3.1.4 Instrument II : Hard X-ray Detector

3.1.4.1 Overview

The HXD is a non-imaging collimator instrument, which is a combination of silicon PIN diodes (PIN) and GSO scintillators (GSO) (figure 3.14). In order to decrease the background level, the phoswich counter techniques is used. Figure 3.15 shows the structure of the HXD. The HXD consists of 16 phoswich well counters and 20 BGO veto counters.

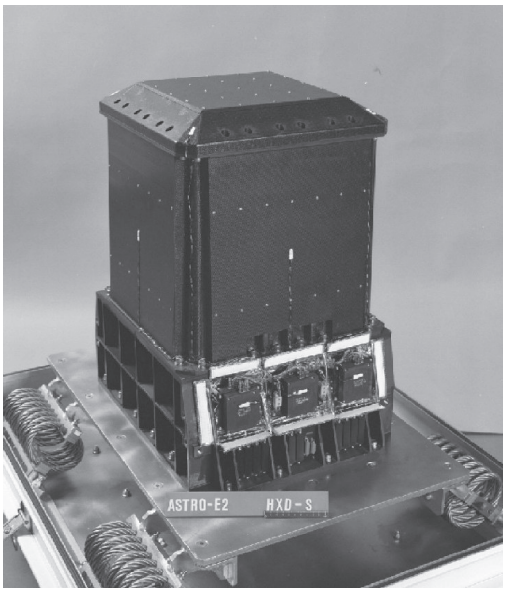

Figure 3.14: Picture of the HXD (Takahashi et al. 2007).

3.1.4.2 Effective Area

The effective areas at the optical axis of the PIN and GSO are shown in figure 3.16. The effective energy bad of the two detectors is 10–70 keV and 40–600 keV, respectively.

3.1.4.3 Background Events

The NXB lightcurve and spectra are shown in figure 3.17. The NXB increases during South Atlantic Anomaly (SAA) passages. A precise estimate of the NXB is particularly important for objects fainter than 10 mCrab ($\sim 2 \times 10^{-6}$ erg s^{-1} cm^{-2} in the 12–40 keV band).

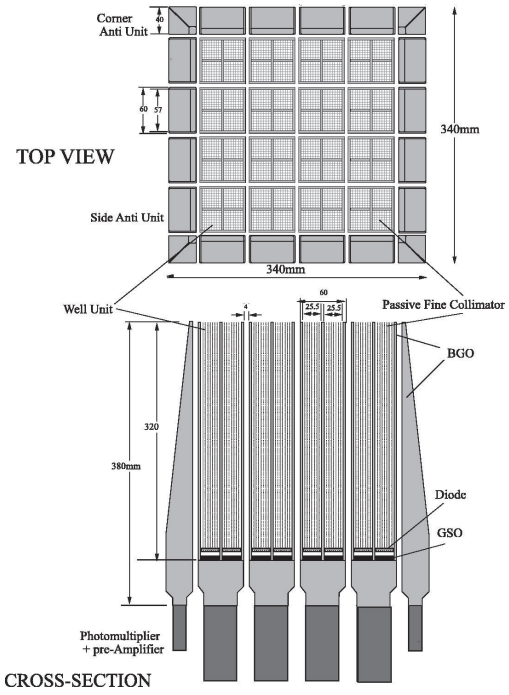

Figure 3.15: Top view and cross section of the HXD (Takahashi et al. 2007).

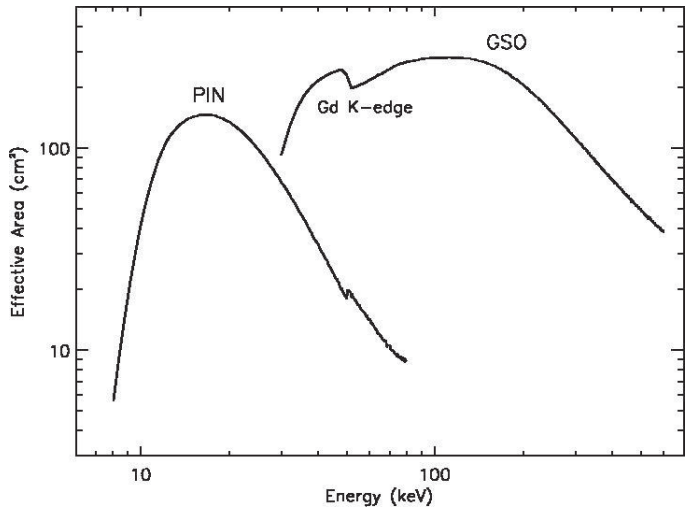

Figure 3.16: Total effective area of the HXD (Takahashi et al. 2007). Photon absorption by materials in front of the device is taken into account.

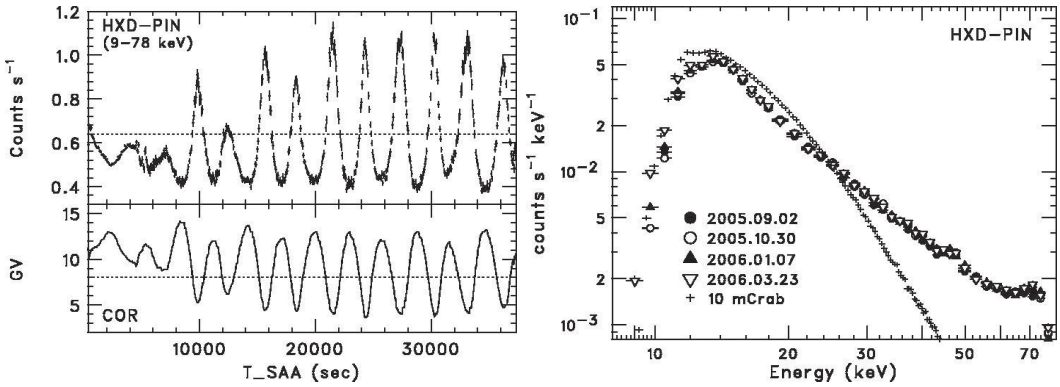

Figure 3.17: (Left) : Light curve of the mean PIN-NXB folded by T_SAA in the energy range of 9–78 keV (top) and cut-off rigidity (bottom) (Kokubun et al. 2007). (Right) : Comparison of four averaged NXB spectra measured by HXD-PIN on 4 occasions separated by two months (Kokubun et al. 2007). Each observation has an exposure longer than two days. The Crab spectrum, scaled down by two orders of magnitude, is also shown.

3.2 XMM-Newton Satellite

3.2.1 Overview

The XMM-Newton Observatory is a cornerstone mission of the European Space Agency's Horizon 2000 program (figure 3.18). XMM-Newton was launched in 1999 December 10 with an Ariane 504 rocket from the Guiana Space Centre. The orbit is elliptical with an apogee and perigee of 115,000 and 6,000 km, respectively, and with an orbital period of 48 hours. The detailed specifications of the XMM-Newton mission are shown in table 3.3.

The satellite has three instruments: the European Photon Imaging Camera (EPIC), which has three X-ray CCD detectors at the focal plane of three X-ray telescopes, the Reflection Grating Spectrometer (RGS), which is an X-ray grating instrument, and the Optical Monitor (OM), which is an optical/UV telescope. The EPIC consists of two Metal Oxide Semi-conductor CCD arrays (MOS1 and MOS2) and an pn-type array (PN). In the following section, the EPIC and the mirror system, which are used in this thesis, are described.

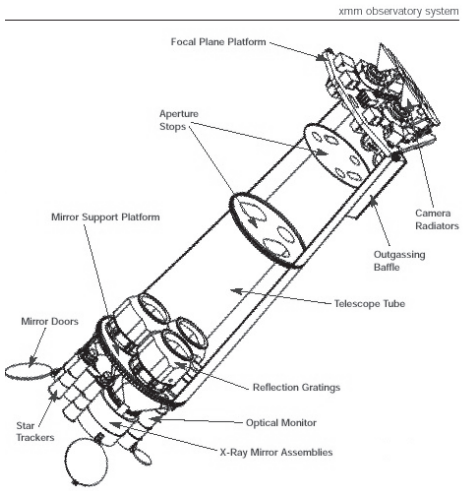

Figure 3.18: Schematic cross-section of the XMM-Newton with the internal structure (http://xmm.esac.esa.int/).

Table 3.3: Specifications of XMM-Newton mission.

	Parameter	Value
Spacecraft	Orbit apogee	$\sim$ 115,000 km
	Orbit perigee	$\sim$ 6,000 km
	Orbital period	$\sim$ 48 h
Telescope	Focal length	7.5 m
	Field of view	$30'$
	Angular resolution	$15''$ (HPD)
EPIC-PN	Field of view	$30'$
	Band pass	0.15–12 keV
	Pixel size	150 μm $\times$ 150 μm
	Energy resolution	$\sim$ 80 eV (FWHM) at 6.4 keV
	Effective area	$\sim$1300 cm^2 at 1.5 keV
		$\sim$500 cm^2 at 8 keV
	Timing resolution	0.04 ms
	Sensitivity	$\sim 10^{-14}$ erg s^{-1} cm^{-2}, in the 0.15-12 keV.
EPIC-MOS	Field of view	$30'$
	Band pass	0.15–12 keV
	Pixel size	40 μm $\times$ 40 μm
	Energy resolution	$\sim$ 70 eV (FWHM) at 6.4 keV
	Effective area	$\sim$ 500 eV (FWHM, single MOS) at 1.5 keV
		$\sim$ 100 eV (FWHM, single MOS) at 8 keV
	Timing resolution	1.75 ms
	Sensitivity	$\sim 10^{-14}$ erg s^{-1} cm^{-2}, in the 0.15-12 keV.

3.2.2 Telescopes

3.2.2.1 Mirror Assembly

XMM-Newton has three X-ray telescopes co-aligned each other. Each telescope has 58 Wolter I grazing-incidence mirrors, which are nested in a coaxial and confocal configuration (figure 3.19). The focal length is 7.5 m and the diameter of the largest mirrors is 70 cm.

The optical pass of the PN telescope is shown in figure 3.20. The MOS telescopes are

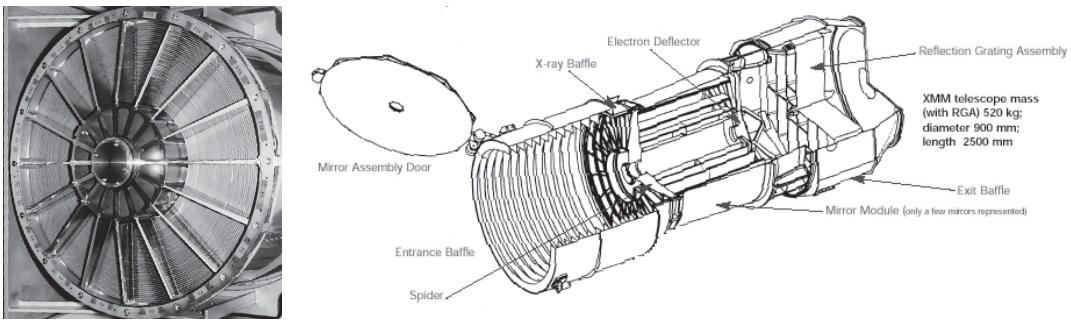

Figure 3.19: Picture of telescope (left) and configuration (right) (XMM-Newton Users Handbook 2011).

equipped with grating elements in the their optical passes. For the telescopes with grating assemblies, 44% of incoming photons are detected by the MOS instruments, and 40% are detected by the RGS detector.

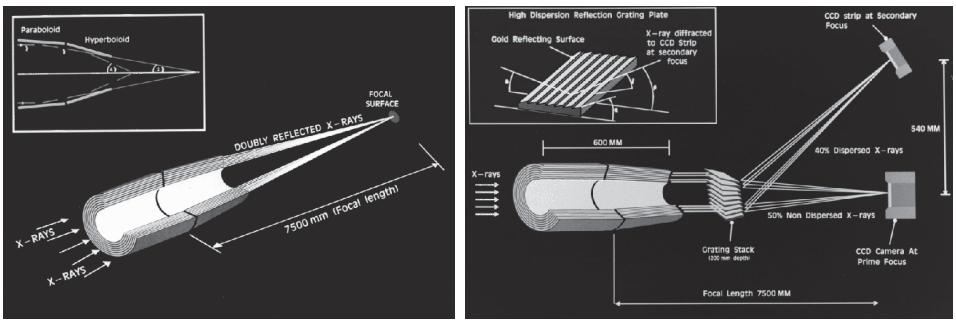

Figure 3.20: The light path in the telescopes for PN (left) and MOS (right) (XMM-Newton Users Handbook 2011).

3.2.2.2 Effective Area

The on-axis EPIC effective area convolved with the quantum efficiency of the focal plane instruments is shown in figure 3.21 left. The mirrors are most efficient in the energy range 0.1–10 keV, with a maximum at about 1.5 keV. Since the MOS shares photons with RGS, the effective areas of the MOS are smaller than that of the PN. While the off-axis EPIC effective area is effective of vignetting shown in figure 3.21 right. The effective area ratio between the field edge and the center at the photon energy 1.5 keV and 8 keV are 0.3 and 0.2, respectively.

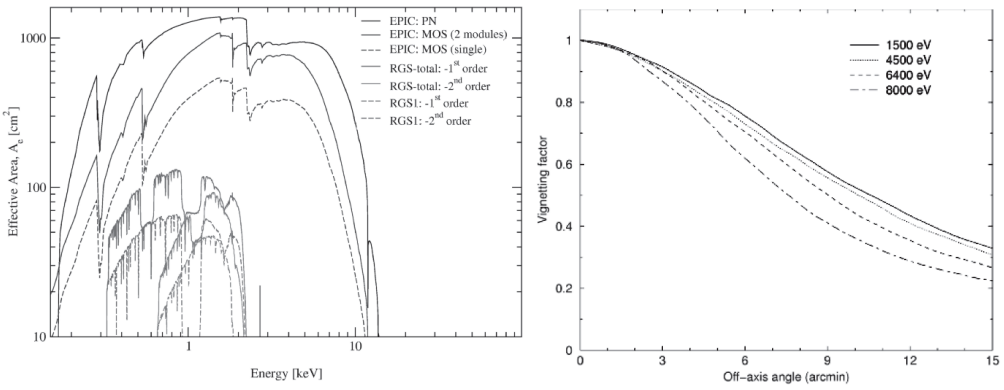

Figure 3.21: (left) On-axis effective areas of all XMM-Newton X-ray telescopes, EPIC and RGS (XMM-Newton Users Handbook 2011). (right) Off-axis effective area with respect to the value at the on-axis for the PN.

3.2.2.3 Angular Resolution

The PSF for MOS can be approximated using a King profile (figure 3.22). The HPD of the telescope is about 15″, which is one-eighth of that of Suzaku telescopes.

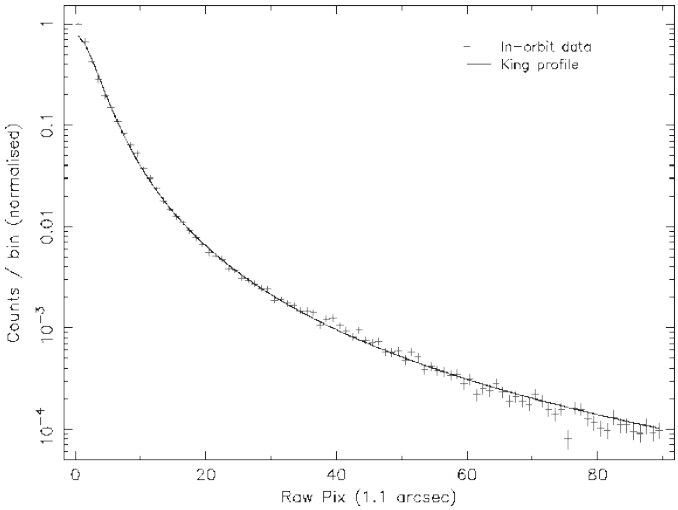

Figure 3.22: PSF of MOS1 (XMM-Newton Users Handbook 2011).

3.2.3 Instrument : European Photon Imaging Camera

3.2.3.1 Overview

The EPIC consists of two MOS (MOS1, MOS2; Turner et al. 2001) and one PN (Strüder et al. 2001) instruments. The sensors of each instrument are shown in figure 3.23. The two types of the EPIC instruments have different characteristics. The two MOS instruments have seven FI CCDs, which are sensitive at an energy range of 0.15–12 keV. The PN instruments has twelve BI CCDs, which are sensitive at an energy range of 0.15–15 keV.

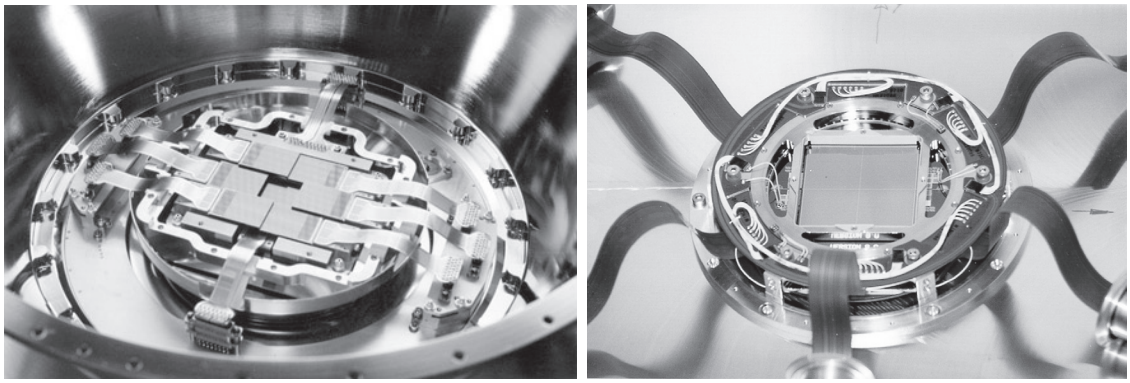

Figure 3.23: Picture of the EPIC. MOS (left), PN (right) (XMM-Newton Users Handbook 2011).

3.2.3.2 Configuration

The layout of the EPIC cameras is shown in figure 3.24. In MOS, the central CCD is at the optical axis of the telescope, while the outer six are elevated towards the mirror by 4.5 mm to follow approximately the focal plane curvature, thereby to improve the imaging quality for off-axis sources. The imaging area for each CCD chip is $\sim 2.5 \times 2.5$ cm^2, so that a mosaic of seven covers the focal plane of 62 mm in diameter, which is equivalent to $28.4'$. One pixel covers $1.1'' \times 1.1''$. The readout register is split into two sections, ending in a readout node. The full CCD image can be read out using either node, or read out using both nodes simultaneously, to halve the readout time.

In PN, the spatially uniform detector quality over the entire FoV is realized by the monolithic fabrication of twelve 3×1 cm pn-type CCDs on a single wafer. The four individual quadrants each having three pn-CCD subunits with a format 200×64 pixels are

operated in parallel.

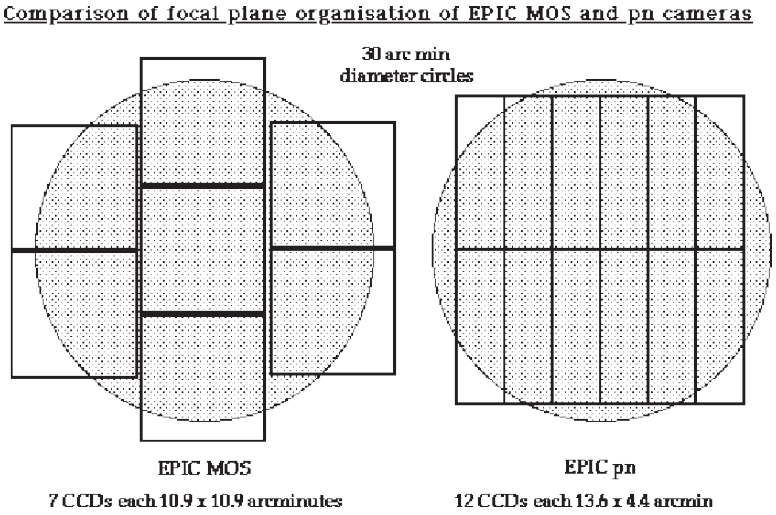

Figure 3.24: Layout of EPIC instruments (left:MOS, right:PN) (XMM-Newton Users Handbook 2011). The shaded circle shows a 30′ diameter circle.

3.2.3.3 Effective Energy Range

The QEs for MOS and PN are shown in figure 3.25. The QE of the PN is constant in the energy range 0.3–10 keV, while the QEs of the MOSs are depend of the energy with a factor of about 0.5 in the same energy range. The absorption feature at 528 eV and 18.38 eV are respectively by O and Si in the insulator.

3.2.3.4 Energy Resolution

The energy resolution for MOS and PN is shown in figure 3.26. In the MOS, the resolution suffered a rapid degradation by about 10 % during the early phase of the mission. The operational temperature of the MOS was decreased between November and December 2002 to improve the resolution. Since then, the energy resolution of the MOS has been basically constant. In the PN, a constant degradation of the energy resolution with a rate of about 2.5 eV yr^{-1} has been measured.

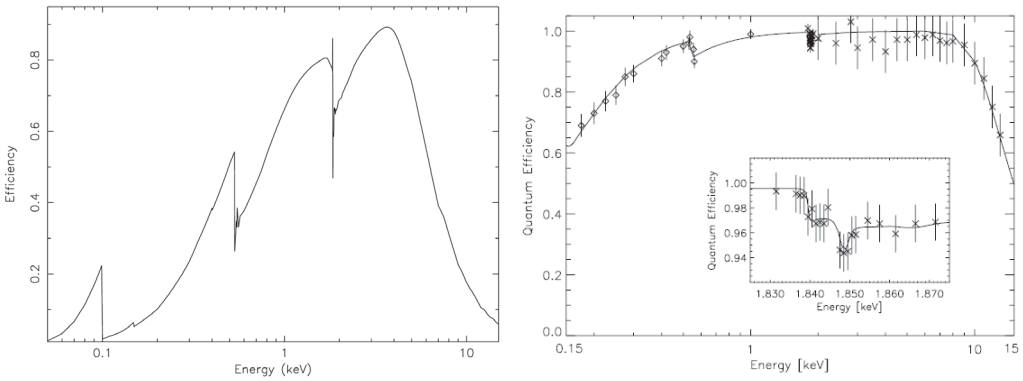

Figure 3.25: Quantum efficiency for MOS (left) and PN (right) (XMM-Newton Users Handbook 2011).

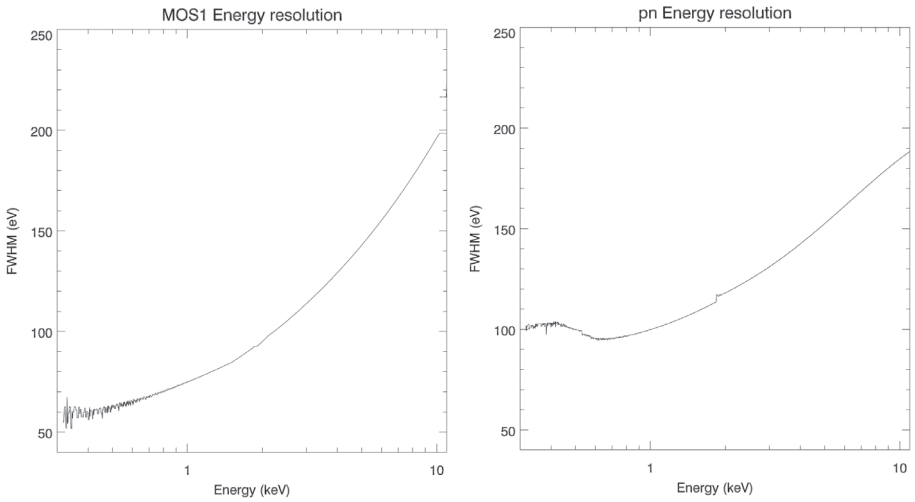

Figure 3.26: Energy resolutions for MOS1 (left, blue curve) and PN (right, black curve), which are simulated with science analysis software (SAS) version 11.0 (XMM-Newton Users Handbook 2011).

3.2.3.5 Background Events

The NXB of the EPIC can be divided into two components: the external flaring component characterized by strong and rapid variability, and the internal stable component. The flaring component is currently attributed to soft protons (< a few 100 keV), which are presumably collected at the detectors by the X-ray mirrors. The stable component is due to the interaction of high-energy particle (> a few 100 MeV) with the structure surrounding the detector and possibly the detector themselves.

Figure 3.27 shows a lightcurve obtained with MOS 1. During the first part of the lightcurve, the background is constant. The second half, however, is heavily affected by a proton flare. Thus, in the EPIC data analysis, it is important to examine the NXB level and remove the intervals affected by flaring events.

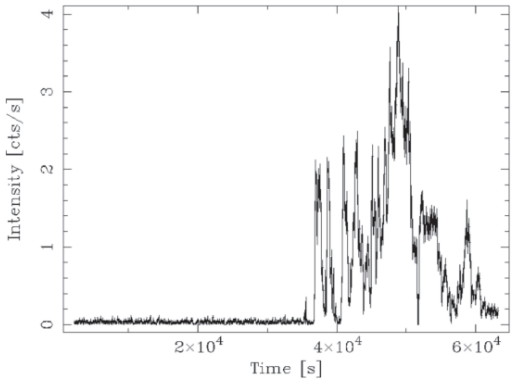

Figure 3.27: Lightcurve from an MOS 1 observation badly affected by soft proton flares (XMM-Newton Users Handbook 2011).

The quiescent NXB spectra for MOS and PN are shown in figure 3.28. The spectra are quite flat and exhibit a number of spectral features due to fluorescence from the detectors and the structure surrounding them. In the MOS spectrum, it has Al-Kα and Si-Kα lines. In PN, Al-Kα and an complex due to Cu-Kα, Ni-Kα, and Z-Kα lines around 8 keV are visible. An important point for the PN NXB is that the line intensities have spatial gradients (figure 3.29). The NXB count rate of the PN is relatively higher than that of the MOS.

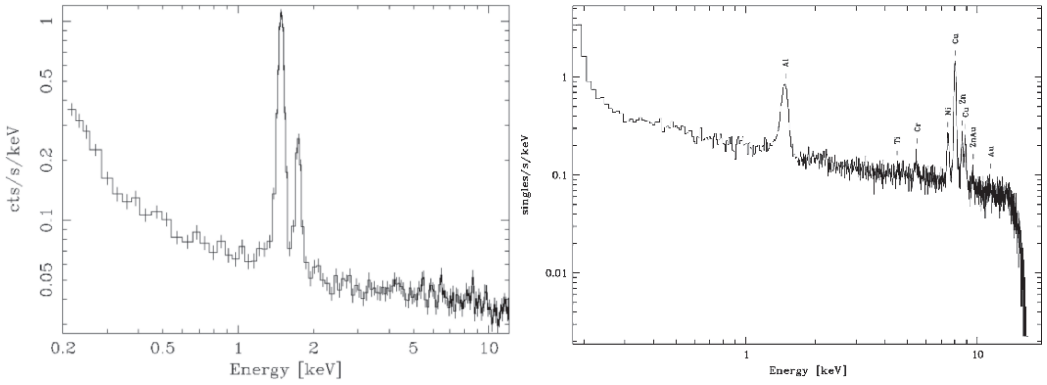

Figure 3.28: NXB spectrum for the MOS (left) and PN (right) (XMM-Newton Users Handbook 2011).

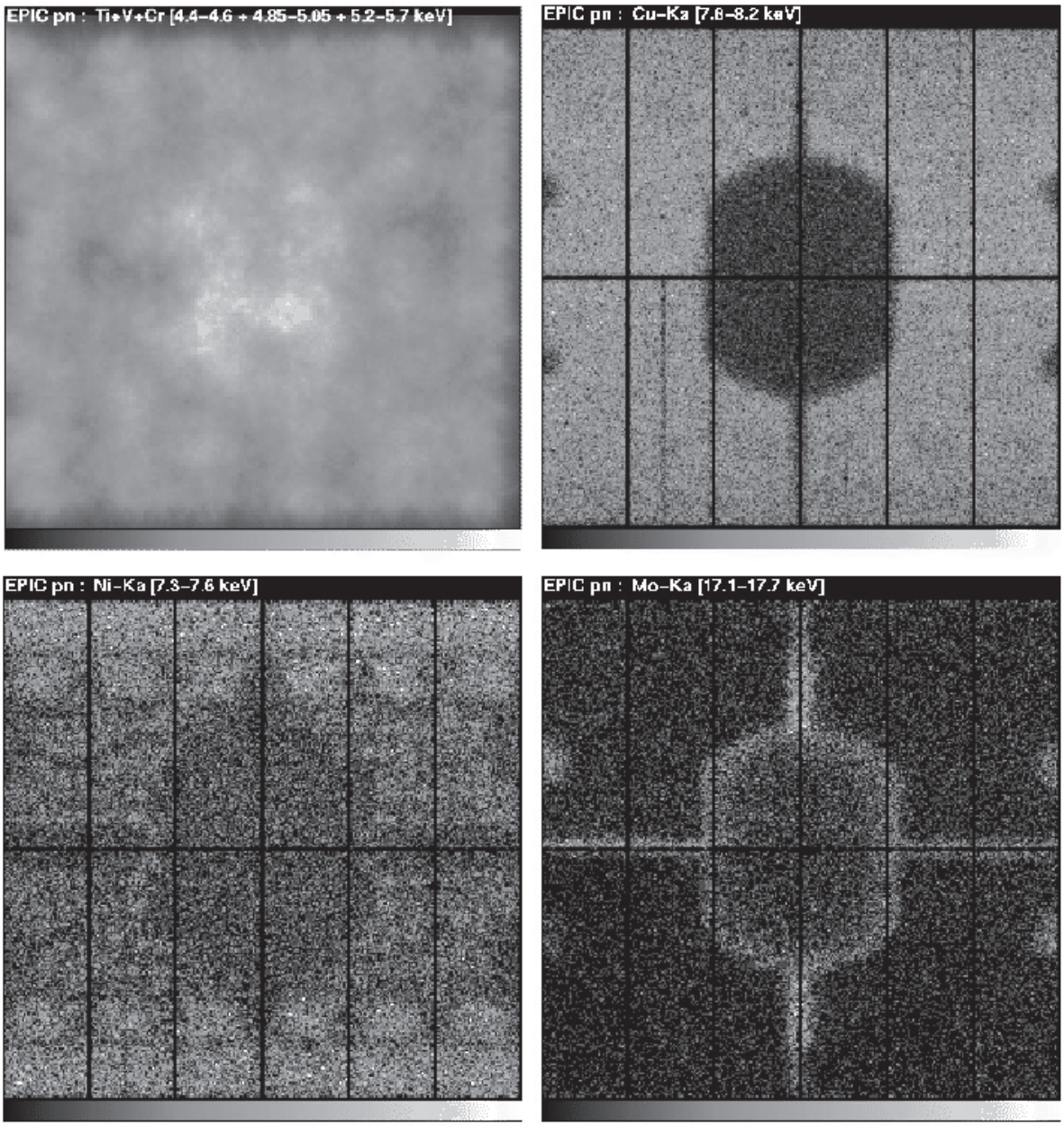

Figure 3.29: Background images of PN for four fluorescence line bands: smoothed image in the Ti+V+Cr Kα lines (top left), the Cu line at 7.8–8.2 keV (top right), the Ni line at 7.3–7.6 keV (bottom left), and the Mo line at 17.1–17.7 keV (bottom right)(XMM-Newton Users Handbook 2011).

3.3 Nobeyama Millimeter Array

Nobeyama Millimeter Array (NMA) is a radio interferometer at the Nobeyama observatory in Nagano, Japan (figure 3.30). The NMA consists of six 10-m antennae equipped with cooled DSB SIS receivers. The frequency coverage is 80–230 GHz. Using the longest baseline configuration, it is achieves a beam size of 0.0003°. The performance of the NMA is shown in table 3.4. Two different receivers are installed: S100 and S150. The effective band for S100 and S150 is 85–116 GHz, and 126–152 GHz, respectively. The spectrocorrelator has two sensor; Ultra-Wide-Band Correlator (UWBC) (Okumura et al. 2000) and New-FX. The UWBC is an XF-type digital spectrocorrelator, which is suited for observing continuum emission and line emission with a wide velocity widths. The New FX is an FX-type digital spectrocorrelator, which is suited for observations requiring a high velocity resolution spectroscopy.

During our observation, the NMA array was set in the C configuration. In the C configuration, the antennae are laid out at the position number of 26, 24, 16, 10, 23 and 14, as shown in figure 3.31. The maximum and minimum baseline lengths are 163 m and 26 m, respectively. A more detailed description can be found in http://www.nro.nao.ac.jp/ nma/.

Figure 3.30: Picture of the NMA (http://www.nro.nao.ac.jp/ nma/).

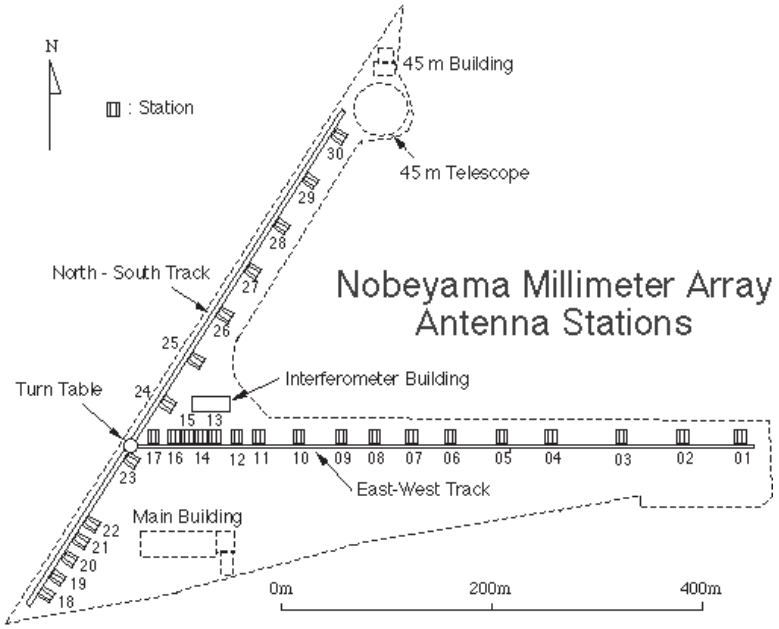

Figure 3.31: Positions of NMA antennae (http://www.nro.nao.ac.jp/ nma/).

Table 3.4: Performance of the NMA.

Parameter	Value
Diameter of antenna	10 m
The number of antennae	6
Frequency	80–230 GHz
Beam size (minimum)	0.0003°
Field of view	77″(88GHz), 62″(110GHz), 46″(147GHz)

3.4 Kanata Telescope

The Kanata telescope is an optical and near-infrared telescope at the Higashi-Hirosima Observatory in Hiroshima, Japan. The diameter of the primary mirror is 1.5 m, which is one of the largest mirrors in Japan. Figure 3.32 and 3.33 show the picture of the telescope. The feature of the telescope is shown in table 3.5. The telescope has four instruments; TRISPEC, HOWPol, high speed CCD camera, and HONIR. The TRISPEC is a simultaneous optical and near-Infrared imager, spectrograph, and polarimeter. The HOWPol is an optical polarimeter. The HONIR is optical and Near-Infrared Camera.

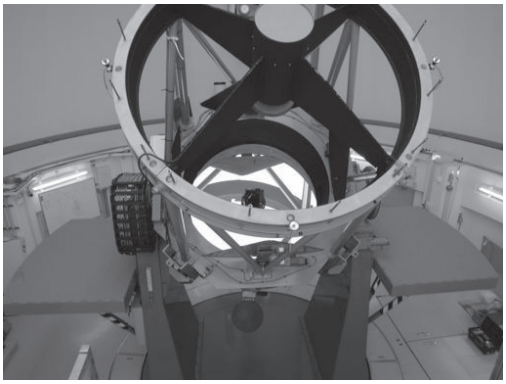

Figure 3.32: Picture of the Kanata telescope (http://www.hiroshima-u.ac.jp/hasc/institution/). The height of the telescope is about 5.8 m.

Table 3.5: Features of the KANATA telescope.

Parameter	Value
Optics	Ritchey-Chretien System
Primary mirror diameter	1600 mm, Mass:983 kg
Primary mirror mass	983 kg
Combined F value	12.2
Focal length	183300 mm
Effective diameter	1500 mm
Scale at Focal Plane	$11.27'/\mathrm{mm}$
Mount	altazimuth mount

In this thesis, we explain the TRISPEC in detail. The TRISPEC was developed by

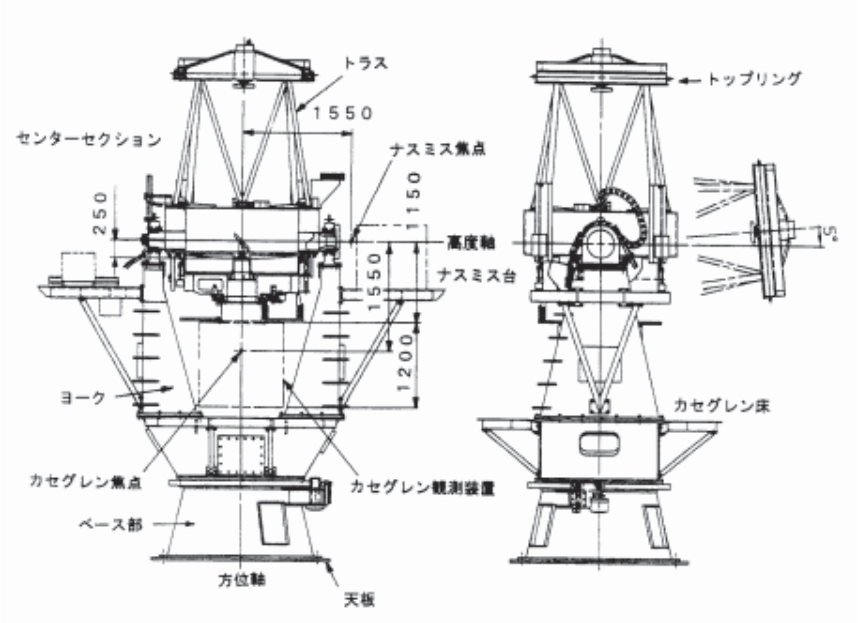

Figure 3.33: Schematic view of the Kanata telescope (http://www.hiroshima-u.ac.jp/hasc/institution/).

Nagoya University. It has four modes; imaging, spectroscopy, imaging-polarimetry, and spectro-polarimetry. Simultaneous observations can be performed in three channels; each channel are selected from optical (OPT) and near-infrared (IR1 and IR2) bands. The instrument is placed at the Cassegrain focus. The imaging capability of the TRISPEC is shown in table 3.6. The instrument for the OPT channel is a CCD camera using filters of the B, V, R, and I bands. The instrument for the two IR channels are InSb detector using filters of the J, H ($IR1$) and Ks, K, H_2 ($IR2$) bands. A more detailed description can be found in http://www.hiroshima-u.ac.jp/hasc/institution/.

Table 3.6: Imaging performance of the TRISPEC.

	OPT	IR1	IR2
Detector	CCD	InSb	InSb
Field of View		$7.0' \times 7.0'$	
Pixel Scale	$0.82''$/pixel	$1.65''$/pixel	$1.65''$/pixel
Filters	B, V, R, I	J, H	Ks, K, H_2
Limiting magnitude[a]	18.5	16.8	15.1

[a] The magnitude is obtained at a 10 sigma significance with an exposure time of 10 min.

3.5 KVA Telescope

The KVA telescope is a 0.6 m optical telescope in the La Palma island in Spain (figure 3.34). The KVA telescope is a remote monitoring telescope having a filter of the V band. The instrument put in the Cassegrain focus. It is used for monitoring observations for blazars (http://users.utu.fi/kani/1m/index.html). A more detailed description can be found shown in http://www.astro.utu.fi/telescopes/60lapalma.htm.

Figure 3.34: Picture of the KVA telescope (http://www.astro.utu.fi/telescopes/60lapalma.htm).

3.6 MAGIC Telescope

The Major Atmospheric Gamma-ray Imaging Cherenkov (MAGIC) Telescope is a single dish imaging atmospheric Cherenkov telescope. The telescope is located in the Canary Island in Spain, and has been operated since 2004. The MAGIC telescope placed at an altitude around 2200 m. It is an international telescope under collaboration among Germany, Italy, Spain, and Switzerland. It has one of the largest main reflector mirrors in the world with a diameter of 17 m, which is an assembly of nearly 1000 individual mirrors. The low energy threshold is 50–60 GeV at small zenith angles (Albert et al. 2008b). The effective area is with diameter of 1.05 m, corresponding to a field of view of 3.6 degree. It consists of 576 photomultiplier tubes, with a weight of about 600 kg. The effective quantum efficiency is 0.25–0.3 for all tubes. The performance of the MAGIC telescope is shown in table 3.7. A more detailed description can be found in http://magic.mppmu.mpg.de/magic/.

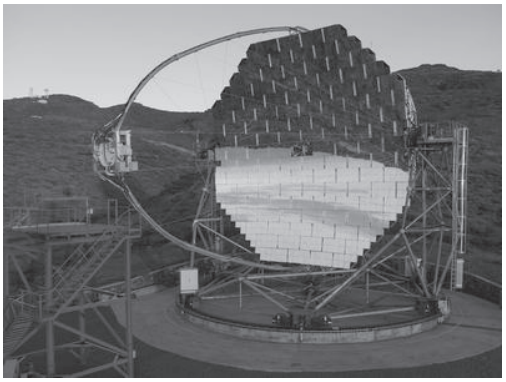

Figure 3.35: Picture of the MAGIC telescope (http://magic.mppmu.mpg.de/magic/).

Table 3.7: Performance of the MAGIC telescope.

Parameter	Value
Energy resolution	±22% at 150 GeV
Point spread function	0.1°
Energy threshold	50–60 GeV

Chapter 4

Observational Study on the blazar OJ 287

Contents

4.1 Observations and Results

4.1.1 Target

At a redshift of $z = 0.306$ (Stickel et al. 1989), OJ 287 is one of the archetypical and most studied blazars. An outstanding characteristic of the object is its recurrent optical out-

bursts with a period of 11.65 years, as revealed by optical data spanning more than 100 years (Sillanpaa et al. 1988). The outburst in 1994 motivated a worldwide multi-wavelength observation campaign named "The OJ 94 project" (Sillanpaa et al. 1996a). This project confirmed the periodicity and revealed that the optical outbursts consist of two peaks corresponding to flares with an interval of about one year (Sillanpaa et al. 1996b). OJ 287 is suggested to be a binary black hole system in which a secondary black hole goes through the accretion disk of the primary black hole and produces two impact flushes per period (Valtonen et al. 2008b) (figure 4.1). Interestingly, the first flare exhibited a low radio flux with decreasing radio polarization and a relatively short duration (a few months), and the second one had a high radio flux with increasing radio polarization, and lasted about half a year (Sillanpaa et al. 1996b; Valtaoja et al. 2000; Pursimo et al. 2000). The differences between the two flares may be interpreted with the idea that the first flare has a thermal origin in the vicinity of the black hole and the accretion disk, while the second one originates from the synchrotron radiation from the jet (Valtaoja et al. 2000). However, we have not yet obtained any convincing evidence supporting this interpretation.

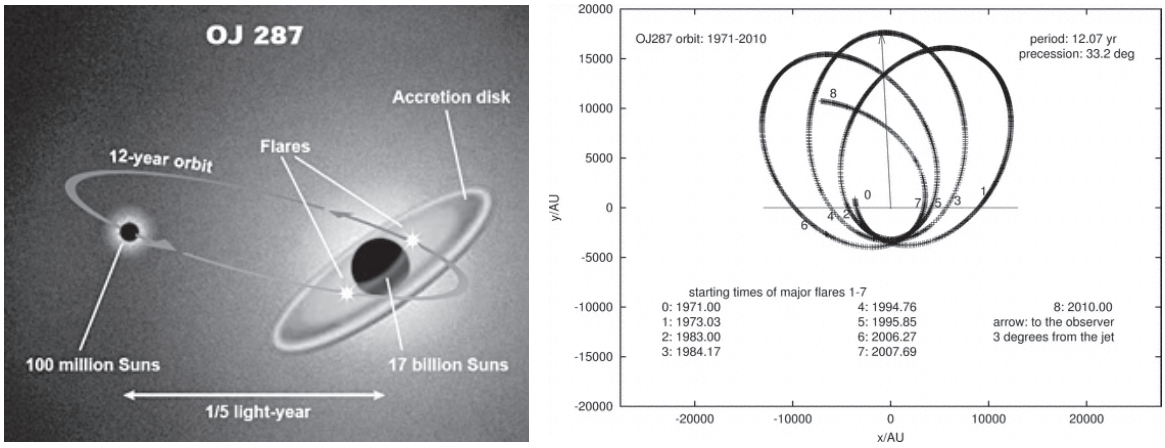

Figure 4.1: OJ 287 precessing binary model. Schematic view (left, http://www.skyandtelescope.com/news/13731992.html) and simulated orbit (Valtonen et al. 2006).

In the period between 2005 and 2008, OJ 287 was predicted to move to latest active phase, and was in fact reported exhibiting the first optical outburst in 2005 November (Valtonen et al. 2008b,a). Figure 4.3 shows light curve of OJ287 between 2003 and 2012. Since the second flare of the source was expected to be in the fall of 2007 (Valtonen et al. 2006; Kidger 2000), we organized two X-ray and simultaneous multi-wavelength observations, in

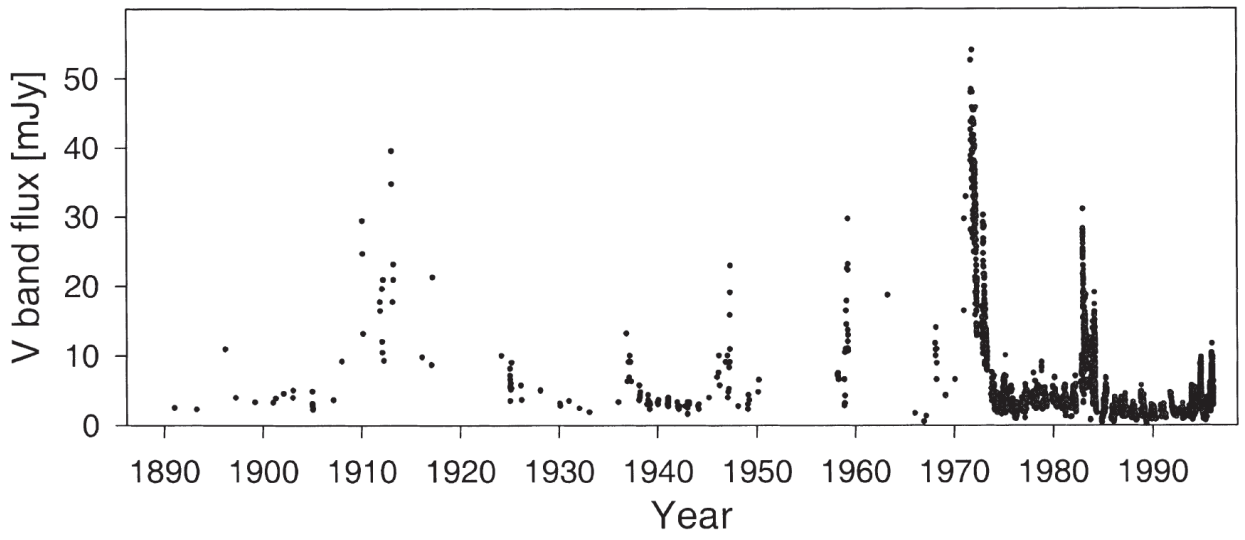

Figure 4.2: Long light curve of OJ 287 spanning more than 100 years. The data is V-band flux. The data are obtained with a variety of telescopes and observing technique.

the intervenient quiescent state (MWL I) and in the following second flaring state (MWL II). These observation were planned with the objective to reveal the characteristics of the second flare in comparison with the quiescent state and with the reported result form the first flare.

The Suzaku X-ray observation in MWL I was conducted during 2007 April 10 – 13, when the source was optically quiescent with an R-band magnitude of about 15. We triggered the MWL II Suzaku observation in 2007 November 7, on condition that the object remained brighter than 14-th magnitude for more than one week, as indicated by the optical monitoring data of the source taken at the Tuorla Observatory and the KVA observatory [1]. We also conducted monitoring observations at radio, optical, and VHE γ-ray frequencies with the NMA, the KANATA telescope, and the MAGIC telescope, respectively.

4.1.2 X-ray Observations and data reduction

The Suzaku pointing observation for MWL I was conducted between 19:47:00 UT 2007 April 10 and 11:10:19 UT 13 April (ObsID 702009010), and the pointing for MWL II was conducted between 11:24:00 UT 2007 7 November and 21:30:23 November 9 (ObsID 702008010). The XIS and the HXD onboard Suzaku were operated in the normal clocking mode with no

[1] http://users.utu.fi/kani/1m/OJ_287_jy.html

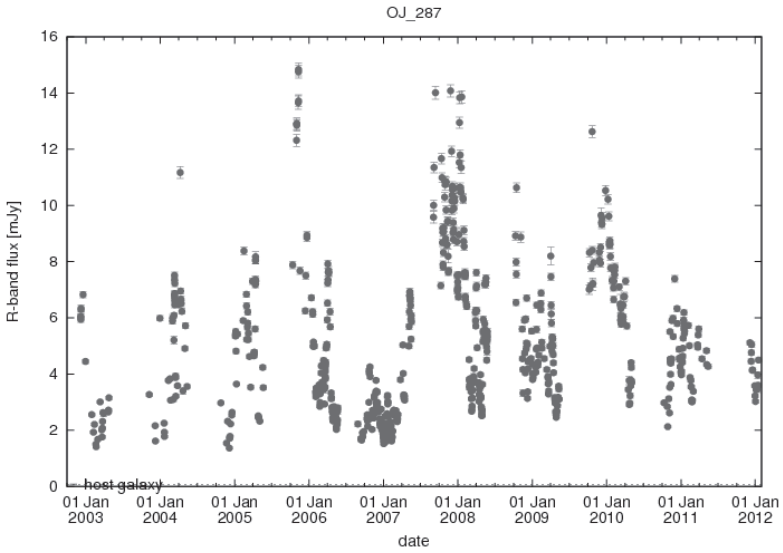

Figure 4.3: Light curve of OJ 287 at the active phase between 2005 and 2008. The data are R-band flux, which is obtained from the Tuorla Observatory.

window option, and in the normal mode, respectively. We placed OJ 287 at the HXD-nominal position (Serlemitsos et al. 2007).

We retrieved the pipeline products and processed the data using the HEADAS software package version 6.5.1 and the latest CALDB as of the XIS, the XRT, and the HXD as of 2008 September 5, 2008 July 9, and 2008 August 11, respectively. We removed events taken during South Atlantic Anomaly passages, the elevation angles from the day and night Earth respectively below 20 and 5 degrees for good-time intervals and events with the ASCA grades 1 and 7 for grade filtering. After these procedures, we obtained 85.3 ks and 102.6 ks of good exposures for XIS, and 93.6 ks and 102.9 ks of that for HXD, for MWL I and MWL II, respectively.

4.1.3 X-ray results

4.1.3.1 XIS Results

Figure 4.4 shows the 0.5 – 10 keV XIS images in MWL I and MWL II. OJ 287 was clearly detected at the position of $(\alpha, \delta) = (08\mathrm{h}54\mathrm{m}48\mathrm{s}.87, 20°06'30''.6)$ in the equinox J2000.0, with

no other apparent contaminating source within the XIS field of view. The image indicates that the intensity of the source was higher in MWL II than in MWL I. We accumulated the source signals within the solid circles with a radius of 3′ in figure 4.4. The background events were integrated within the same radius (dashed circles) at symmetric positions around the optical axis of the XRT.

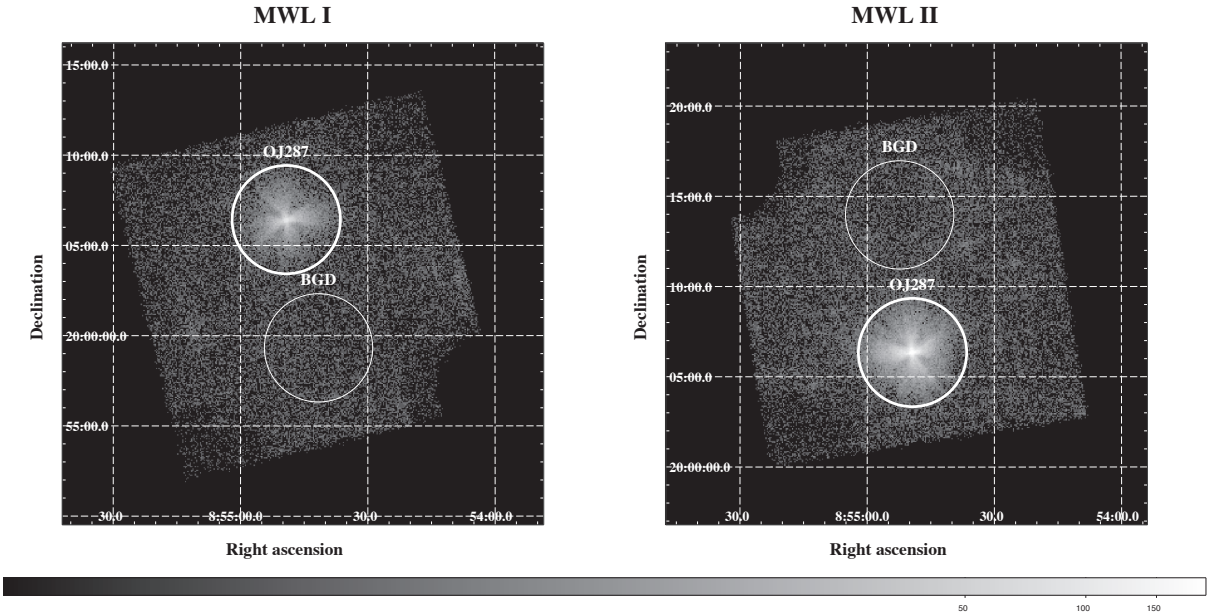

Figure 4.4: The 0.5 – 10 keV XIS image of OJ 287 in MWL I (left) and MWL II (right). Data from all XIS CCD chips (XIS 0, 1, and 3) were summed up. The region of the calibration sources was removed. Background subtraction and exposure correction are not applied to the image. Both panels are drawn in the same grayscale. The source and the background signals are integrated within the solid and dashed circles, respectively.

In figure 4.5, we show the background-subtracted X-ray lightcurves of OJ 287 in MWL I and MWL II as obtained with the two FI CCD cameras (XIS 0 and 3). In MWL I, the time-averaged count rates in the soft (0.5 – 2 keV) and medium (2 – 10 keV) bands were measured to be 0.088 ± 0.001 cts s^{-1} and 0.071 ± 0.001 cts s^{-1}, respectively, while they nearly doubled to 0.166 ± 0.001 cts s^{-1} and 0.164 ± 0.002 cts s^{-1} in MWL II. With $\chi^2 = 42.9$ and 27.7 for 39 d.o.f., the lightcurve indicates no significant variation during MWL I in both energy bands. On the other hand, in MWL II, we found that the source flux gradually decreased by a factor of 1.3 in the first half of the observation ($\sim$ 1.5 days; χ^2/d.o.f. = 58.5/37 and 71.3/37 in the soft and medium bands). However, the hardness ratio, which was simply

calculated by dividing the count rate of the medium band by that of the soft band, indicates no significant spectral variation in both observations. Therefore, we evaluated the averaged spectra as presented below.

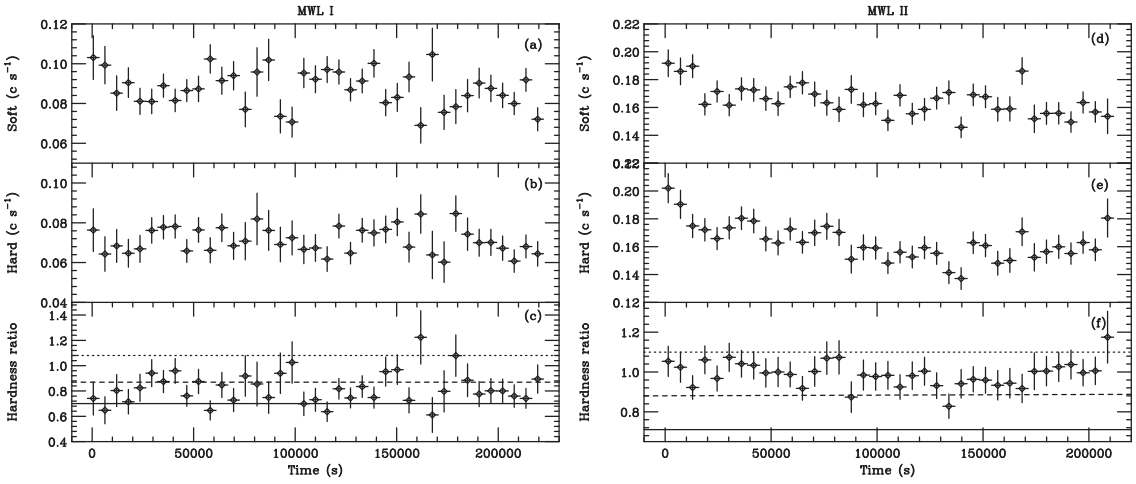

Figure 4.5: The XIS FI lightcurves of OJ 287 obtained in MWL I and MWL II. The time bin was set to 5760 s. Panels (a) and (d) show the soft energy band lightcurves (0.5 – 2 keV), while panels (b) and (e) show the medium energy band lightcurves (2 – 10 keV) in each observation. The hardness, which is simply calculated as the ratio of the medium band count rate to the soft band one, is shown in panels (c) and (f). The dotted, dashed, and solid lines in panels (c) and (f) indicate the predictions provided by the absorbed PL model with $N_H = 2.56 \times 10^{20}$ cm^{-2}, Γ=1.4, 1.6, and 1.8, respectively.

Figure 4.6 shows the background-subtracted XIS spectra of OJ 287, without deconvolving the instrumental response. In this case, significant X-ray signals were detected in the range of 0.5 – 10 keV and 0.4 – 8 keV, with the FI CCDs and the backside-illuminated (BI) CCD (XIS 1). The spectra appear to be featureless, without any absorption or emission lines.

We fitted the spectra with a single power-law (PL) model modified for photoelectric absorption. We calculated the redistribution matrix function and the auxiliary response file by using `xisrmfgen` and `xissimarfgen` (Ishisaki et al. 2007), respectively. The effects of absorption caused by the presence of contaminants on the surface of the optical blocking filter of the CCD is taken into account in `xissimarfgen`. The FI and BI spectra were jointly fitted with a small correction factor between their model normalizations. Because we found that the fluxes from the BI and FI spectra were in good agreement within 7 %, we adopt the FI value. We fixed the absorption column density at the Galactic value ($N_H = 2.56 \times 10^{20}$

cm^{-2}; Kalberla et al. 2005). The PL model became acceptable, yielding the best-fit photon index of $\Gamma = 1.65 \pm 0.02$ and $\Gamma = 1.50 \pm 0.01$ for MWL I and MWL II, respectively (table 4.1). Thus, we found that OJ 287 showed a harder X-ray spectrum in MWL II. As indicated in the lightcurve (figure 4.5), the flux density of the source in MWL II (404^{+6}_{-5} nJy) was higher than that in MWL I (215 ± 5 nJy) by a factor of 2.

Table 4.1: Summary of model fitting to the Suzaku XIS spectra.

obs	Models	$N_{\rm H}^{*}$	Γ	$S^{\dagger}_{\rm 1keV}$	$\Gamma^{\ddagger}$	$S^{\dagger\ddagger}_{\rm 1keV}$	χ^2/d.o.f.	$F^{\S}_{\rm 2-10keV}$
MWL I	PL	2.56$^{\parallel}$	1.65 ± 0.02	215 ± 5	–	–	215.0/243	1.44×10^{-12}
MWL II	PL	2.56$^{\parallel}$	1.50 ± 0.01	404^{+6}_{-5}	–	–	566.3/520	3.42×10^{-12}
	double PL	2.56$^{\parallel}$	$1.50^{+0.01}_{-0.02}$	404^{+4}_{-9}	2.62$^{\#}$	< 8.7	566.4/519	3.42×10^{-12}

* in 10^{20} cm^{-2}.

† X-ray flux density at 1 keV, in units of nJy.

‡ Soft PL component parameter.

§ 2 – 10 keV flux in erg cm^{-2} s^{-1}.

$^{\parallel}$ Fixed at the Galactic Value.

$^{\#}$ Fixed.

4.1.3.2 HXD Results

It is crucial to evaluate the non-X-ray background (NXB), before examining the hard X-ray spectrum observed with the HXD-PIN (Takahashi et al. 2007; Kokubun et al. 2007). Although the NXB varies under various cosmic ray environments in the orbit, the HXD team revealed a set of control parameters for reproducing the NXB and supplied simulated NXB event files for each observation. The latest version of the NXB model, named "tuned"-NXB (LCFITDT in Fukazawa et al. 2009), was reported to have a systematic reproducibility error of 2.31 % and of 0.99 % with 10 ks and 40 ks exposures, respectively, in the 15 – 40 keV band.

First, we analyzed the HXD-PIN data in MWL I. Since the data during Earth occultation is essentially dominated by the NXB events, these data were utilized to evaluate the reproducibility of the NXB model. The data were obtained with the same criteria as in the case of the on-source observation (section 4.1.2), with the exception that ELV $< -5^{\circ}$ instead of ELV $> 5^{\circ}$. The exposure of 44.1 ks was obtained under these conditions. Figure 4.7

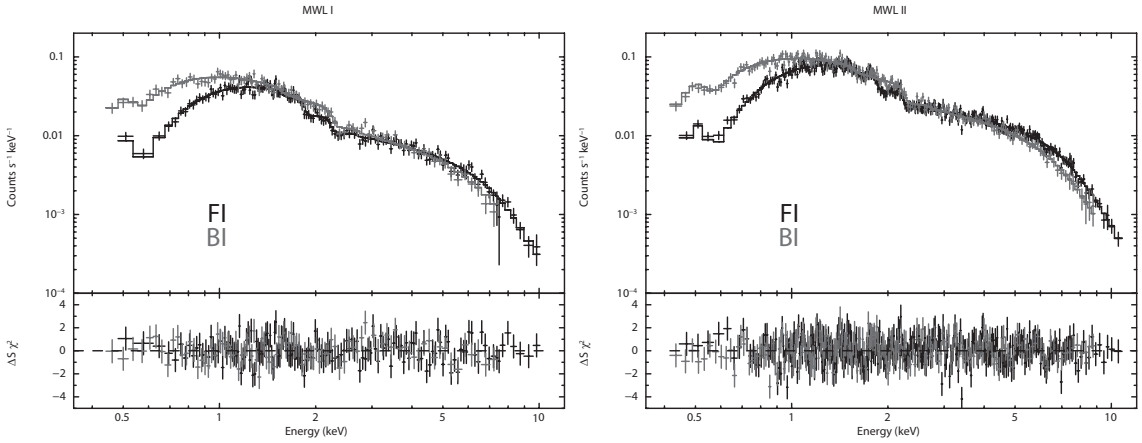

Figure 4.6: The XIS spectra of OJ 287 in MWL I and MWL II. The FI and BI data are shown with black and red points, respectively. The data are binned with at least 100 events, and error bars represent 1 σ statistical errors. Histograms in both panels indicate the best-fit PL models.

(a) compares the observed Earth-occultated (black), the NXB model (red), and the NXB-subtracted (green) spectra. Table 4.2 summarizes the statistics of the data and the NXB model in MWL I. We found a data excess of 3.8 ± 1.0 % over the NXB model below 20 keV. The apparent excess below 20 keV is within a 3 σ level of the current uncertainty of the NXB model (Fukazawa et al. 2009). Therefore, we consider that the excess is an artifact produced by fluctuations in the NXB model. In other words, the NXB model underestimates the real NXB data with ~ 4 % in this observation. It is necessary to take this into account for the on-source data.

In a similar manner, we compared the on-source and NXB model spectra, and the results are shown in figure 4.7 (b). We found a significant data excess over the NXB model, in the 12 – 40 keV range. This excess includes not only the source signals, but also those of the cosmic X-ray background (CXB). In order to evaluate the CXB component, we introduced the CXB spectrum within the HXD field of view as

$$F(E) = (9.412 \times 10^{-3}) \left(\frac{E}{1\mathrm{keV}} \right)^{-1.29} \exp\left[\frac{-E}{40\mathrm{keV}} \right] \text{ photons s}^{-1}\text{cm}^{-2}\text{keV}^{-1},$$

in accordance to Boldt (1987). We folded this spectrum with the HXD-PIN response of `ae_hxd_pinhxnome3_20080129.rsp` which was appropriate to the observation phase (Epoch 3), and show it in figure 4.7 (b). We also summarized the statistics of the data, the NXB, and the CXB in table 4.3. The NXB count rate for on-source is higher than that for the Earth

Table 4.2: Event statistics of the HXD data in MWL I.

	Earth occulation		On-source	
	12 – 20 keV	20 – 40 keV	12 – 20 keV	20 – 40 keV
Data (c s^{-1})	0.274 ± 0.003	0.149 ± 0.002	0.319 ± 0.002	0.173 ± 0.001
NXB (c s^{-1})	0.264 ± 0.001	0.150 ± 0.001	0.290 ± 0.001	0.167 ± 0.001
CXB (c s^{-1})	–	–	0.016	0.008
Excess (c s^{-1})[a]	0.010 ± 0.003	−0.015±0.002	0.012 ± 0.002	−0.002± 0.001
Excess [a] ratio[b] (%)	3.8 ± 1.0	−1.0 ± 1.3	4.2 ± 0.3	−0.9± 0.2
(Net signal)/NXB	–	–	0.042 ± 0.003	−0.009± 0.002

[a] Data excess over the NXB and the combined NXB and CXB for Earth occultation and on-source, respectively.

[b] Ratio to the NXB model.

occultation, due to different orbit conditions of the satellite, as can be seen in tables 4.2 and 4.3. Therefore, it is of no use to perform a direct comparison of the count rates between the Earth occultation and on-source periods, and therefore we examined the ratio of the combined NXB and CXB to the NXB. After subtracting the CXB and NXB models, the on-source data corresponded to 4.2 ± 0.3 % and −0.9±0.2 % of the NXB, in 12 – 20 keV and 20 – 40 keV, respectively. By using the Earth occultation data, we ascribed the apparent excess in 12 – 20 keV due to the uncertainly of the NXB model instead of the source signals since we confirmed that the NXB model underestimates the real NXB spectrum by ~ 4 %.

Next, in (a) in figure 4.8, we show the HXD-PIN spectra of MWL II during the Earth occultation with an exposure of 28.7 ks. Table 4.3 summarizes the statistics of the data and the NXB model during the Earth occultation. They are consistent with each other within 1.4±1.2% and 1.2±1.6% in 12 – 20 keV and 20 – 40 keV. Thus, we confirmed that the NXB model adequately reproduced the observed NXB spectrum in MWL II within its reported uncertainty.

Figure 4.8 (b) shows the on-source spectra in MWL II. In order to fold the CXB spectra, we used the HXD-PIN response function (Epoch 4), `ae_hxd_pinhxnome4_20080129.rsp`. The HXD-PIN spectrum revealed a significant excess over the combined CXB and NXB in the 12 – 27 keV range. The count rates for the data, the NXB and the CXB in this range, are shown in table 4.3. Thus, the excess has a count rate of 0.011 ± 0.002 cts s^{-1} (2.9 ± 0.6 % of the NXB), which corresponds to statistical significance of 5.0σ. Since this is well above

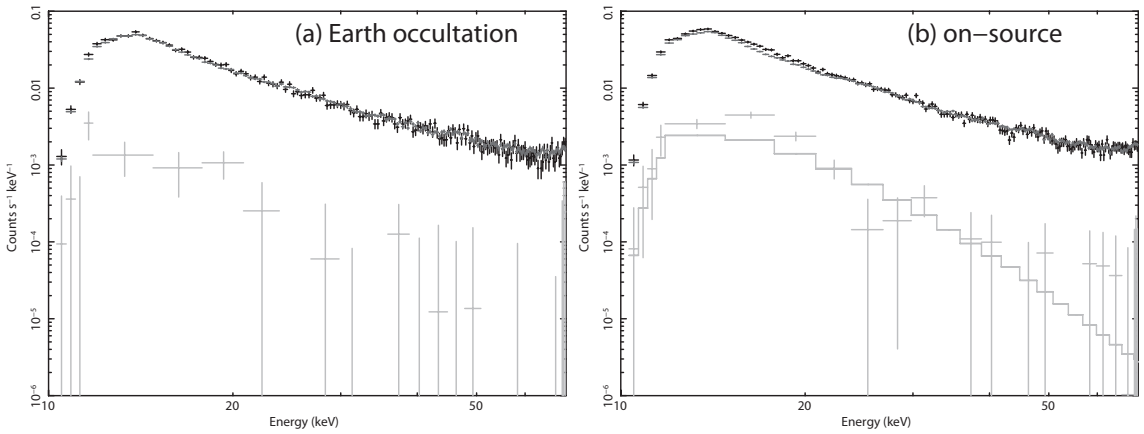

Figure 4.7: The HXD-PIN spectra of OJ 287 in MWL I, obtained in the Earth occultation (panel a) and the on-source observations (panel b). The black, red, and green data points indicate the data, NXB model, and NXB-subtracted spectra, respectively. The green histogram in panel (a) shows the CXB model spectrum (see the text).

the NXB errors, we concluded that the HXD-PIN detected signals from OJ 287 in MWL II.

Due to the rather low signal statistics of the HXD-PIN in comparison to the XIS, instead of joint fitting of XIS and HXD-PIN spectra, we compared the flux of the HXD-PIN signal to the fitting result of the XIS spectrum. The simple extrapolation of the best-fit single PL model to the XIS spectrum (section 4.1.3.1) has a count rate of 0.016 cts s^{-1} in 12 – 27 keV, after the correction of the relative normalization of the HXD to the XIS (1.14: Ishida 2007). The detected HXD-PIN count rate is only 0.65 times this value, which suggests the presence of a spectral break between the XIS and the HXD-PIN range.

4.1.4 Multi-wavelength Observations and Results

4.1.4.1 Radio Observations

Eleven radio observations of OJ 287 with the NMA at the Nobeyama Radio Observatory were carried out between January 2007 and January 2008. We performed simultaneous observations of radio continuum emission from OJ 287 at 86.75 GHz and 98.75 GHz with a 1 GHz bandwidth for each band. The total on-source time of OJ 287 in each observation was between nine and twelve minutes. In each observation session, OJ 287 and the bright

Table 4.3: Event statistics of the HXD data in MWL II.

	Earth occultation		On-source
	12 – 20 keV	20 – 40 keV	12 – 27 keV
Data (c s^{-1})	0.286 ± 0.003	0.165 ± 0.002	0.399 ± 0.002
NXB (c s^{-1})	0.290 ± 0.001	0.167 ± 0.001	0.367 ± 0.001
CXB (c s^{-1})	–	–	0.022
Excess (c s^{-1})[a]	−0.004± 0.003	−0.002 ± 0.003	0.011 ± 0.002
Excess[a] ratio[b]	−1.4± 1.2	−1.2± 1.6	2.9 ± 0.6
(Net signal)/NXB	–	–	0.029 ± 0.002

[a] Data excess over the NXB and the combined NXB and CXB for Earth occultation and on-source, respectively.

[b] Ratio to the NXB model.

reference amplitude calibrators (3C 84 or 3C 345) were observed alternately. The relative amplitude ratios between OJ 287 and these reference calibrators were obtained from the visibility data. As absolute flux-scale calibrations, Uranus or Neptune was used in order to calculate the final flux values of OJ 287. The uncertainties in the absolute flux scale were estimated to be about 15 % for each observation, taking into account statistical errors induced by noise and systematic errors caused by flux fluctuations of the reference calibrators.

For MWL I, we observed the source on 11 and 12 April, overlapping with the Suzaku pointing. The averaged flux of the two night observations was 1.73±0.26 Jy and 1.75±0.26 Jy at 86.75 GHz and 98.75 GHz, respectively. During the period of MWL II, the observations on November 7 and 8 were coincident with the Suzaku pointing. The averaged flux of the two day observations was 3.04 ± 0.46 Jy and 2.98 ± 0.45 Jy at 86.75 GHz and 98.75 GHz, respectively (see table 4.4). The measured radio flux for MWL II was 1.7 – 1.8 times higher than that for MWL I.

4.1.4.2 Optical Observations

Optical and near-infrared (NIR) photometric observations were performed at the Higashi-Hiroshima Observatory with the 1.5-m "KANATA" telescope. We obtained images of the field of OJ 287 with V, J, and K_s filters by using TRISPEC attached to the telescope (Watanabe et al. 2005). The V-band images were observed for 53 nights between 2006 Oc-

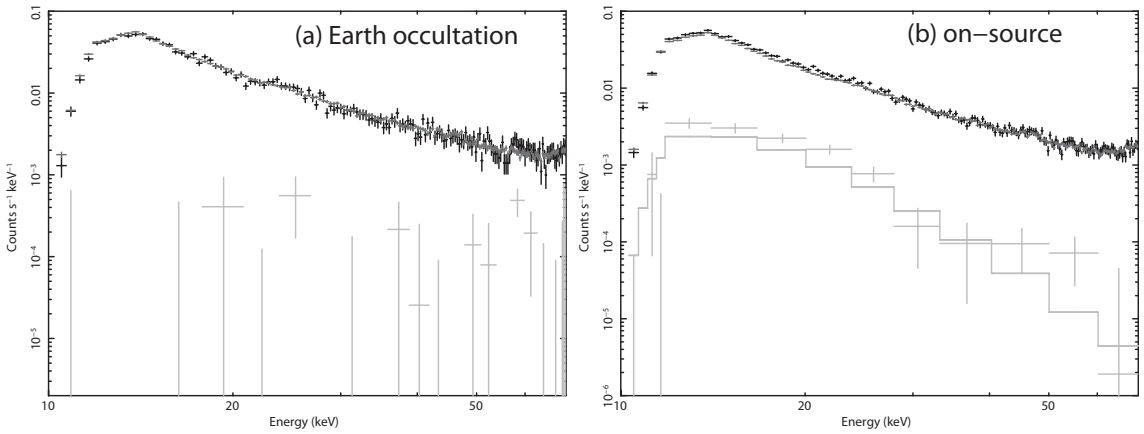

Figure 4.8: The HXD-PIN spectra of OJ 287 in MWL II, presented in the same manner as in figure 4.7.

Table 4.4: Summary of radio and optical fluxes obtained during the Suzaku pointing in MWL I and MWL II.

obs	radio flux (Jy)		optical flux (mJy)			
	86.95 GHz[a]	98.75 GHz[a]	K_s^b	J^b	R^c	V^c
MWL I	1.73 ± 0.26	1.75 ± 0.26	17.74 ± 0.33	8.82 ± 0.03	3.20 ± 0.05	3.03 ± 0.01
MWL II	3.04 ± 0.46	2.98 ± 0.46	$55.95^{+7.69}_{-6.76}$	27.02 ± 0.21	8.70 ± 0.14	8.93 ± 0.05

[a] NMA data
[b] KANATA data
[c] KVA telescope data

tober and 2007 December. For each night, we obtained ~ 20 images with an exposure time of 108 s for each frame. The magnitude of OJ 287 was measured by differential photometry with a neighbor comparison star located at $(\alpha, \delta) = (08\mathrm{h}54\mathrm{m}52.7\mathrm{s}, 20°04'46'')$. The V-magnitude of the comparison star ($V = 14.160$) was quoted from Skiff (2007). After producing dark-subtracted and flat-fielded images, we measured the magnitudes of the objects by aperture photometry using IRAF. We also checked the magnitude being constant for the comparison star by using another neighbor star at $(\alpha, \delta) = (08\mathrm{h}54\mathrm{m}59.0\mathrm{s}, 20°02'58'')$. The differential magnitude of the comparison star exhibited no significant fluctuation exceeding 0.003-th during our observations.

We also obtained NIR images for MWL I on 2007 April 11, 12, and 13, as well as for MWL II on November 7, 8, and 10, which overlapped with the Suzaku pointing. Si-

multaneous V, J, and K_s-band images were obtained for these six nights. The exposure times of each frame were 15 and 4 s for the J and K_s-band images, respectively. The reduction procedure was similar to that in the V-band data mentioned above, and we used the same comparison stars and target stars as those for the V-band data. The J and K_s magnitudes of the comparison star were quoted from the 2MASS catalog ($J = 12.664$ and $K_s = 12.090$; Skrutskie et al. 2006). We confirmed that the magnitude of the comparison star remained constant within 0.004 and 0.012 mag for J and K_s-bands during our observations. In MWL I, the averaged flux of three night observations was 3.03 ± 0.01 mJy, 8.81 ± 0.03 mJy, and 17.74 ± 0.33 mJy for V, J, K_s-band, respectively. In MWL II, these fluxes were 8.93 ± 0.05 mJy, 27.02 ± 0.21 mJy, and $55.95^{+7.96}_{-6.76}$ mJy, respectively. (see table 4.4). It can be seen that the source flux for MWL II is higher by a factor 3 as compared to that for MWL I. The optical data show a monotonous decrease in a time scale of ~ 4 days during MWL II by a factor of 1.3.

In addition, we obtained R-band frames from the KVA telescope simultaneously with Suzaku pointings. The exposure time was 180 s for each frame. Photometric measurements were conducted in differential mode, that is, by obtaining CCD images of the target and the calibrated comparison stars in the same field of view (Fiorucci & Tosti 1996). The magnitudes of the source and the comparison stars were measured using aperture photometry and the (color-corrected) zero point of the image as determined from the magnitude of the comparison star. Finally, the object magnitude was computed using the zero point and a filter-dependent color correction. After this, magnitudes were transferred into linear fluxes by using the formula $F = F_0 \times 10^{(mag/-2.5)}$, where mag is the magnitude of the object and F_0 is a filter-dependent zero point (the value $F_0 = 3080$ Jy is used in the R-band; Bessell 1979).

4.1.4.3 VHE γ-ray Observations

We used the MAGIC telescope to search for VHE γ-rays emission from OJ 287 during the MWL campaigns I and II.

In MWL I, MAGIC observed in 3 nights. The zenith angle of the observations ranges from 8° to 29°. The observations were performed in so-called ON-OFF observation mode. The telescope was pointed directly to the source, recording ON-data. The background was estimated from additional observations of regions where no γ-ray is expected, OFF-data, which were taken with sky conditions similar to ON-data. Data runs with anomalous trigger

rates due to bad observation conditions were rejected in the analysis. The remaining data correspond to 4.5 hours of ON and 6.5 hours of OFF data. In November and December 2007 for MWL II, MAGIC observed in a zenith angle range from 8° to 31° in the "wobble mode" (Fomin et al. 1994), where the object was observed at 0.4° offset from the camera center. With this observation mode, an ON-data sample and OFF-data samples can be extracted from the same observation run; in our case, we used 3 OFF regions to estimate the background. In total, the data were taken during 22 nights, two of which coincide with the Suzaku pointing. 41.2 hours of data from 19 nights passed the quality selection to be used for further analysis.

The VHE γ-ray data taken for MWLs I and II were analyzed using the MAGIC standard calibration and analysis software. Detailed information about the analysis chain is found in Albert et al. (2008b). In February 2007, the signal digitization of MAGIC was upgraded to 2 Gsamples s^{-1} FADCs, and timing information is used to suppress the contamination of light of the night sky and to obtain new shower image parameters (Aliu et al. 2009) in addition to conventional *Hillas* image parameters (Hillas 1985).

These parameters were used for γ/hadron separation by means of the "Random Forest (RF)" method (Albert et al. 2008a). The γ/hadron separation based on the RF method was turned to give a γ-cut efficiency of 70 %. Finally, the γ-ray signal was determined by comparing between ON and normalized-OFF data in the —ALPHA— parameter[2] distribution, in which the γ-ray signal should show up as an excess at small values. Our analysis requires a γ-cut efficiency of 80 % for the final —ALPHA— selection. The energy of the γ-ray events are also estimated using the RF method.

A search of VHE γ-rays from OJ 287 was performed with data taken for MWLs I and II in three distinct energy bins. No significant excess was found in any data samples. Upper limits with 95 % confidence level in the number of excess events were calculated using the method of Rolke et al. (2005), taking into account a systematic error of 30 %. The number of excess events was converted into flux upper limits assuming a photon index of -2.6, corresponding to the value used in our Monte-Carlo samples of γ-rays. The derived upper limits in the three energy bins for each period are summarized in table 4.5.

A search for VHE flares with a short-time scale was also performed with the data taken for MWL II. Figure 4.9 shows the nightly count rate of the excess events after all cuts

[2]the angle between the shower image principal axis and the line connecting the image center of gravity with the camera center.

including a SIZE cut above 200 photoelectrons, corresponding to an energy threshold of 150 GeV. Fitting a constant rate to the observed flux yields χ^2/d.o.f. = 25.55/18 (a probability of 11 %), and thus indicates no evidence of a VHE flare during this period.

Table 4.5: Results of the search for VHE γ-ray emissions from OJ 287.

MWL I			
Threshed energy (GeV)[a]	80	145	310
ON events[b]	40056	1219	42
OFF events[c]	40397 ± 226	1340 ± 38	39.5 ± 6.3
significance (σ)[d]	-1.13	-0.94	-0.47
U.L. of excess events[e]]	394	75.1	21.9
$\mathrm{Flux}_{95\%\mathrm{U.L.}}$ ($\times 10^{-12}$ cm^{-2} s^{-1}[f]	59.8	11.1	2.83
Crab flux(%)[g]	8.5	3.3	2.4
MWL II			
Threshed energy (GeV)[a]	85	150	325
ON events[b]	281885	12582	578
OFF events[c]	282342 ± 493	12573 ± 65	576 ± 14
significance (σ)[d]	-0.75	0.07	0.07
U.L. of excess events[e]	1218	330	71.6
$\mathrm{Flux}_{95\%\mathrm{U.L.}}$ ($\times 10^{-12}$ cm^{-2} s^{-1})[f]	22.1	5.64	1.18
Crab flux(%)[g]	3.4	1.7	1.1

[a] Correspond to peak energies of γ-ray Monte Carlo samples after all cuts.

[b] Number of measured ON events.

[c] Normalized number of OFF events and related error.

[d] Based on equation (17) in Li & Ma (1983),

[e] 95% upper limit of the number of excess events with 30% systematic error.

[f] Flux upper limit assuming a photon index of -2.6 for the calculation of the effective area.

[g] Corresponding Crab flux in each energy range based on measurements of the Crab pulsar performed with the MAGIC telescope (Albert et al. 2008b)

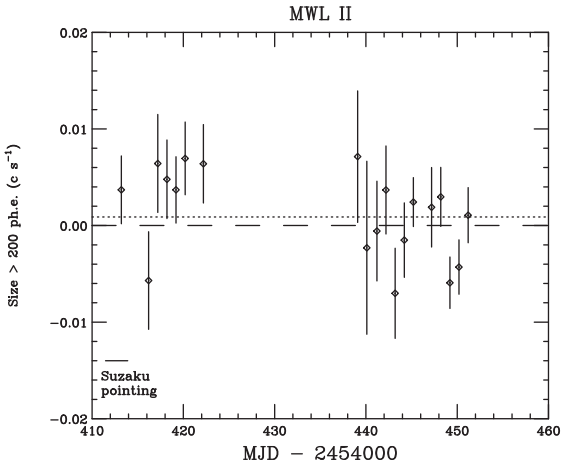

Figure 4.9: Excess event rate with SIZE above 200 photoelectrons (with a corresponding energy threshold of 150 GeV), observed with the MAGIC telescope in MWL II. The dotted line indicates the average count rate.

4.2 Discussion

4.2.1 Summary of the observational results

We performed Suzaku X-ray observations of OJ 287 in the quiescent state (MWL I) and the second flare (MWL II) in 2007 April and November, respectively, where the latter was the first X-ray observation during the second flare of the source. In cooperation with Suzaku, the radio, optical, and VHE γ-ray observations were performed with NMA, KANATA, and MAGIC, respectively. Figure 4.10 summarizes the multi-wavelength lightcurves obtained between September 2006 and January 2008. While the optical flux of OJ 287 was below 3 mJy in the V-band before MWL I, the brightness of the source started increasing after MWL I to become the flaring state ($>\sim$ 7 mJy) in September 2007. Although the radio flux gradually decreased around the period of MWL I, it started increasing during the optical flare in MWL II, and it also increased in other energy bands. We found that the brightness of the source increased by a factor of 2 – 3, in the radio, optical, and X-ray bands between MWL I and MWL II, although no significant VHE γ-ray signals were detected in either MWL I or MWL II.

As shown in figure 4.6, significant X-ray signals were detected with the XIS in the 0.5 – 10 keV range. The HXD-PIN detected hard X-ray signals in 12 – 27 keV with a significance of 5.0 σ in MWL II (figure 4.8), while those signals were not significant in MWL I (figure 4.7). The XIS spectra in 0.5 – 10 keV were described with a single PL model modified with Galactic absorption in MWL I and MWL II. The photon induces and the flux densities at 1 keV were derived as 1.65 ± 0.02 and 215 ± 5 nJy in MWL I, and 1.50 ± 0.01 and 404^{+6}_{-5} nJy in MWL II.

In the previous observations of the first flares, it was reported that the X-ray spectrum became softer as the source became brighter (Idesawa et al. 1997; Isobe et al. 2001). This tendency was interpreted as the domination of the IC component over the X-ray spectrum in the quiescent state. However, once the X-ray flux increases, the high-frequency end of the Synchrotron (SR) component extends to the X-ray band and exhibits a softer spectrum. In fact, Isobe et al. (2001) have successfully decomposed the X-ray spectrum obtained with ASCA at the first flare in 1994 into soft and hard PL components representing the SR and the IC components, respectively. Moreover, in the XMM-Newton observation of the recent first flare in 2005, the source exhibited a concave broken-PL-like X-ray spectrum (Ciprini & Rizzi 2008) which also supports the contribution from the soft component. The XMM

obtained 2–10 keV flux is 1.82×10^{-12} erg s^{-1} cm^{-3}, which is half of the Suzaku obtained flux. On the other hand, the spectral behavior in the second flare of OJ 287 observed with Suzaku was completely the opposite to the previous X-ray trend in the first flares.

In order to perform a quantitative evaluation of the possible soft excess component in the Suzaku X-ray spectrum obtained in MWL II, we employed an additional steep PL model modified with the Galactic absorption. The photon index of the additional steep PL component was fixed at 2.62, which is the best fit value for the first flare in 1994 (Isobe et al. 2001), while its normalization was left free. As a result of this two-component model fitting, the upper limit on the flux density of the additional soft PL component was derived as 8.7 nJy at the 3σ level (see table 4.1), while the hard component remained consistent with the best fit values for the single PL model fitting (χ^2/d.o.f. = 566.4/519). Thus, we obtained the upper limit on the ratio of the soft to the hard components at 1 keV as 0.022, although the ratio was estimated to be 0.186 ± 0.034 in the first flare of 1994 (Isobe et al. 2001). Therefore, the contribution from the soft component in MWL II was negligible in comparison to that of the first flare, and the hard component fully dominated the XIS spectrum over the 0.5 – 10 keV range.

4.2.2 Multi-wavelength spectra

Figure 4.11 shows the overall SED of OJ 287 for the Suzaku pointing in MWL I and MWL II, including the optical R-band data from the KVA telescope, as well as some historical data. In the figure, we recognize two spectral components, which are typical of blazars. The low frequency SR component, extending from radio to optical frequencies, has a spectral turnover at around 5×10^{14} Hz. The X-ray spectrum exceeds the extrapolation from the optical SR spectra in both observations, which is consistent with the negligible soft PL component in MWL II discussed above. Therefore, we naturally attribute the observed hard X-ray spectrum to the IC component rising toward the higher frequency range. The HXD spectrum suggests that the spectral softening occurs above 10 keV, in comparison with the XIS spectrum in the 0.5 – 10 keV range. The SED indicates that both the SR and IC intensities increased from MWL I to MWL II without any significant shift of the SR peak frequency.

As a working hypothesis, here we assume simply that the variation of the SED was caused by a change in electron energy density (or number density) and/or the maximum

Lorentz factor of the electrons, with stable magnetic field, volume of emission region, minimum Lorentz factor, and break of electron energy distribution (e.g., Takahashi et al. 2000). In order to evaluate this hypothesis, we applied a one-zone SSC model to the SED by using the numerical code developed by Kataoka (2000). The electron number density spectrum was assumed to be a broken PL and the index of the electron spectrum (p) below the break Lorentz factor was determined by the X-ray photon index as $p = 2\Gamma - 1 = 2.3$ and 2.0, in MWL I and MWL II, respectively. We obtained the following seven free parameters to describe the observed SED: the Doppler factor (δ), the electron energy density ($u_{\rm e}$), the magnetic field (B), the blob radius (R), and the minimum, break, and maximum Lorentz factor of the electrons ($\gamma_{\rm min}$, $\gamma_{\rm break}$, and $\gamma_{\rm max}$, respectively). Adopting the optical variability time scale ($T_{\rm var} \sim 4$ days; section 4.1.4.2) in MWL II, the relation between δ and R should be subjected to $R < cT_{\rm var}\delta/(1+z) = 1.2 \times 10^{17}(T_{\rm var}/4{\rm days})(\delta/15)$ cm where c and z are the speed of light and the redshift of the source, respectively.

We derived the SSC model parameters as summarized in table 4.6. The resultant model curves are shown with solid lines in figure 4.11. The model for MWL II appears to reproduce the spectral steepening in the HXD-PIN range, although the both model predictions are well below the upper limit on the VHE γ-ray spectra. The SED in MWL I was reproduced with $\delta = 15$, $B = 0.71$ G, $R = 7.0 \times 10^{16}$ cm, $\gamma_{\rm min} = 70$, $\gamma_{\rm break} = 700$, $\gamma_{\rm max} = 3300$, and $u_{\rm e} = 1.5 \times 10^{-3}$ erg cm^{-3}. The δ and R are typical values for LBL (Ghisellini et al. 1998). On the other hand, in the SED in MWL II, the SSC model with $u_{\rm e} = 2.1 \times 10^{-3}$ erg cm^{-3} and $\gamma_{\rm max} = 4500$ was found to describe the SED successfully, while the other parameters remained unchanged. Thus, we adopt the interpretation that the increase in the electron energy density produced the second flare.

4.2.3 Difference of the first and second flare

The SED spectra obtained in first and second flare during 2005 – 2008 outburst are suggested to have different features as we saw in the X-ray spectra obtained with XMM-Newton and Suzaku. The flux increase between those flare indicates that the jet in the second flare is more active than that in the first flare. The X-ray soft excess in the first flare is suspected to be possibility of not only synchrotron radiation but also thermal emission from the disk (Ciprini & Rizzi 2008). The difference in these SED spectra may require not only simple 'disk impact' (Valtonen et al. 2008b), but also a state transition of the disk - jet system (Valtaoja et al. 2000).

Table 4.6: Physical parameters for the SSC model.

parameters[a]	MWL I	MWL II
δ	15	
R (cm)	7.0×10^{16}	
B (Gauss)	0.71	
$\gamma_{\rm min}$	70	
$\gamma_{\rm break}$	700	
$\gamma_{\rm max}$	3300	4500
p	2.3	2.0
$u_{\rm m}$ (erg cm^{-3})	2.0×10^{-2}	2.0×10^{-2}
$u_{\rm e}$ (erg cm^{-3})	1.5×10^{-3}	2.1×10^{-3}

[a] Notations are described in the text.

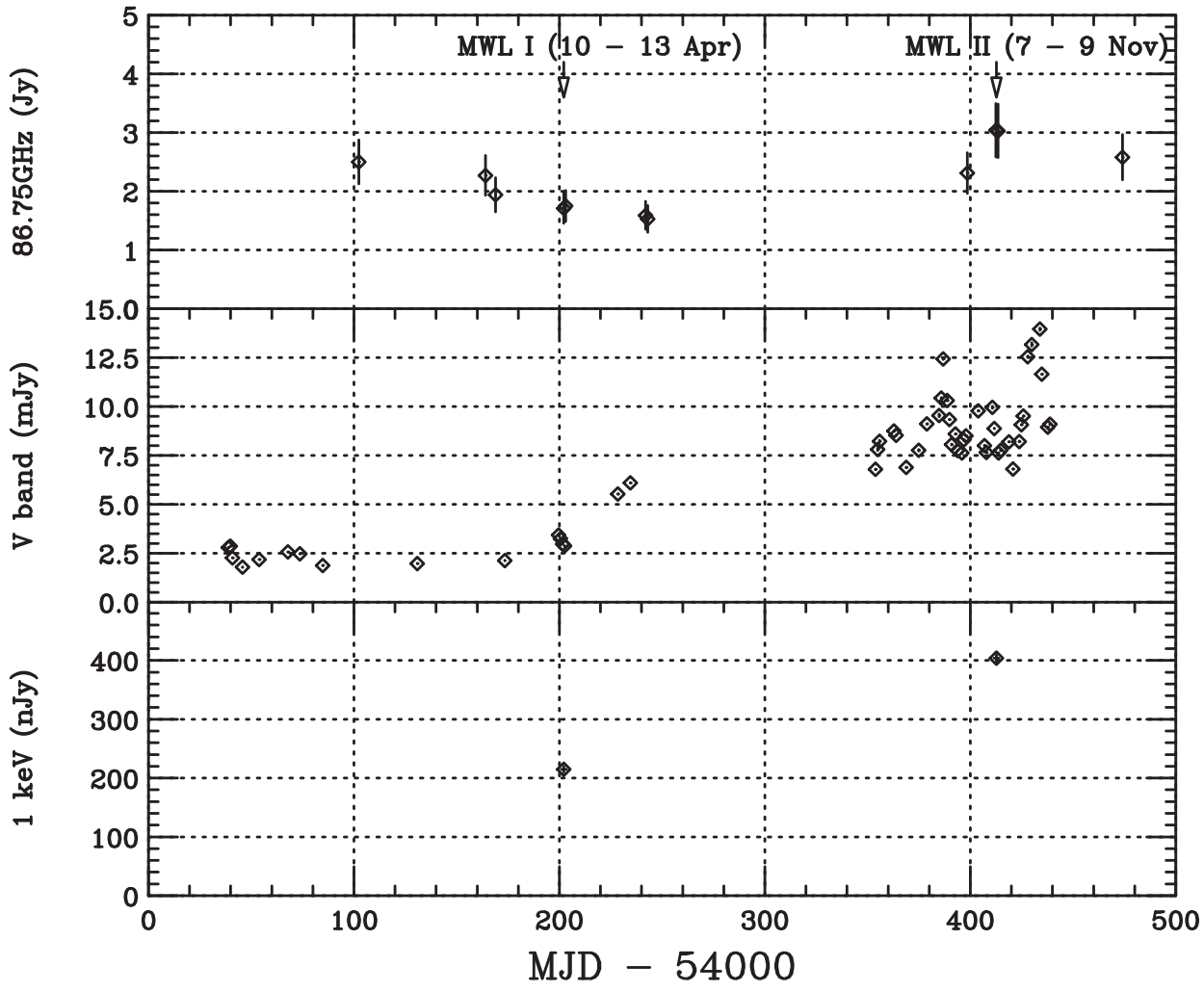

Figure 4.10: The multi-wavelength lightcurves of OJ 287. The top panel shows the radio flux at 86.75 GHz as observed with NMA, while the middle panel shows the optical flux in the V-band as observed with KANATA. The radio and optical fluxes are averaged over each night. The bottom panel shows the X-ray flux density at 1 keV. Arrows indicate the Suzaku pointings in MWL I and MWL II.

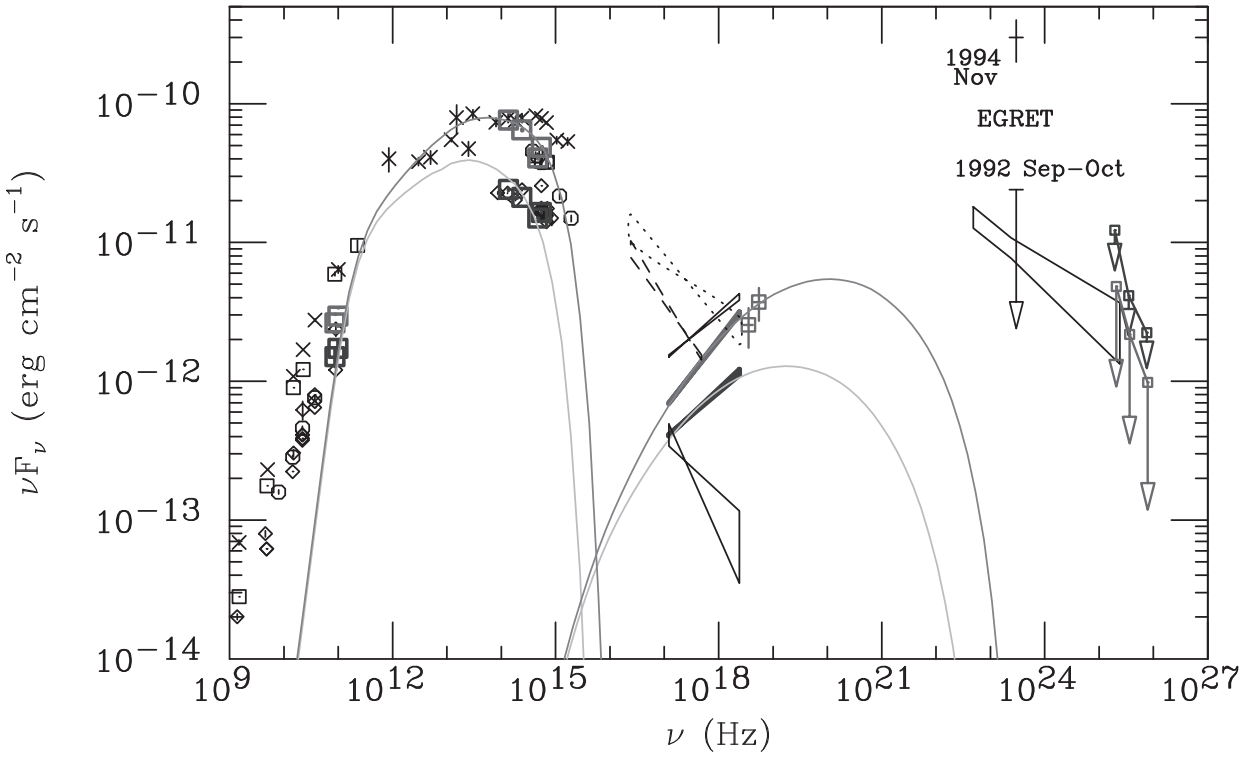

Figure 4.11: The SED of OJ 287 during the Suzaku observations in MWL I (blue) and MWL II (red). The radio and optical data are shown with squares and, the X-ray data are shown with bow ties. The upper limit of the VHE γ-ray spectrum are measured values, shown with downward arrows. The light blue lines and the purple lines indicate the simple one-zone SSC model for MWL I and MWL II, respectively. The black data points show radio, optical, and γ-ray data from non-simultaneous observations. The X-ray spectra with EXOSAT, ROSAT, and ASCA are drawn with dotted, dashed, and solid lines, respectively (Idesawa et al. 1997; Isobe et al. 2001 and references therein). The γ-ray spectrum obtained with Fermi during the first 3 month observation (August – October 2008) is shown with a bow tie (Abdo et al. 2009).

Chapter 5

Observational Study on the radio lobe of Fornax A

Contents

5.1 Observations and Results

5.1.1 Target

Fornax A (NGC 1316) is one of the closest and brightest radio galaxies with a distinctive two-sided lobe structure. It is the brightest in the GHz band (Ekers et al. 1983) from the synchrotron emission by accelerated electrons interacting with the magnetic field (figure 5.1 right). It is one of the few samples to have a difference of the polarization intensity between the north and south part. The south part of the lobe is depolarized to a higher degree (figure 5.1 left). It is also the first to be detected with the non-thermal X-rays from the inverse Compton emission by those interacting with the ambient radiation (mostly cosmic microwave background) field (Feigelson et al. 1995; Kaneda et al. 1995) (figure 5.2). In addition, it is the first to be detected with hard X-ray ($\sim$ 20 keV) form the lobe (figure 5.3). It is evident that the electron distribution of the synchrotron and inverse Compton radiation is the same ($\gamma \sim 10^3$). However, Fornax A is somewhat atypical in its energy balance; the ratio of the energy density between the accelerated electrons ($u_{\rm e}$) and the magnetic field ($u_{\rm m}$), which can be derived with the detections of both synchrotron and inverse Compton emission, is lower than other radio lobes (eg., Isobe et al. 2011a). This may have something to do with the unique evolutionary stage of Fornax A; its powering black hole in the NGC 1316 galaxy is considered to have ceased its activity some 3 Gyr ago for its unusually low X-ray brightness at present (Iyomoto et al. 1998). Radio lobes with no energy supply are destined to fade into oblivion as the population of accelerated charged particles loses their energy via radiative cooling and thermalization via Coulomb interactions. Perhaps because the energy supply has ceased quite recently in Fornax A, the emission from accelerated electrons is still visible using the remaining energy deposited into the system while the black hole was still active.

One of the features only seen in Fornax A is the possible presence of diffuse thermal X-ray emission inside the lobe. In addition to the diffuse non-thermal X-ray emission due to the inverse Compton emission, all previous X-ray studies have consistently suggested that the thermal emission is present in the spectra taken from both sides of the lobe (Feigelson et al. 1995; Kaneda et al. 1995; Tashiro et al. 2001; Isobe et al. 2006; Tashiro et al. 2009).

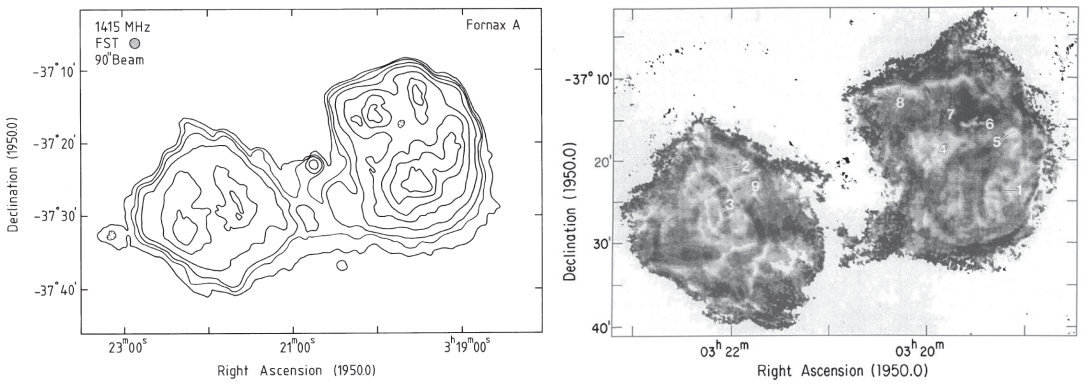

Figure 5.1: The 1.4 GHz intensity map (left; Ekers et al. 1983) and the polarization map (right; Fomalont et al. 1989). In the left panel, the contours are at 125, 187.5, 250, 375, 625, 875, 1125, and 1375 mJy/beam. In the right panel, the percentage is the linear polarization. The contrast of the image is linear between 5 % (white) to 40 % (black).

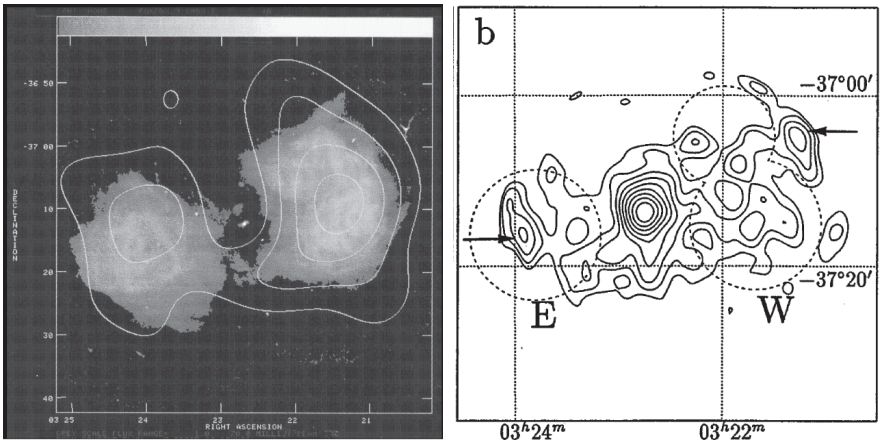

Figure 5.2: Image of the first X-ray detection in the Fornax A western lobe. The contour, which is 0.9-2.0 keV band, is observed with the ROSAT satellite (left; Feigelson et al. 1995. The gray-scale image is the 1.4 GHz map obtained with the Very Large Array (Fomalont et al. 1989. The contour, which is 1.5-7.0 keV band, is observed with the ASCA satellite (right; Kaneda et al. 1995.

The presence of the diffuse thermal emission in Fornax A is distinctively different from other objects, in which X-ray spectra require a thermal component (3C XX ...). In all these objects other than Fornax A, the thermal emission is attributable to the interstellar plasma emission of the host galaxy. In Fornax A, however, the host galaxy and the lobe are spatially resolved for its apparently large size, thus X-ray spectra of the lobe can be

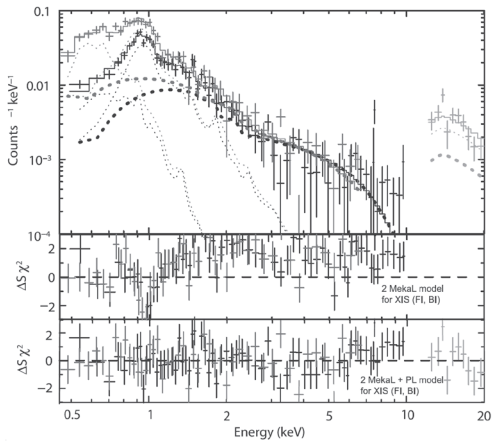

Figure 5.3: The 0.5-20 keV spectrum obtained with the Suzaku satellite (Tashiro et al. 2009).

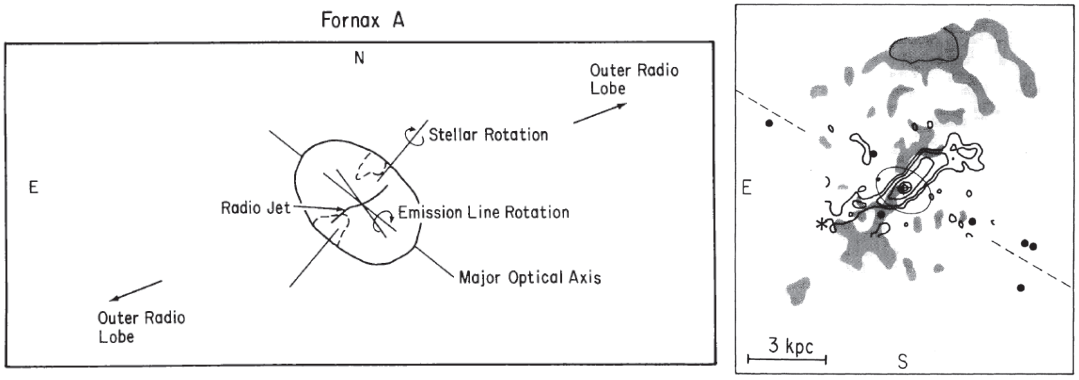

Figure 5.4: The orientation of various features of the sketch showing (left; Ekers et al. 1983)) and it superimposed on the 4 ″resolution radio map at 1.5 GHz (right; Geldzahler & Fomalont 1984)). In the left panel, the ellipse is the outline of the elliptical galaxy with the prominent dust patches indicated by dotted lines. In the right panel, the cross marks the optical core, the ellipse marks an approximate optical isophote, the dashed line marks the major axis of the spheroid, and the dots are unresolved optical knots.

extracted separately from the host galaxy.

If the diffuse thermal emission is present in Fornax A, it indicates the existence of diffuse plasma in the lobe. Such a plasma is certainly a major energy reservoir and plays a non-negligible role in the energy balance in the lobe. Nevertheless, the diffuse thermal emission was recognized as “ambient thermal emission” (e.g., Tashiro et al. 2009) and has never drawn much attention.

5.1.2 Observations and Data Reduction

5.1.2.1 Suzaku

We performed six points of mapping observations of the western lobe associated with the radio galaxy Fornax A, using the Suzaku satellite (Mitsuda et al. 2007). Suzaku carries two operational instruments: the XIS and the HXD. We concentrate on the XIS data in this thesis.

The field of views in this mapping observations are shown in figure 5.5, while the observation details are summarized in table 5.1. Two observations were carried out in 2006 and the remaining four in 2009. A part of the results from the earlier data was presented in Tashiro et al. (2009) using the data set obtained from the center inner most region of the western lobe (sequence ID 801014010 in figure 5.5). All of these observations are carried out with XIS normal operation mode. In this thesis, we assemble the additional sets taken in the flanking fields to cover the entire western lobe and the host galaxy (NGC 1316) of Fornax A.

We retrieved the pipeline products and processed the data using the HEADAS software package[1] version 6.11 and the latest calibration database (CALDB) as of writing. We removed events taken during South Atlantic Anomaly passages, the elevation angles from the day and night Earth respectively below 20 and 5 degrees for good-time intervals and events with the ASCA grades 1 and 7 for grade filtering. The net exposure times are given in table 5.1.

5.1.2.2 XMM-Newton

We also retrieved the archival XMM-Newton data to supplement the Suzaku data for investigating point-like X-ray sources that are potential contaminating emission to the diffuse emission of interest (figure 5.1). The XMM-Newton satellite (Jansen et al. 2001) carries three X-ray instruments. We used the data taken with two imaging-spectroscopic instruments: the EPIC MOS and pn. The EPIC-MOS and the EPIC-pn were operated in the full-frame mode with the medium thickness filter. The large effective area and the sharp optics make the EPIC cameras sensitive to point-like sources, which serves complimentary to the Suzaku XIS data.

[1] See http://heasarc.gsfc.nasa.gov/lheasoft/ for detail.

Table 5.1: Suzaku and XMM-Newton data sets in the Fornax A.

Observatory	Sequence ID	Position (J2000.0)		Observation	t_{exp}*
		R. A.	DEC	start date	(ks)
Suzaku	801015010	03h22m40.4s	-37°12′10″	2006-12-22	86.7
	801014010	03h21m40.4s	-37°09′52″	2006-12-23	42.9
	804036010	03h20m53.3s	-37°02′03″	2009-06-08	54.8
	804037010	03h22m05.5s	-37°58′03″	2009-06-09	55.5
	804038010	03h21m25.9s	-37°18′39″	2009-06-30	47.0
	804038020	03h21m25.7s	-37°18′40″	2009-08-02	39.6
XMM-Newton	0602440101	03h21m29.3s	-37°11′30″	2009-06-25	59.5

[a] For Suzaku, the aim point is the center of the XIS field of view.

[b] The mean exposure time of the three XIS sensors for Suzaku and two MOS and one PN sensors for XMM-Newton.

In the data reduction procedure, we used the SAS software package[2] version 11.0.0. All the data were reprocessed using the XMM-Newton original tools based on the calibration database latest as of 2011 August 26. Upon standard screening, we further removed events taken during intervals of high particle background. The net exposure time is given in table 5.1.

5.1.3 X-ray images

Figure 5.6 shows the (a) XIS and (b) MOS images. The XIS images are in the 0.67–1.5 keV band are shown with a logarithmic scale to focus on the diffuse emission thermal plasma whose temperature of $kT \sim 1$ keV (Feigelson et al. 1995; Kaneda et al. 1995; Tashiro et al. 2001, 2009). The MOS image in the 0.2–10 keV band are shown in a linear scale to highlight point-like sources. We note that numerous point-like sources are recognized in the MOS image with the brightest one being the nucleus of NGC 1316 at the field edge. Beneath these point-like sources, it is evident that diffuse emission exists in the XIS image. The brightness distribution of the diffuse emission suggests that there are two spatial components; one is centered at NGC 1316 and the other is associated with the western lobe. In addition to these two components, there should be diffuse emission pervasive in the Fornax cluster to

[2]See http://xmm.esac.esa.int/sas/ for detail.

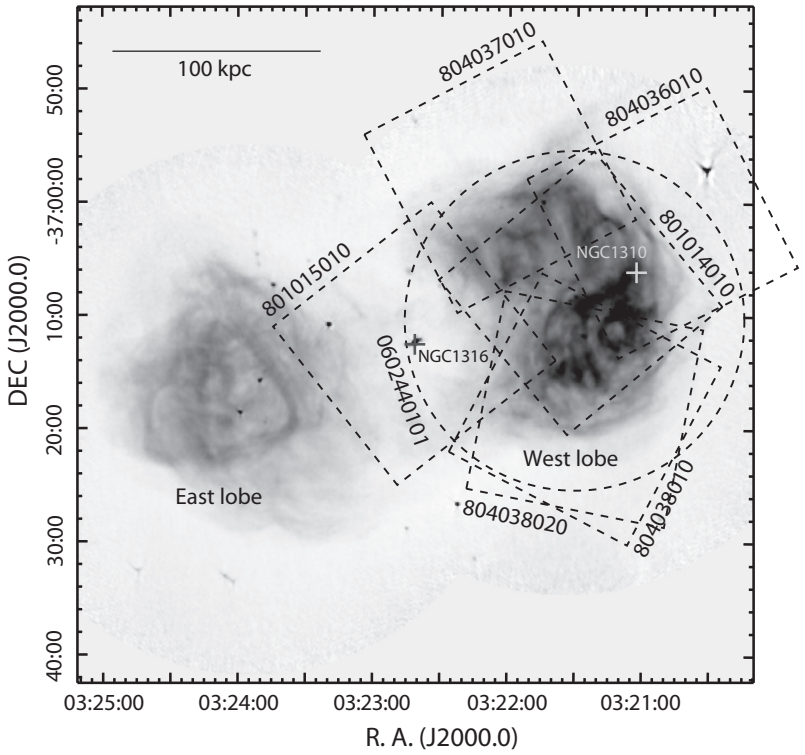

Figure 5.5: Mapping layout of the Suzaku observations over a 1.4 GHz radio intensity map in gray scale (Fomalont et al. 1989). The Suzaku XIS and the XMM-Newton MOS fields of view are shown with dashed squares and circles, respectively, with a sequence ID label in table 5.1. The positions of the powering source NGC 1316 is shown with a cross.

which the galaxy belongs. Since the galaxy is far from the core of cluster of galaxies, the distribution of the Fornax cluster component is expected to be almost uniform at the position of Fornax A thus is not apparently visible in figure 5.6. We hereafter call them "the galaxy component", "the lobe component", and "the cluster component", respectively.

In order to investigate the spatial distribution of the thermal and non-thermal emission from the western lobe, we defined four different patterns of regions: (1) the entire lobe region, which is called M (the blue ellipse region in figure 5.6), (2) the M region divided into north (MN) and south (MS), or west (MW) and east (ME), (3) the annulus regions divided with concentric circles around the lobe center: R1, R2, R3, and R4 (red regions), (4) the regions in (3) divided into north (R1N, R2N, R3N, R4N) and south (R1S, R2S, R3S, R4S).

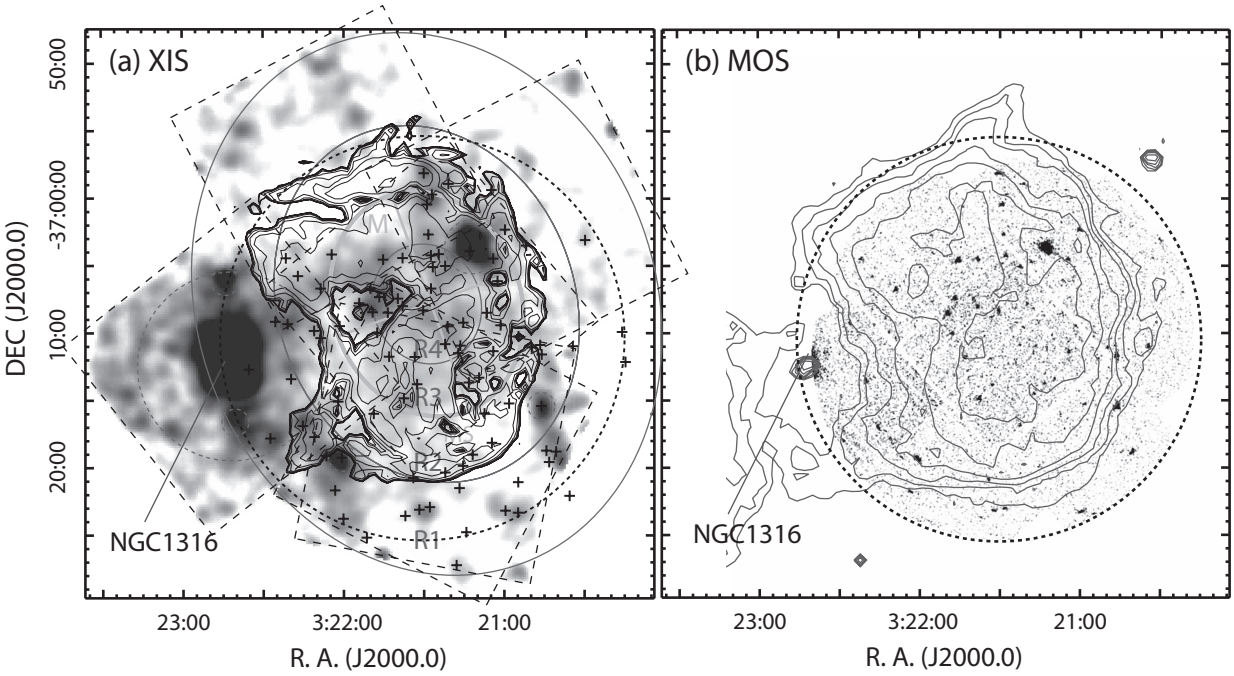

Figure 5.6: (a) Suzaku XIS and (b) XMM-Newton MOS2 images of the western lobe and NGC 1316. The XIS image is shown in the 0.67–1.5 keV band in a logarithmic scale to enhance the diffuse thermal emission, while the MOS image is shown in the 0.2–10 keV band in a linear scale to highlight point-like sources, listed in table 5.4. The contours indicate the (a) linear polarized and (b) linear intensity in 1.4 GHz (Fomalont et al. 1989). The source extraction regions for spatially-resolved spectroscopy (§ 5.1.5) are shown with cyan and red solid curves, while the masked regions around bright point-like sources are shown with red dotted curves. In the mosaic image of the XIS, FI events were merged, the difference in the exposure was corrected, and smoothed by a 50″ Gaussian convolution. In both images, the background was not subtracted.

5.1.4 X-ray Spectra (1) Background Emission

We proceed to characterize the spectral properties of the three components of the diffuse X-ray emission and their spatial distribution using the XIS. For the galaxy component, we refer to previous work by Kim et al. (1998); Kim & Fabbiano (2003); Konami et al. (2010).

As the emission of interest has a low surface brightness, we carefully subtracted background emission, which mainly consists of (1) non X-ray background (NXB), (2) the Galactic halo (GH), and (3) others of celestial X-ray diffuse background. In this subsection, we describe the approach to evaluate each component of background emission (§ 5.1.4.1–5.1.4.3.1). We apply the method to each spatial components in the next subsection (§ 5.1.5).

For the spectral fitting, we used the XSPEC package version 11. We generated the redistribution matrix functions (RMF) using the `xisrmfgen` tool[3], and the auxiliary response files (ARF) using the `xissimarfgen` tool[4] (Ishisaki et al. 2007). The response files and background spectra were generated for each sensor and each data set (table 5.1) separately at the positions of source extraction regions. The two FI spectra with XIS0 and XIS3 were merged for their nearly identical responses, while the BI spectrum was treated separately. When source spectra were extracted using multiple data sets, the source and background spectra and the response files were averaged with a weight of exposure times effective area using the `addascaspec` tool[5]. The fitting parameters were tied between the FI and BI spectra except for a normalization factor of a few percent to account for the internal calibration uncertainties.

5.1.4.1 NXB

The NXB event is caused mainly due to energy deposits by charged particles penetrating with the sensors, thus depends on the cut-off-rigidity of the satellite position at the time of observations (§3.1.3.6). The level of the NXB of the XIS is so low and stable that it can be reproduced by the accumulation of non-contemporary data taken while the satellite is pointed toward the night Earth. Using the `xisnxbgen` tool [6], we simulated the NXB spectrum by accumulating the night Earth data sorted in respect to the cut-off-rigidity Tawa et al. (2008)

[3]See http://heasarc.gsfc.nasa.gov/docs/software/ftools/fhelp/xisrmfgen.txt for detail.
[4]See http://heasarc.gsfc.nasa.gov/docs/software/ftools/fhelp/xissimarfgen.txt for detail.
[5]See http://heasarc.gsfc.nasa.gov/docs/software/ftools/fhelp/addascaspec.txt for detail.
[6]See http://heasarc.gsfc.nasa.gov/docs/software/ftools/fhelp/xisnxbgen.txt for detail.

demonstrated that this approach reproduces the NXB spectrum at an accuracy of $\sim$5% in the count rate.

For the FI spectra, we are able to make further fine-tune the normalization of the simulated NXB spectrum using instrumental spectral features as the calibrator, here we employed the most notable instrumental line Ni I Kα emission line at 7.47 keV. We derived the intensity of the emission line in both the actual and simulated spectra by phenomenologically fitting them with a power-law shaped continuum component plus a Gaussian line model in the 6.7–8 keV band. The free parameters in this model fitting were the power-law normalization and index, and the Gaussian normalization. In order to account for possible gain uncertainty, the center energy was set as a free parameter, and tied between the actual and simulated spectra. The incident line width of the Gaussian component was fixed to 0 eV. Figure 5.7 and table 5.2 show the 6.7–8 keV actual and simulated spectra for each region and the best-fit parameters, respectively. We rescaled the simulated NXB spectra so that the Ni I Kα line intensity became equal to that of the actual data, shown in table 5.2.

As for the BI spectra, the similar method that we employed for the FI spectra cannot be taken since the NXB level is much higher in the high energy end of the spectrum including the Ni I Kα line. Instead, we used the count rate in the 8–10 keV to derive the rescaling factor, in which the NXB emission dominates celestial X-ray emission. Table 5.3 shows the count rate for actual and simulated spectra and the rescaling factor for each region.

We evaluated the systematic uncertainty in subtracting the NXB to be a 1σ statistical uncertainty of the Gaussian normalization in the Ni I Kα line fitting for the FI spectra and the 1σ statistical uncertainty in the 8–10 keV count rate for the BI spectra.

Table 5.2: Summary of the Ni Kα line fitting for FI spectra[ab].

		actual			simulated				
Region	Energy[b]	Norm	Γ	$F_{\rm PL}$	Norm	Γ	$F_{\rm PL}$	χ^2/dof	ratio
	(1)	(2)	(3)	(4)	(5)	(6)	(7)		(8)
R1	$7.4790^{+0.0003}_{-0.0005}$	$7.30^{+0.24}_{-0.24}$	$-2.25^{+0.56}_{-0.56}$	$4.49^{+0.29}_{-0.24}$	$7.16^{+0.08}_{-0.08}$	$-2.94^{+0.22}_{-0.21}$	$3.59^{+2.07}_{-1.95}$	83.0 / 47	$1.02^{+0.04}_{-0.04}$
R1N	$7.4855^{+0.0004}_{-0.0025}$	$6.57^{+0.33}_{-0.33}$	$-2.40^{+0.81}_{-0.79}$	$4.38^{+0.44}_{-0.33}$	$6.74^{+0.10}_{-0.10}$	$-2.96^{+0.30}_{-0.30}$	$3.32^{+2.73}_{-2.49}$	77.2 / 47	$0.98^{+0.05}_{-0.05}$
R1S	$7.4750^{+0.0012}_{-0.0010}$	$7.94^{+0.37}_{-0.37}$	$-2.11^{+0.82}_{-0.81}$	$4.58^{+0.43}_{-0.31}$	$7.61^{+0.12}_{-0.12}$	$-2.83^{+0.30}_{-0.30}$	$3.84^{+3.09}_{-2.81}$	73.3 / 47	$1.04^{+0.05}_{-0.05}$
R2	$7.4770^{+0.0005}_{-0.0010}$	$6.41^{+0.21}_{-0.21}$	$-2.71^{+0.71}_{-0.70}$	$3.94^{+0.33}_{-0.24}$	$6.18^{+0.07}_{-0.07}$	$-2.71^{+0.19}_{-0.22}$	$3.01^{+1.66}_{-1.55}$	82.4 / 45	$1.04^{+0.04}_{-0.04}$
R2N	$7.4746^{+0.0027}_{-0.0014}$	$5.80^{+0.33}_{-0.32}$	$-1.68^{+0.94}_{-0.91}$	$3.80^{+0.32}_{-0.23}$	$5.76^{+0.10}_{-0.09}$	$-2.96^{+0.33}_{-0.33}$	$2.95^{+2.60}_{-2.38}$	67.9 / 47	$1.01^{+0.06}_{-0.06}$
R2S	$7.4795^{+0.0005}_{-0.0003}$	$6.81^{+0.30}_{-0.30}$	$-1.23^{+0.87}_{-0.87}$	$3.72^{+0.22}_{-0.16}$	$6.47^{+0.09}_{-0.09}$	$-2.56^{+0.28}_{-0.29}$	$3.07^{+2.18}_{-1.90}$	69.6 / 47	$1.05^{+0.05}_{-0.05}$
R3	$7.4760^{+0.0001}_{-0.0004}$	$6.81^{+0.25}_{-0.26}$	$-1.59^{+0.59}_{-0.47}$	$4.00^{+0.15}_{-0.15}$	$6.49^{+0.08}_{-0.08}$	$-2.84^{+0.14}_{-0.15}$	$3.26^{+1.00}_{-0.97}$	59.9 / 47	$1.05^{+0.04}_{-0.04}$
R3N	$7.4705^{+0.0005}_{-0.0007}$	$6.91^{+0.44}_{-0.44}$	$-3.04^{+1.22}_{-1.19}$	$4.23^{+0.77}_{-0.54}$	$6.27^{+0.12}_{-0.12}$	$-2.48^{+0.34}_{-0.34}$	$3.22^{+2.63}_{-2.33}$	71.4 / 45	$1.10^{+0.07}_{-0.07}$
R3S	$7.4788^{+0.0008}_{-0.0014}$	$6.72^{+0.34}_{-0.34}$	$-0.69^{+0.82}_{-0.78}$	$3.98^{+0.27}_{-0.19}$	$6.45^{+0.11}_{-0.11}$	$-3.01^{+0.33}_{-0.32}$	$3.30^{+2.90}_{-2.69}$	46.9 / 47	$1.04^{+0.06}_{-0.05}$
R4	$7.4776^{+0.0003}_{-0.0010}$	$5.99^{+0.38}_{-0.38}$	$-2.89^{+0.95}_{-0.93}$	$4.58^{+0.62}_{-0.47}$	$5.91^{+0.11}_{-0.11}$	$-3.54^{+0.38}_{-0.38}$	$3.12^{+3.63}_{-3.29}$	43.7 / 47	$1.01^{+0.07}_{-0.07}$
R4N	$7.4739^{+0.0017}_{-0.0016}$	$6.01^{+0.56}_{-0.55}$	$-2.06^{+1.53}_{-1.53}$	$4.09^{+0.79}_{-0.45}$	$5.51^{+0.16}_{-0.16}$	$-2.39^{+0.58}_{-0.60}$	$2.72^{+3.92}_{-3.00}$	58.7 / 47	$1.09^{+0.11}_{-0.10}$
R4S	$7.4780^{+0.0016}_{-0.0017}$	$5.87^{+0.47}_{-0.47}$	$-3.30^{+1.25}_{-1.20}$	$4.80^{+0.93}_{-0.69}$	$6.15^{+0.15}_{-0.15}$	$-4.42^{+0.52}_{-0.50}$	$3.53^{+5.95}_{-5.63}$	46.1 / 47	$0.95^{+0.08}_{-0.08}$
M	$7.4750^{+0.0004}_{-0.0016}$	$6.58^{+0.21}_{-0.22}$	$-2.04^{+0.54}_{-0.53}$	$4.18^{+0.24}_{-0.19}$	$6.31^{+0.07}_{-0.07}$	$-3.07^{+0.21}_{-0.21}$	$3.23^{+1.87}_{-1.77}$	62.1 / 47	$1.04^{+0.04}_{-0.04}$
MN	$7.4716^{+0.0007}_{-0.0014}$	$6.63^{+0.35}_{-0.35}$	$-2.90^{+0.94}_{-0.93}$	$4.35^{+0.58}_{-0.44}$	$6.18^{+0.10}_{-0.11}$	$-2.55^{+0.32}_{-0.34}$	$3.08^{+2.56}_{-2.19}$	92.1 / 47	$1.07^{+0.06}_{-0.06}$
MS	$7.4796^{+0.0002}_{-0.0008}$	$6.52^{+0.28}_{-0.28}$	$-1.60^{+0.68}_{-0.66}$	$4.10^{+0.24}_{-0.19}$	$6.37^{+0.09}_{-0.09}$	$-3.40^{+0.28}_{-0.27}$	$3.35^{+2.66}_{-2.55}$	45.9 / 47	$1.02^{+0.05}_{-0.05}$
ME	$7.4769^{+0.0009}_{-0.0006}$	$5.76^{+0.27}_{-0.27}$	$-2.34^{+0.74}_{-0.71}$	$4.04^{+0.35}_{-0.27}$	$5.54^{+0.08}_{-0.08}$	$-2.77^{+0.29}_{-0.27}$	$2.78^{+1.90}_{-1.88}$	66.6 / 47	$1.04^{+0.05}_{-0.05}$
MW	$7.4748^{+0.0003}_{-0.0009}$	$7.62^{+0.36}_{-0.36}$	$-1.54^{+0.83}_{-0.81}$	$4.30^{+0.31}_{-0.22}$	$7.35^{+0.11}_{-0.11}$	$-3.38^{+0.31}_{-0.31}$	$3.85^{+3.50}_{-3.24}$	69.0 / 47	$1.04^{+0.05}_{-0.05}$

[a] The errors indicate a 1 σ statistical uncertainly.

[b] The best-fit parameter for the (1) center energy (keV), (2, 5) Gaussian normalization (10^{-4} photons s^{-1} cm^{-2}), (3, 6) power-law index, and (4, 7) power-law normalization (10^{-11} erg s^{-1} cm^{-2}) , for the actual and simulated spectra, respectively. The parameter (8) is the ratio of the Gaussian normalization for the actual spectrum to that for the simulated spectrum.

Table 5.3: Summary of the 8–10 keV count rate for XIS 1[ab].

region	actual (count s^{-1}) (1)	simulated (count s^{-1}) (2)	ratio (3)
R1	2.38 ± 0.03	2.16 ± 0.01	1.10 ± 0.01
R1N	2.44 ± 0.04	2.22 ± 0.01	1.10 ± 0.02
R1S	1.49 ± 0.02	1.35 ± 0.01	1.10 ± 0.02
R2	2.29 ± 0.03	2.11 ± 0.01	1.08 ± 0.01
R2N	1.26 ± 0.02	1.18 ± 0.01	1.07 ± 0.02
R2S	1.64 ± 0.02	1.50 ± 0.01	1.09 ± 0.02
R3	1.67 ± 0.02	1.53 ± 0.01	1.09 ± 0.02
R3N	0.68 ± 0.01	0.63 ± 0.00	1.08 ± 0.02
R3S	1.19 ± 0.02	1.08 ± 0.01	1.10 ± 0.02
R4	0.71 ± 0.02	0.68 ± 0.00	1.05 ± 0.02
R4N	0.32 ± 0.01	0.31 ± 0.00	1.03 ± 0.04
R4S	0.48 ± 0.01	0.45 ± 0.00	1.07 ± 0.03
M	2.29 ± 0.03	2.12 ± 0.01	1.08 ± 0.01
MN	0.96 ± 0.02	0.91 ± 0.01	1.06 ± 0.02
MS	1.59 ± 0.02	1.46 ± 0.01	1.09 ± 0.02
ME	1.18 ± 0.02	1.11 ± 0.01	1.06 ± 0.02
MW	1.27 ± 0.02	1.16 ± 0.01	1.10 ± 0.02

[a] The error indicate 1 σ statistical uncertainly.

[b] (1) count rate for the actual spectra, (2) the count rate for the simulated spectra, and (3) the count rate ratio of actual to simulated spectra.

5.1.4.2 Galactic Halo (GH)

The GH is one of a celestial X-ray emission seen in any direction of the sky. The spectrum of the GH is characterized by optically-thin thermal plasma emission with a temperature of ∼0.2 keV. The flux of the GH is widely fluctuated and is depend on the angular distance from Galactic center. We evaluate these two components in the spectral fitting of the diffuse

emission local to our studying in the field.

5.1.4.3 Others of X-ray background

The contaminating emission by point-like sources is one of the important background. The sum of the point-like sources is considered as cosmic X-ray background (CXB). The bright and nearby point-like sources are low samples and have large fluctuation, while the obscure and distant sources are high samples and have small fluctuation. In this analysis, the bright sources, which are resolved by XMM-Newton, are performed spectral analysis for each sources, and the flux level of the CXB is estimated that a residual, which is subtracted the well-known level of the CXB from the sum of the estimated point-source fluxes.

5.1.4.3.1 Point-like Sources We detected point-like sources in the XIS images by visual inspection and masked a circular region around them. The radius of the masking circle was adaptively chosen for each source so that the remaining emission outside of the circle is smaller than the ambient emission. The masked regions are dashed circle (figure 5.6).

The XMM-Newton data were available in most of the XIS field of Fornax A (figure 5.6). We could thus consider point-like sources unresolved with Suzaku but resolved with XMM-Newton. We employed the XMM-Newton source list in the pipeline products with a detection significance above 5σ (table 5.4). For each individual source, we performed spectral fitting to characterize its spectrum. We accumulated source and background events from a circular region with a radius of $36''$ and an annulus region with inner and outer radii of 72–$180''$ respectively. Because of the small aperture and the local background subtraction, the spectra contains negligible contributions from diffuse background emission. The RMF and ARF were generated using the `rmfgen` and `arfgen` tools. We used all the three EPIC sensors whenever available.

We fitted the background-subtracted spectra in the 0.5–6 keV with a power-law model attenuated by an interstellar photo-electric absorption model (`wabs`; Morrison & McCammon 1983). The absorption column density was fixed to 2.06×10^{20} cm^{-2}, which is the Galactic value toward Fornax A. Most sources were successfully fitted with a simple power-law model. We then simulated an XIS event file using the ray-tracing tool, `xissim`, by feeding the list of XMM-Newton source position and the best-fit parameters. The simulated event file was used for extracting spectra of unresolved point-like sources. The spectra were characterized

by the spectral model composed of two power-law components with different indices and normalizations attenuated by the Galactic absorption. The best-fit parameters and spectra for each source are shown in table 5.4 and figure 5.8.

The uncertainty in simulating the unresolved point-like source spectra was evaluated as follows. Using the mean and standard deviation for each fitting parameter for each individual source, we randomly chose a value for a parameter following the Gaussian probability density function of the mean and the standard deviation. We then simulated an XIS event list using the ray-tracing simulator by feeding the list of the source position and the altered spectral parameters. The extracted spectra of unresolved point-like sources were fitted with the attenuated two power-law component model. This procedure was repeated 100 times with different random choices of parameter values, producing the histograms of the best-fit normalization and power-law index values for the spectra of unresolved point-like sources. Figure 5.13 shows the histogram, which was fitted with a Gaussian model. The Gaussian center and the sigma were 0.31×10^{-11} erg s^{-1} cm^{-2} and 0.16×10^{-11} erg s^{-1} cm^{-2}, respectively. The standard deviation of the Gaussian was taken as the uncertainty in evaluating the spectral intensity and shape of unresolved point-like sources.

Table 5.4: XMM-Newton point source list[a].

No.	Position J2000.0		Counts [b]	Γ	$F_{0.5-6\mathrm{keV}}$ [c]	χ^2/dof
	R. A	Decl.			(10^{-14} erg s^{-1} cm^{-2})	
1	$03^h23^m07^s.342$	$-36°53'00''93$	4503	$2.08\ ^{+0.03}_{-0.03}$	$44.96\ ^{+0.69}_{-0.69}$	136.0/137
2	$03^h22^m41^s.038$	$-37°04'47''18$	1128	$1.40\ ^{+0.08}_{-0.08}$	$15.41\ ^{+0.89}_{-0.88}$	47.9/53
3	$03^h23^m55^s.190$	$-37°08'42''17$	744	$2.03\ ^{+0.13}_{-0.13}$	$8.47\ ^{+0.68}_{-0.67}$	51.2/39
4	$03^h23^m40^s.172$	$-36°53'59''72$	505	$2.26\ ^{+0.21}_{-0.19}$	$3.49\ ^{+0.38}_{-0.36}$	37.5/31
5	$03^h22^m35^s.420$	$-37°08'09''54$	571	$2.24\ ^{+0.22}_{-0.21}$	$5.15\ ^{+0.66}_{-0.62}$	15.7/26
6	$03^h23^m43^s.959$	$-36°57'54''15$	492	$2.44\ ^{+0.29}_{-0.26}$	$2.27\ ^{+0.33}_{-0.31}$	22.0/30
7	$03^h23^m41^s.508$	$-36°56'46''29$	802	2.07	2.60	54.2/27
8	$03^h22^m41^s.050$	$-37°00'57''83$	533	$2.12\ ^{+0.26}_{-0.24}$	$3.03\ ^{+0.46}_{-0.43}$	16.3/24
9	$03^h23^m23^s.996$	$-36°49'53''46$	482	3.06	2.18	101.7/25
10	$03^h23^m32^s.191$	$-37°04'16''68$	640	$1.64\ ^{+0.30}_{-0.28}$	$2.12\ ^{+0.44}_{-0.41}$	33.8/29
11	$03^h22^m54^s.121$	$-37°12'34''12$	484	2.36	4.65	79.8/23
12	$03^h24^m09^s.731$	$-37°06'21''93$	431	$2.32\ ^{+0.36}_{-0.32}$	$2.42\ ^{+0.48}_{-0.44}$	21.4/23
13	$03^h23^m25^s.259$	$-36°47'34''35$	920	$1.55\ ^{+0.13}_{-0.13}$	$7.26\ ^{+0.64}_{-0.63}$	20.9/17
14	$03^h22^m55^s.021$	$-36°51'43''33$	180	$2.13\ ^{+0.33}_{-0.29}$	$2.11\ ^{+0.43}_{-0.39}$	4.6/8

15	$03^h22^m29^s.502$	$-37°00'20''15$	366	$2.43\ ^{+0.46}_{-0.39}$	$1.82\ ^{+0.45}_{-0.39}$	12.8/18
16	$03^h23^m57^s.618$	$-37°11'07''72$	384	$2.29\ ^{+0.60}_{-0.49}$	$2.09\ ^{+0.64}_{-0.53}$	22.2/19
17	$03^h23^m42^s.239$	$-36°59'25''50$	521	$2.21\ ^{+0.69}_{-0.54}$	$0.88\ ^{+0.32}_{-0.27}$	23.6/25
19	$03^h24^m03^s.296$	$-36°56'09''88$	481	$1.62\ ^{+0.27}_{-0.25}$	$2.63\ ^{+0.49}_{-0.46}$	25.1/25
20	$03^h23^m16^s.085$	$-36°48'21''18$	373	$2.03\ ^{+0.96}_{-0.71}$	$1.21\ ^{+0.64}_{-0.51}$	27.6/18
21	$03^h23^m32^s.946$	$-36°53'52''38$	350	$1.85\ ^{+0.37}_{-0.34}$	$1.84\ ^{+0.44}_{-0.40}$	15.7/21
22	$03^h23^m22^s.317$	$-37°12'20''41$	394	$1.67\ ^{+0.34}_{-0.31}$	$3.30\ ^{+0.74}_{-0.68}$	23.9/19
23	$03^h22^m59^s.307$	$-36°53'52''63$	484	$1.86\ ^{+0.26}_{-0.24}$	$1.86\ ^{+0.33}_{-0.31}$	9.8/15
24	$03^h24^m20^s.097$	$-36°58'38''34$	540	$3.09\ ^{+0.43}_{-0.38}$	$2.15\ ^{+0.36}_{-0.34}$	20.2/24
25	$03^h23^m17^s.120$	$-36°54'26''54$	445	$1.68\ ^{+0.57}_{-0.50}$	$1.26\ ^{+0.44}_{-0.39}$	29.0/20
26	$03^h23^m37^s.750$	$-37°01'11''62$	525	$1.31\ ^{+0.34}_{-0.33}$	$1.40\ ^{+0.37}_{-0.35}$	29.2/26
27	$03^h23^m06^s.487$	$-37°08'25''77$	297	$2.22\ ^{-2.22}_{-2.22}$	$0.13\ ^{+0.38}_{-0.13}$	12.9/13
28	$03^h23^m22^s.432$	$-36°53'39''70$	518	$1.86\ ^{+0.48}_{-0.42}$	$1.27\ ^{+0.39}_{-0.36}$	21.6/22
29	$03^h22^m53^s.065$	$-37°04'36''83$	391	$2.28\ ^{+0.75}_{-0.58}$	$0.98\ ^{+0.39}_{-0.31}$	21.0/19
30	$03^h23^m16^s.094$	$-36°58'55''06$	507	$2.25\ ^{+0.80}_{-0.62}$	$0.51\ ^{+0.26}_{-0.11}$	30.3/23
31	$03^h22^m59^s.063$	$-37°00'44''64$	325	$1.77\ ^{+0.64}_{-0.54}$	$1.32\ ^{+0.50}_{-0.44}$	30.3/22
32	$03^h23^m26^s.225$	$-37°12'31''99$	412	$0.90\ ^{+0.29}_{-0.28}$	$4.95\ ^{+1.07}_{-1.02}$	26.7/19
33	$03^h23^m32^s.816$	$-36°57'26''51$	533	$1.62\ ^{+0.51}_{-0.44}$	$1.43\ ^{+0.40}_{-0.37}$	35.1/27
34	$03^h22^m56^s.391$	$-36°58'49''22$	306	$2.25\ ^{+1.33}_{-0.79}$	$0.80\ ^{+0.43}_{-0.33}$	16.0/13
35	$03^h24^m14^s.173$	$-37°02'53''40$	410	$2.68\ ^{+0.52}_{-0.45}$	$1.57\ ^{+0.39}_{-0.34}$	31.0/18
36	$03^h22^m30^s.276$	$-37°11'26''08$	299	$2.02\ ^{+0.50}_{-0.42}$	$2.46\ ^{+0.82}_{-0.67}$	0.3/4
37	$03^h23^m22^s.191$	$-36°49'09''01$	377	$1.87\ ^{+0.42}_{-0.36}$	$1.80\ ^{+0.51}_{-0.46}$	21.9/19
38	$03^h23^m16^s.935$	$-37°06'12''17$	376	$1.97\ ^{+0.85}_{-0.65}$	$0.71\ ^{+0.37}_{-0.30}$	14.3/19
39	$03^h23^m23^s.412$	$-36°52'06''98$	263	$1.25\ ^{+0.49}_{-0.47}$	$1.65\ ^{+0.56}_{-0.51}$	21.9/15
40	$03^h22^m44^s.806$	$-37°00'26''76$	392	$1.54\ ^{+0.57}_{-0.51}$	$1.17\ ^{+0.44}_{-0.36}$	5.0/10
41	$03^h23^m25^s.190$	$-36°57'44''81$	271	$1.76\ ^{+0.45}_{-0.40}$	$1.39\ ^{+0.39}_{-0.36}$	15.0/20
42	$03^h22^m49^s.417$	$-37°12'42''80$	342	$1.44\ ^{+0.50}_{-0.44}$	$2.36\ ^{+0.93}_{-0.82}$	21.9/16
43	$03^h24^m00^s.944$	$-37°08'34''27$	414	$2.07\ ^{+0.71}_{-0.55}$	$1.32\ ^{+0.56}_{-0.47}$	23.1/18
44	$03^h23^m28^s.533$	$-37°10'10''64$	240	$1.38\ ^{+0.54}_{-0.47}$	$1.94\ ^{+0.70}_{-0.64}$	27.8/15
45	$03^h24^m05^s.380$	$-37°07'10''72$	350	$2.12\ ^{+0.49}_{-0.44}$	$1.74\ ^{+0.50}_{-0.44}$	21.7/20
46	$03^h23^m34^s.628$	$-36°56'53''12$	489	$4.56\ ^{+0.67}_{-0.57}$	$0.92\ ^{+0.15}_{-0.15}$	35.9/25
47	$03^h23^m27^s.295$	$-37°03'13''63$	496	2.00	0.00	104.6/22
48	$03^h24^m21^s.792$	$-37°07'17''74$	433	3.31	0.86	182.8/21
49	$03^h24^m05^s.661$	$-36°59'18''32$	266	$0.42\ ^{+0.87}_{-1.09}$	$1.53\ ^{+0.74}_{-0.66}$	16.1/16
50	$03^h23^m11^s.317$	$-37°10'54''91$	241	$2.64\ ^{+1.77}_{-1.03}$	$0.68\ ^{+0.51}_{-0.34}$	14.0/12

51	$03^h23^m08^s.057$	$-37°03'04''78$	410	$1.32\ ^{+0.67}_{-0.62}$	$0.85\ ^{+0.40}_{-0.35}$	15.4/21
52	$03^h23^m12^s.232$	$-37°16'38''08$	324	$1.38\ ^{+0.38}_{-0.35}$	$2.93\ ^{+0.95}_{-0.85}$	6.4/5
53	$03^h23^m08^s.656$	$-37°14'11''11$	290	$2.04\ ^{+1.23}_{-0.71}$	$1.21\ ^{+0.70}_{-0.53}$	4.7/9
54	$03^h22^m39^s.036$	$-37°08'05''58$	355	$1.85\ ^{+0.51}_{-0.43}$	$2.06\ ^{+0.68}_{-0.59}$	12.3/17
55	$03^h23^m00^s.135$	$-36°48'47''50$	275	2.00	0.00	58.7/8
57	$03^h23^m16^s.649$	$-37°09'45''89$	350	$1.20\ ^{+1.26}_{-1.00}$	$1.01\ ^{+0.72}_{-0.60}$	22.7/15
58	$03^h23^m54^s.478$	$-37°13'13''88$	259	3.42	0.12	86.8/10
59	$03^h23^m22^s.332$	$-36°56'07''48$	395	$3.48\ ^{+1.72}_{-1.14}$	$0.29\ ^{+0.17}_{-0.15}$	20.7/20
60	$03^h24^m16^s.254$	$-36°53'55''53$	599	$2.31\ ^{+0.52}_{-0.45}$	$1.39\ ^{+0.38}_{-0.34}$	9.9/10
62	$03^h23^m10^s.290$	$-36°58'38''51$	460	$9.98\ ^{-38.65}_{-41.65}$	0.17	30.2/20
63	$03^h24^m03^s.238$	$-36°59'50''22$	393	$1.29\ ^{+1.39}_{-0.96}$	$0.68\ ^{+0.50}_{-0.43}$	23.8/18
64	$03^h23^m28^s.236$	$-37°01'12''52$	205	$1.32\ ^{+0.76}_{-0.69}$	$0.75\ ^{+0.41}_{-0.36}$	19.8/16
65	$03^h23^m10^s.027$	$-37°09'15''69$	330	$1.25\ ^{+1.04}_{-0.84}$	$0.96\ ^{+0.63}_{-0.54}$	16.2/16
66	$03^h23^m56^s.198$	$-36°58'56''38$	347	$7.18\ ^{-7.18}_{-3.57}$	$0.25\ ^{+0.12}_{-0.11}$	15.0/13
67	$03^h23^m31^s.427$	$-37°13'00''17$	289	$0.44\ ^{+0.57}_{-0.65}$	$2.54\ ^{+0.99}_{-0.95}$	14.2/15
68	$03^h22^m37^s.989$	$-37°08'56''29$	312	$1.89\ ^{+0.92}_{-0.67}$	$1.15\ ^{+0.67}_{-0.52}$	8.2/14
69	$03^h24^m29^s.887$	$-37°02'11''62$	603	$2.49\ ^{+0.78}_{-0.69}$	$1.83\ ^{+0.65}_{-0.56}$	19.8/25
70	$03^h23^m38^s.321$	$-36°57'55''77$	416	$3.04\ ^{+0.79}_{-0.67}$	$0.76\ ^{+0.26}_{-0.23}$	36.4/22
71	$03^h22^m41^s.652$	$-37°00'15''63$	404	$1.56\ ^{+0.42}_{-0.36}$	$1.60\ ^{+0.42}_{-0.38}$	11.6/12
73	$03^h22^m49^s.453$	$-37°10'26''78$	250	$0.45\ ^{-0.45}_{-0.45}$	$0.36\ ^{+0.92}_{-0.36}$	13.3/12
74	$03^h23^m19^s.519$	$-36°53'34''00$	450	$0.58\ ^{+0.91}_{-1.13}$	$1.19\ ^{+0.73}_{-0.64}$	21.5/15
75	$03^h22^m25^s.273$	$-36°52'27''27$	213	$2.95\ ^{+1.04}_{-0.73}$	$1.47\ ^{+0.53}_{-0.44}$	0.2/2
77	$03^h24^m11^s.771$	$-36°55'14''77$	343	$1.44\ ^{+4.43}_{-1.71}$	$0.48\ ^{+0.57}_{-0.48}$	12.5/16
78	$03^h24^m15^s.522$	$-36°58'48''37$	502	$4.10\ ^{+0.64}_{-0.53}$	$1.28\ ^{+0.26}_{-0.25}$	41.1/21
81	$03^h23^m48^s.964$	$-36°57'14''36$	354	$4.04\ ^{+2.01}_{-1.25}$	$0.36\ ^{+0.16}_{-0.15}$	15.1/18
82	$03^h22^m59^s.357$	$-37°07'32''36$	163	$2.00\ ^{-2.00}_{-2.00}$	$0.00\ ^{+0.39}_{0.00}$	6.9/11
86	$03^h23^m02^s.165$	$-37°05'22''04$	228	$-0.83\ ^{+1.49}_{+0.67}$	$0.98\ ^{+0.93}_{-0.82}$	15.8/10
89	$03^h23^m01^s.510$	$-36°57'53''71$	442	$1.84\ ^{+0.81}_{-0.63}$	$0.54\ ^{+0.31}_{-0.26}$	17.1/17
91	$03^h22^m49^s.716$	$-36°59'37''79$	325	$0.75\ ^{+0.42}_{-0.44}$	$1.07\ ^{+0.34}_{-0.33}$	11.6/9
94	$03^h23^m45^s.726$	$-37°14'37''51$	274	2.00	0.00	10.8/3
95	$03^h23^m59^s.253$	$-36°53'37''99$	244	$-2.98\ ^{+29.10}_{-29.10}$	$0.62\ ^{+0.77}_{-0.62}$	14.0/12
96	$03^h23^m16^s.983$	$-37°00'14''50$	480	$-0.04\ ^{+1.12}_{-2.33}$	$0.58\ ^{+0.40}_{-0.39}$	24.3/24
97	$03^h23^m21^s.712$	$-36°54'31''87$	397	$3.97\ ^{+1.19}_{-0.87}$	$0.54\ ^{+0.17}_{-0.16}$	17.9/20
101	$03^h23^m12^s.051$	$-37°00'54''06$	315	$1.80\ ^{-1.80}_{-1.80}$	$0.19\ ^{+0.34}_{-0.19}$	26.4/19
102	$03^h22^m57^s.645$	$-36°55'32''83$	397	$3.50\ ^{+0.98}_{-0.78}$	$0.55\ ^{+0.15}_{-0.12}$	16.2/11

104	$03^h23^m04^s.296$	$-37°02'42''89$	428	$2.86\ ^{+5.72}_{-1.88}$	$0.17\ ^{+0.23}_{-0.16}$	25.9/20
107	$03^h23^m56^s.630$	$-37°04'32''67$	319	$-0.40\ ^{+1.31}_{0.38}$	$0.91\ ^{+0.70}_{-0.65}$	18.8/17
109	$03^h22^m47^s.109$	$-36°52'53''76$	339	$-1.65\ ^{+1.96}_{1.65}$	$1.26\ ^{+0.90}_{-0.75}$	6.2/9
116	$03^h23^m11^s.322$	$-37°00'20''72$	442	$2.60\ ^{+1.32}_{-0.92}$	$0.37\ ^{+0.24}_{-0.18}$	28.9/22
122	$03^h22^m11^s.258$	$-36°59'14''88$	264	2.00	0.00	17.1/3
123	$03^h23^m44^s.820$	$-36°56'08''86$	377	$0.91\ ^{+1.07}_{-1.16}$	$1.29\ ^{+0.70}_{-0.63}$	15.7/16
129	$03^h22^m09^s.884$	$-37°01'28''46$	266	0.38	1.68	7.4/3
151	$03^h23^m43^s.364$	$-37°05'26''06$	385	$2.00\ ^{-2.00}_{-2.00}$	$0.00\ ^{+0.32}_{0.00}$	22.1/17

[a] The errors indicate a 90% statistical uncertainty.

[b] Background-unsubtracted counts in the 0.5–6 keV range. The counts record by PN are shown except for sources No. 13 and 60 (MOS 1 + MOS 2) and 75 (MOS 2).

[c] Absorption-uncorrected flux in the 0.5–6 keV range.

Then we accumulated the simulated point-like source spectra for each observation field of view to reproduce the summed point source spectra in the 0.5–5.5 keV with double power-law model attenuated by an interstellar photo-electric absorption model (`wabs`; Morrison & McCammon 1983). The absorption column was fixed to 2.06×10^{20} cm^{-2}, again. The double power-law succeeded to describe the point source spectra and the best-fit parameter and spectra are shown in table 5.5 and figure 5.14.

5.1.4.3.2 CXB In general, CXB flux is determined by measuring the sum of the *unresolved* X-ray emission. Since we independently evaluated the contaminant point-like source flux using the XMM-Newton data, it is expected that we will overestimated the CXB if we employ the CXB estimated by Suzaku directly. In order to estimate the CXB correctly, we carefully compared the level of the sum flux of the resolved point-like sources with well know $\log N$-$\log S$ relation. Figure 5.15 shows the $\log N$-$\log S$ in the 2–10 keV band from the Chandra deep field south (Rosati et al. 2002) (black) and that derived from our point-like sources results (red). Our point-source results is consistent with that of the Chandra deep field south in the range of $S = 10^{-14}$–10^{-13} erg s^{-1}cm^{-2}. On the other hand, in the range of $S < 10^{-14}$ erg s^{-1} cm^{-2}, the N of our point-like sources saturated because of the limit of spatial resolution of XMM-Newton. Thus we consider the CXB level, after subtracting XMM-Newton detected point sources, is safely estimated as follows. We estimated that the CXB flux is the residual, which is subtracted the sum of the our analyzed point-like source (2.61×10^{-8} erg s^{-1} cm^{-2} str^{-1}) of the from the total flux level of the Chandra deep field (5.15×10^{-8} erg s^{-1} cm^{-2} str^{-1} Rosati et al. 2002). Thus we estimate the CXB level as the

Table 5.5: Best-fit parameters for point-like sources[ab].

Region	Γ_1 (1)	F_1 (2)	Γ_2 (3)	F_2 (4)	χ^2/dof
R1	$2.28^{+0.35}_{-0.18}$	$1.26^{+0.50}_{-0.67}$	$0.39^{+0.62}_{-0.83}$	$2.61^{+0.38}_{-0.37}$	101.1 / 75
R1N	$4.96^{-4.99}_{-4.99}$	$0.00^{+0.10}_{-0.00}$	$2.01^{+0.44}_{-2.02}$	$0.15^{+1.19}_{-0.04}$	19.2 / 13
R1S	$2.25^{+0.41}_{-0.21}$	$2.46^{+1.22}_{-1.48}$	$0.48^{+0.62}_{-0.96}$	$5.23^{+0.91}_{-0.90}$	59.7 / 33
R2	$1.97^{+0.15}_{-0.09}$	$2.35^{+0.36}_{-0.64}$	$-0.29^{+0.86}_{-1.05}$	$2.44^{+0.80}_{-0.49}$	142.4 / 95
R2N	$1.89^{+0.27}_{-0.08}$	$3.07^{+0.43}_{-1.25}$	$-1.54^{+2.26}_{1.54}$	$3.34^{+2.61}_{-1.69}$	18.4 / 17
R2S	$2.30^{+0.36}_{-0.26}$	$1.39^{+0.74}_{-0.68}$	$0.15^{+0.63}_{-1.21}$	$3.60^{+0.97}_{-0.57}$	41.8 / 21
R3	$3.02^{+0.36}_{-0.42}$	$0.54^{+0.79}_{-0.29}$	$1.31^{+0.19}_{-0.47}$	$4.39^{+0.24}_{-0.53}$	138.2 / 102
R3N	$3.21^{+0.71}_{-0.53}$	$0.62^{+1.47}_{-0.50}$	$1.72^{+0.26}_{-0.69}$	$4.53^{+0.43}_{-1.18}$	90.3 / 60
R3S	$3.11^{+1.57}_{-2.37}$	$0.20^{+1.99}_{-0.14}$	$1.30^{+0.21}_{-0.71}$	$4.32^{+0.33}_{-1.13}$	31.2 / 17
R4	$3.49^{+0.49}_{-0.30}$	$0.45^{+0.36}_{-0.27}$	$1.36^{+0.22}_{-0.22}$	$6.39^{+0.40}_{-0.39}$	97.0 / 62
R4S	$2.78^{+0.35}_{-0.21}$	$2.93^{+1.18}_{-1.39}$	$0.27^{+0.77}_{-1.07}$	$11.59^{+6.52}_{-2.49}$	18.9 / 16
R4N	$5.60^{+1.33}_{-0.95}$	$0.01^{+0.02}_{-0.01}$	$1.55^{+0.13}_{-0.09}$	$4.02^{+0.37}_{-0.38}$	73.8 / 45
M	$3.15^{+0.29}_{-0.24}$	$0.53^{+0.35}_{-0.24}$	$1.34^{+0.15}_{-0.20}$	$4.93^{+0.21}_{-0.26}$	223.7 / 165
MN	$2.93^{+0.42}_{-0.18}$	$1.56^{+0.70}_{-0.91}$	$1.19^{+0.38}_{-0.34}$	$5.71^{+0.65}_{-0.55}$	77.9 / 50
MS	$4.05^{+0.71}_{-0.63}$	$0.05^{+0.11}_{-0.04}$	$1.39^{+0.10}_{-0.15}$	$4.46^{+0.23}_{-0.22}$	45.1 / 28
ME	$2.69^{+0.32}_{-0.20}$	$1.23^{+0.58}_{-0.61}$	$0.92^{+0.41}_{-0.52}$	$3.70^{+0.41}_{-0.41}$	125.9 / 82
MW	$3.36^{+0.38}_{-0.33}$	$0.42^{+0.65}_{-0.22}$	$1.33^{+0.16}_{-0.22}$	$6.21^{+0.31}_{-0.32}$	149.6 / 83

[a] The errors indicate a 1 σ statistical uncertainly.

[b] The best-fit parameter for the power-law index (1 and 3) and normalization in the 2–10 keV band (2 and 4) for the two power-law components.

field of Fornax A is 2.54×10^{-8} erg s^{-1} cm^{-2} str^{-1}.

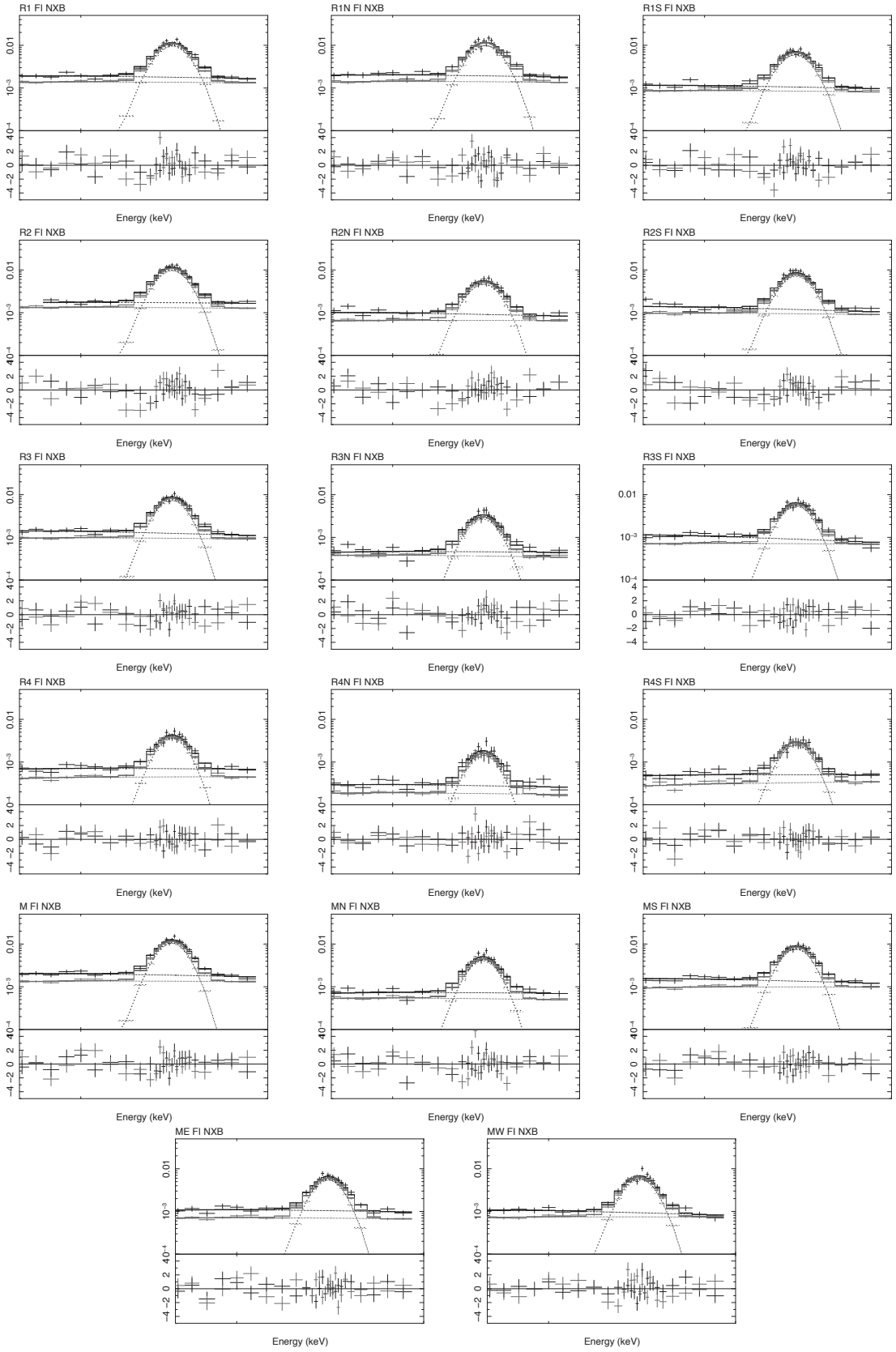

Figure 5.7: Actual (black) and simulated (red) NXB spectra around the Ni Kα line for each observation and each region. The doted curves indicate the best-fit model.

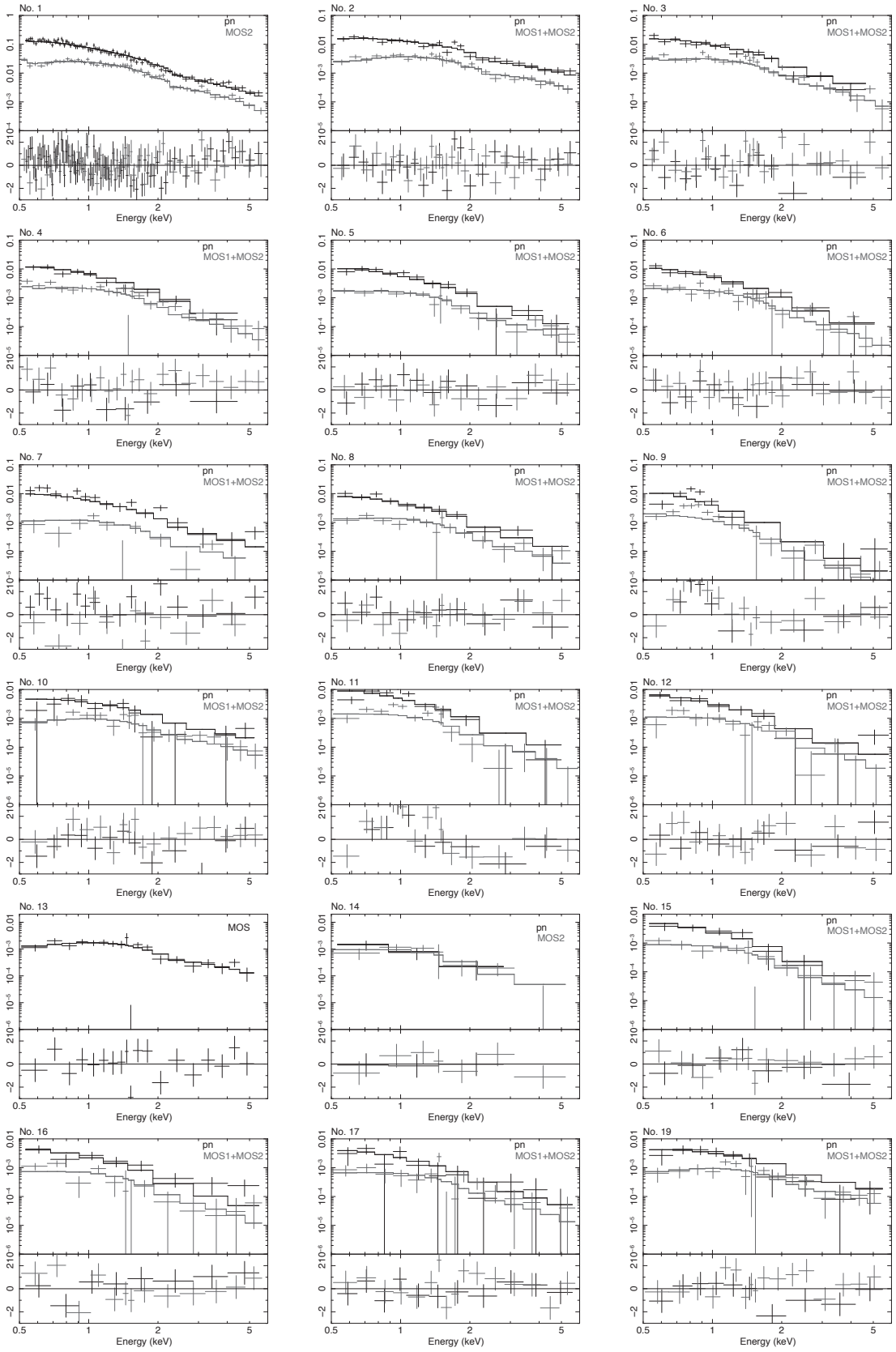

Figure 5.8: XMM-Newton Spectra and best-fit models of individual sources.

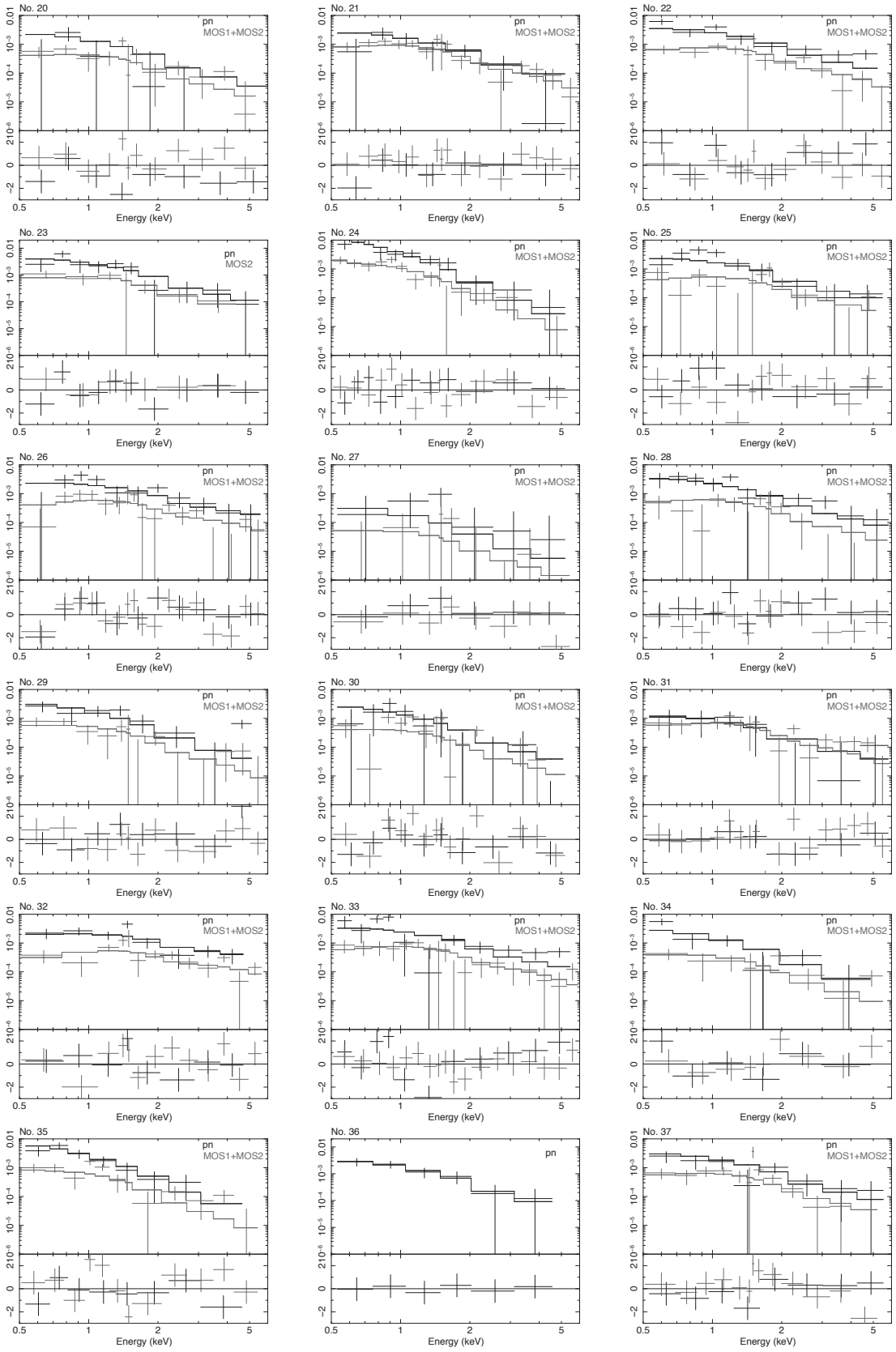

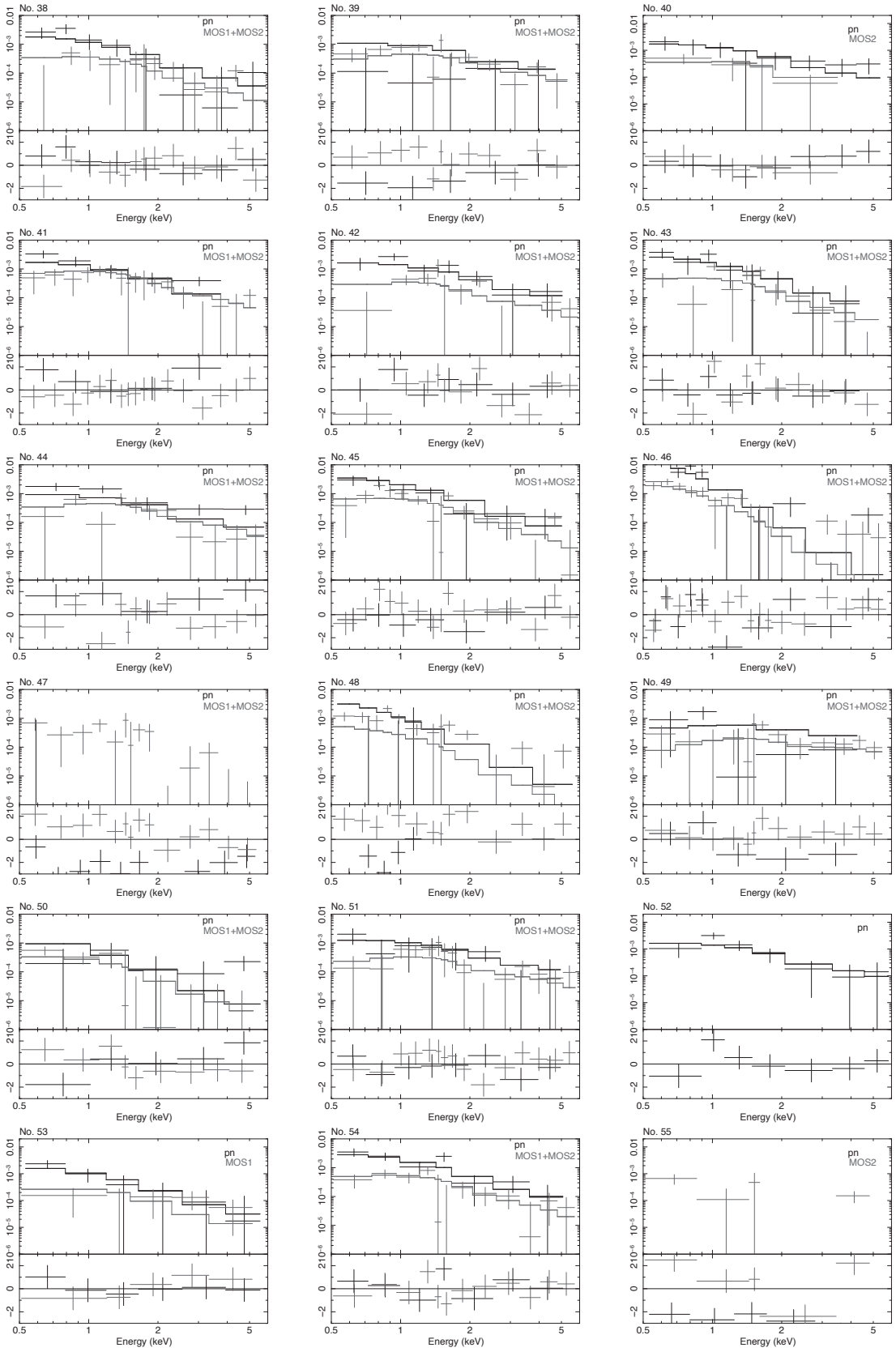

Figure 5.9: Continued.

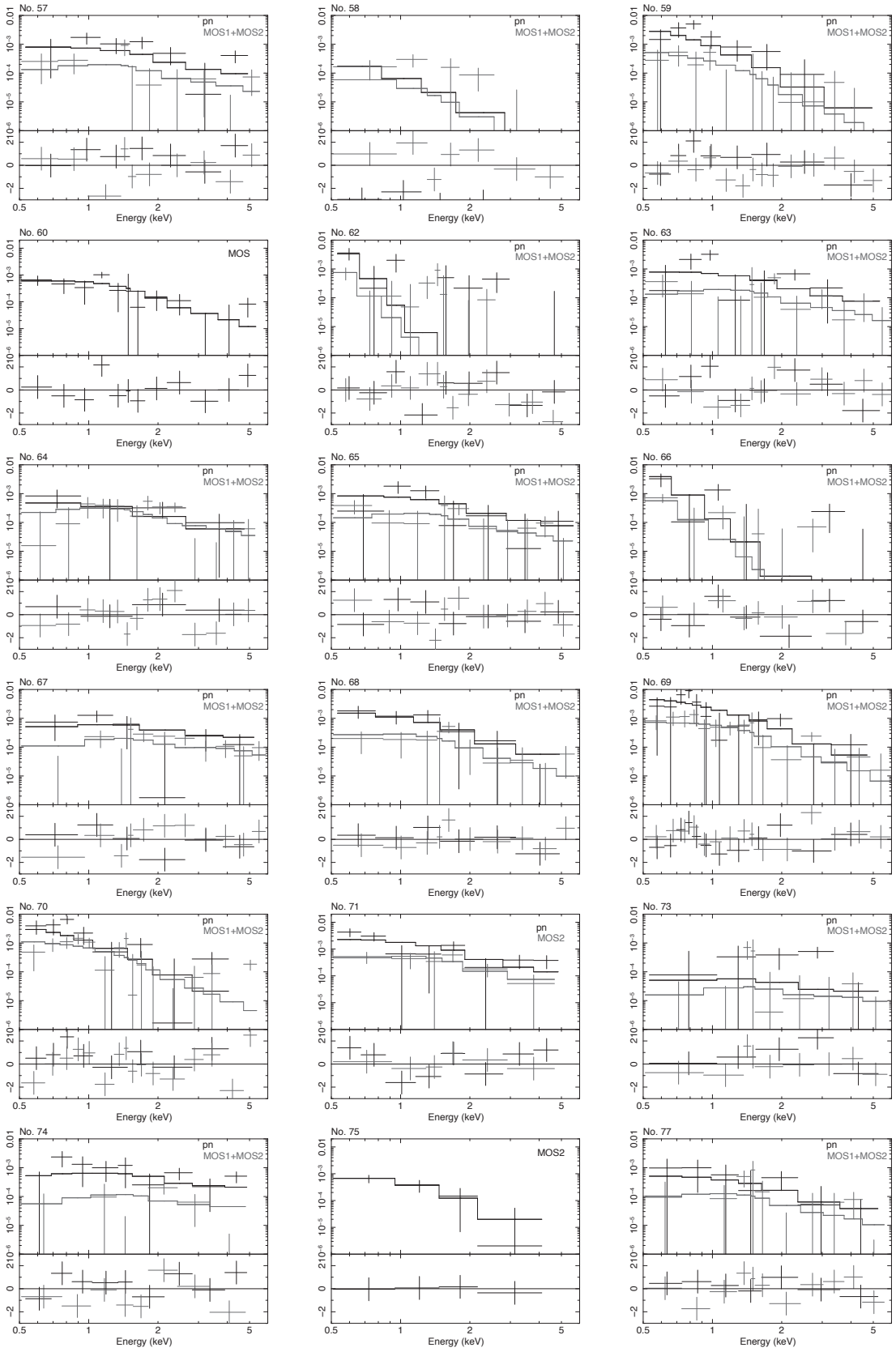

Figure 5.10: Continued.

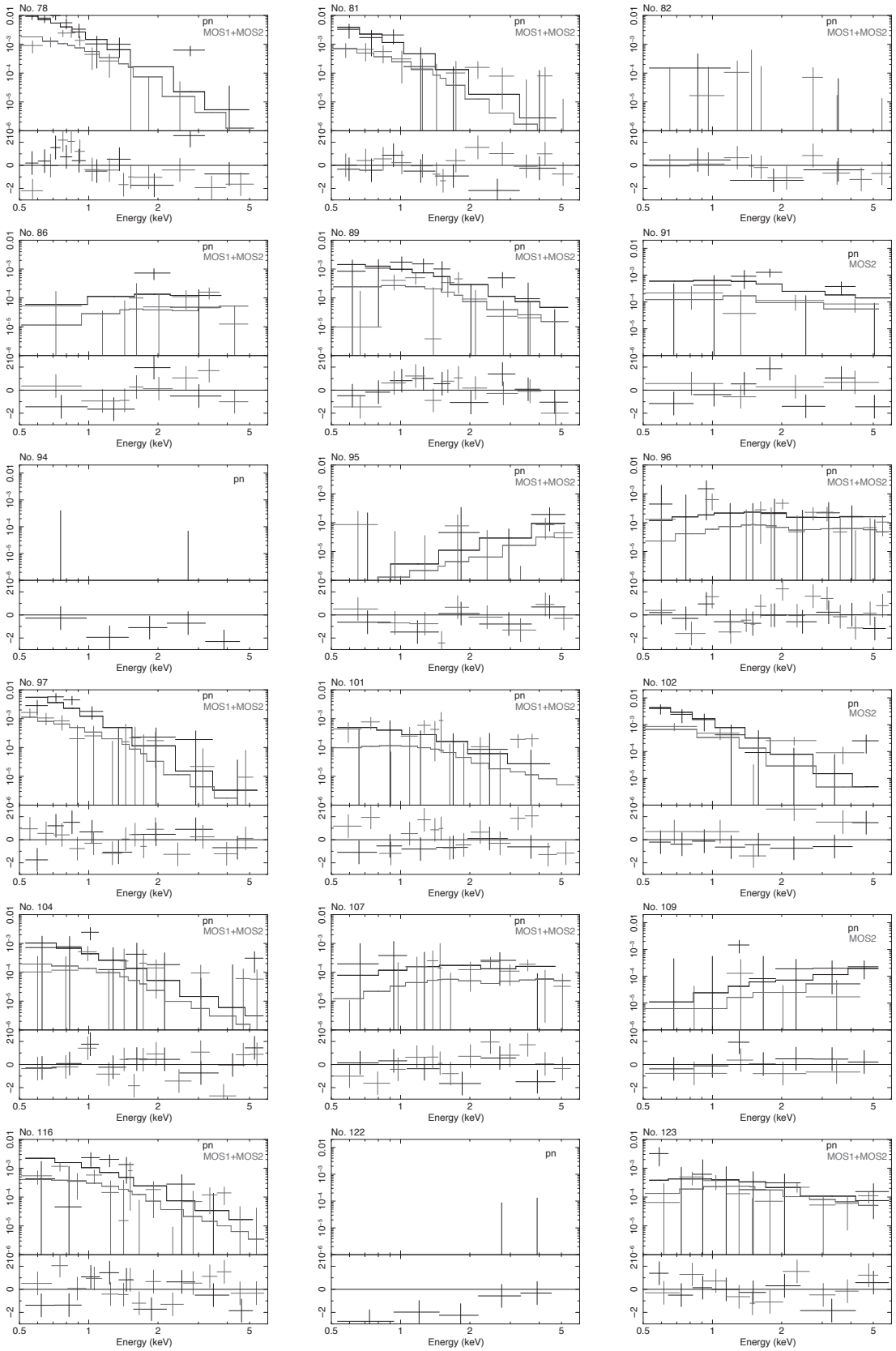

Figure 5.11: Continued.

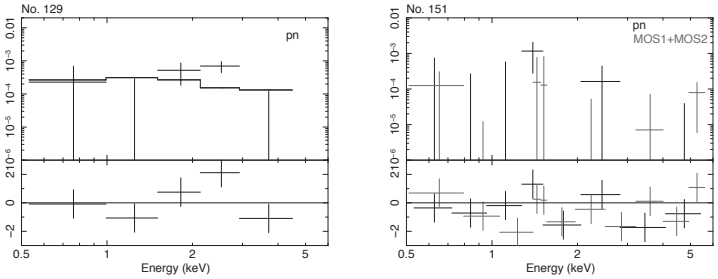

Figure 5.12: Continued.

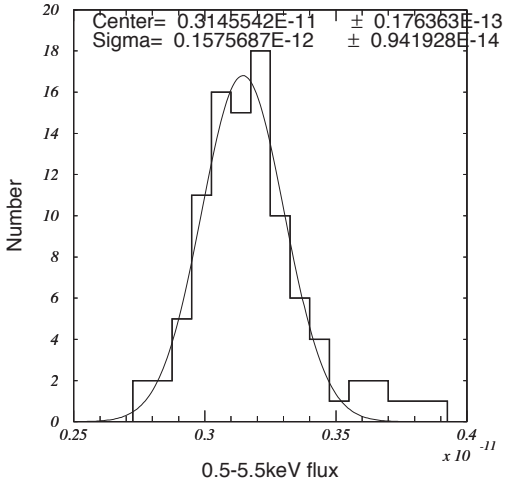

Figure 5.13: Histogram of the 0.5–5.5 keV flux of contaminating sources. The curve shows best-fit Gaussian model.

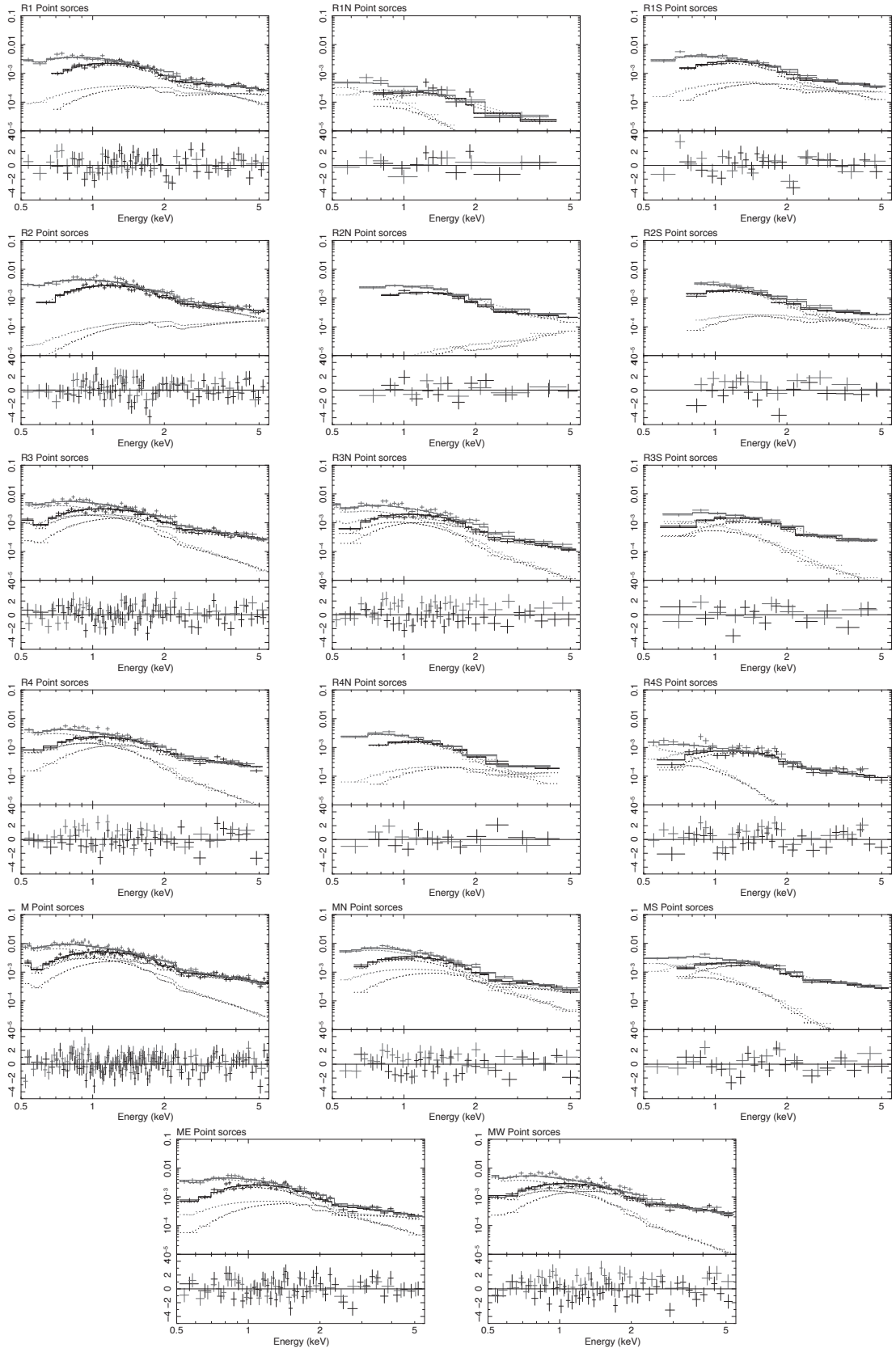

Figure 5.14: Composite spectra of point sources and the best-fit models. Best-fit point-like source spectra for each region. The black and red are FI and BI, respectively. The dotted curves represent the model.

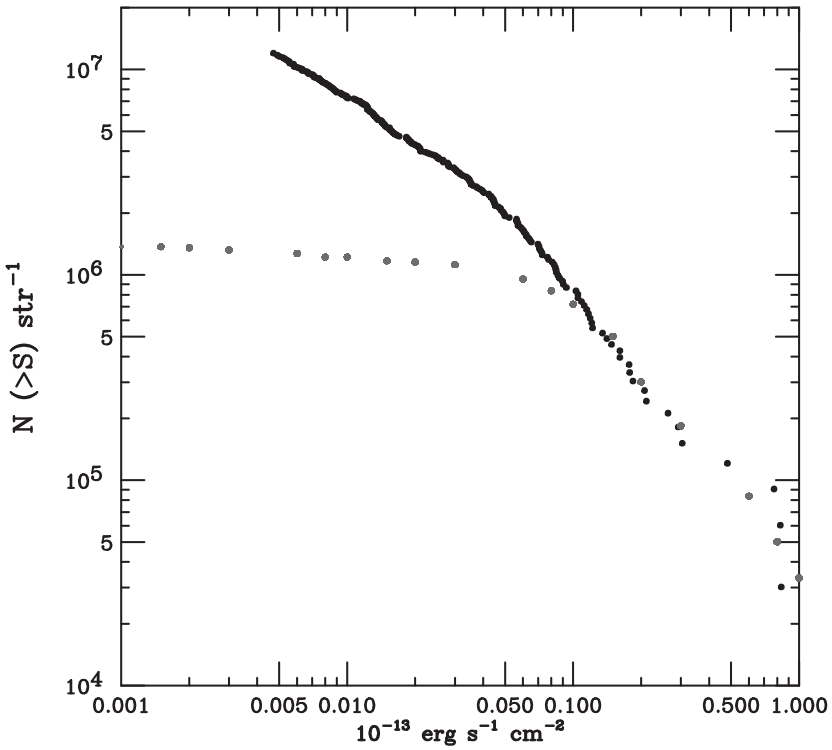

Figure 5.15: log$N$-log$S$ in the 2–10 keV band for the Chandra deep field south (Rosati et al. 2002) (black) and our point-like sources results (red).

5.1.5 X-ray Spectra (2) Source Emission of Individual Components

5.1.5.1 Cluster Component

In order to constrain the cluster component at the position of Fornax A, which is displaced from the cluster center by 3.6°, we retrieved XIS archive data taken in the Fornax cluster at various distances from the cluster center. We employed three data sets (table 5.6) that are devoid of bright point-like sources in the field of view. All the data were taken with the normal clocking mode.

Table 5.6: Suzaku data sets in the Fornax cluster.

Sequence ID	Position (J2000.0)		Observation	Dist.[a]	$t_{\rm exp}$[b]
	R. A.	DEC	start date	(arcdeg)	(ks)[b]
702002010	03h36m39.1s	-35°57′12″	2007-07-28	0.65	51.7
703038010	03h31m06.3s	-38°24′05″	2008-06-16	3.30	24.3
802040010	03h19m57.4s	-32°03′58″	2007-06-29	5.13	19.7

[a] The distance from the center of the Fornax cluster at (R. A., Decl.)=(03h38m30.9s, -35°27′16″).

[b] The mean exposure time of the three XIS sensors.

Figure 5.16 shows the positions of the field near the Fornax cluster. We first identified point-like sources in the XIS images with a visual inspection and masked them. We used the remaining regions to extract the source spectra. We fitted the NXB-subtracted spectra with a model consisting of three spectral components: two are the Galactic halo and the CXB components for the XDB emission and the other is thermal emission of the Fornax cluster.

For the Galactic halo component, we used the `mekal` model (Mewe et al. 1985, 1986; Kaastra 1992; Liedahl et al. 1995) with the plasma temperature ($kT^{\rm (GH)}$) and the surface brightness ($S^{\rm (GH)}$) as free parameters and the metal abundance fixed to that of solar (Anders & Grevesse 1989). For the CXB component, we used the power-law model with the surface brightness ($S^{\rm (CXB)}$) as a free parameter and the power-law index fixed to –1.4 . For the cluster component, we used the `mekal` model with free parameters of the plasma temperature ($kT^{\rm (FC)}$) and the surface brightness ($S^{\rm (FC)}$) and a fixed metal abundance in the same manner as the XDB emission component. All the components were attenuated by an interstellar

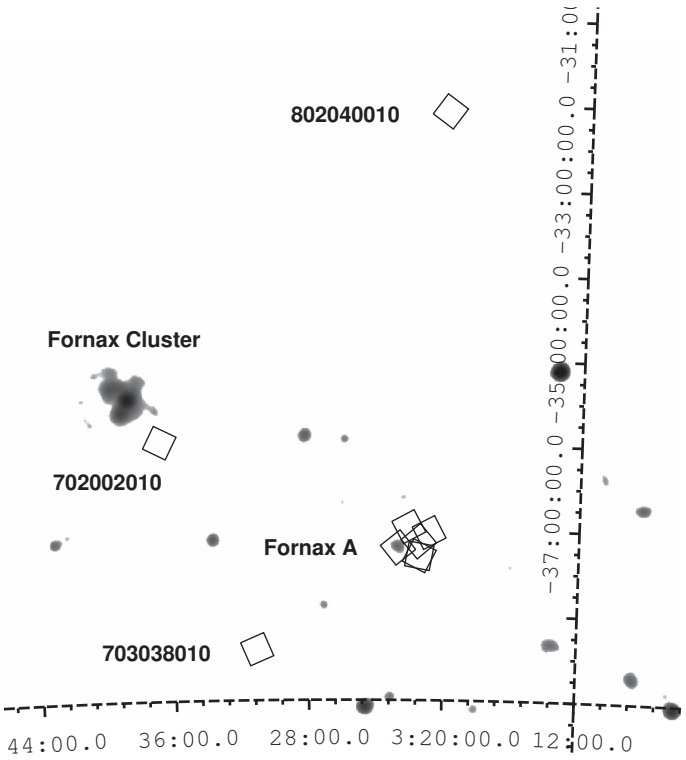

Figure 5.16: Positions of the field near the Fornax cluster. The gray scale image is 0.1–2keV image by the ROSAT all-sky survey. The squares shows the XIS field of view. The numbers show the observation ID for each observation.

photo-electric absorption model with an absorption column fixed to the Galactic value toward each region (Kalberla et al. 2005).

All the free parameters of the Galactic halo and CXB components were tied among all the spectral sets as they are not expected to vary as a function of the cluster-centric distance. The plasma temperature of the Fornax cluster thermal component was also set common among the three data sets as it was unconstrained with the spectrum taken at the furthermost region from the cluster center (sequence ID 802040010 in table 5.6).

The two thermal components (the Galactic halo and the cluster components) were easily distinguished as they have different typical temperatures and dependence to the distance from the cluster center. Unlike the former, the latter drops sharply as the distance increases. Indeed, the spectrum taken at the furthermost distance from the cluster (sequence ID 802040010) did not require the cluster thermal component, for which we derived a 1 σ

upper limit.

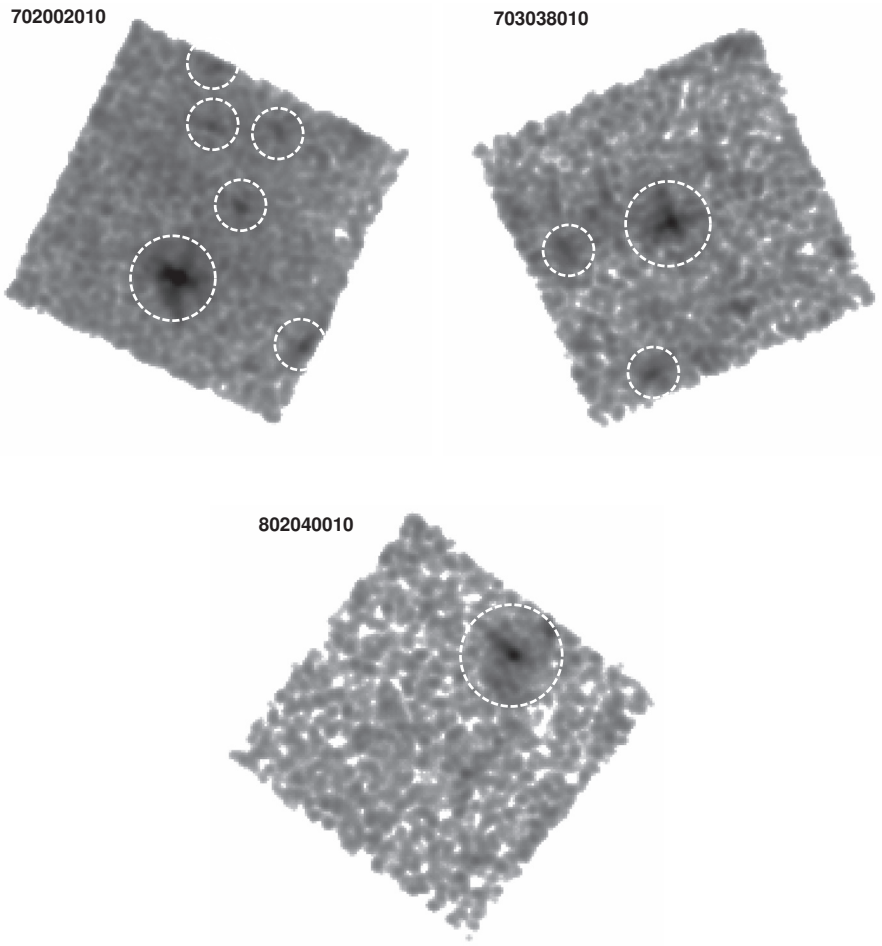

Figure 5.17: 0.5–10 keV image of the data with the sequence numbers 702002010 (left), 703038010 (right), and 802040010 (center). The dashed circles are masked regions around point-like sources.

Table 5.7 summarizes the fitting result, figure 5.18 shows the fitting spectra, and figure 5.19 presents the best-fit parameters as a function of the distance. Using this result, we estimated the level of the cluster thermal emission to be $\sim 8 \times 10^{-9}$ erg s^{-1} cm^{-2} str^{-1} at the position of Fornax A.

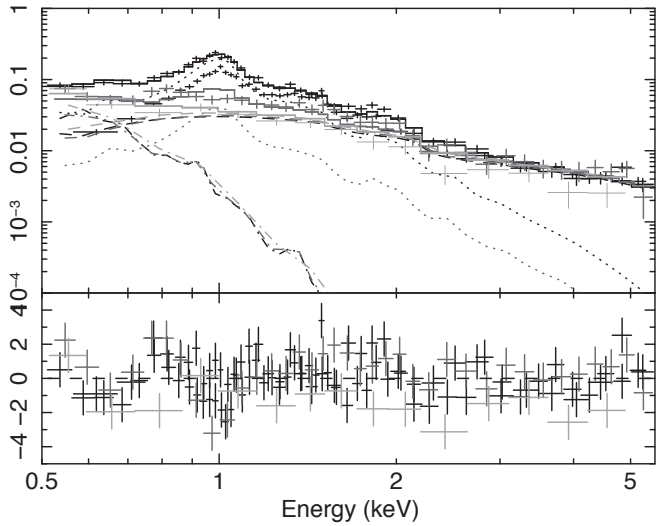

Figure 5.18: Best-fit model for the Fornax cluster component using the data in table 5.6. The BI spectra are shown for the sequence number 702002010 (black), 703038010 (red), and 802040010 (green). The model components are indicated in the GH component (dotted-and-dashed line), the CXB component (dashed line) and the cluster component (dotted line).

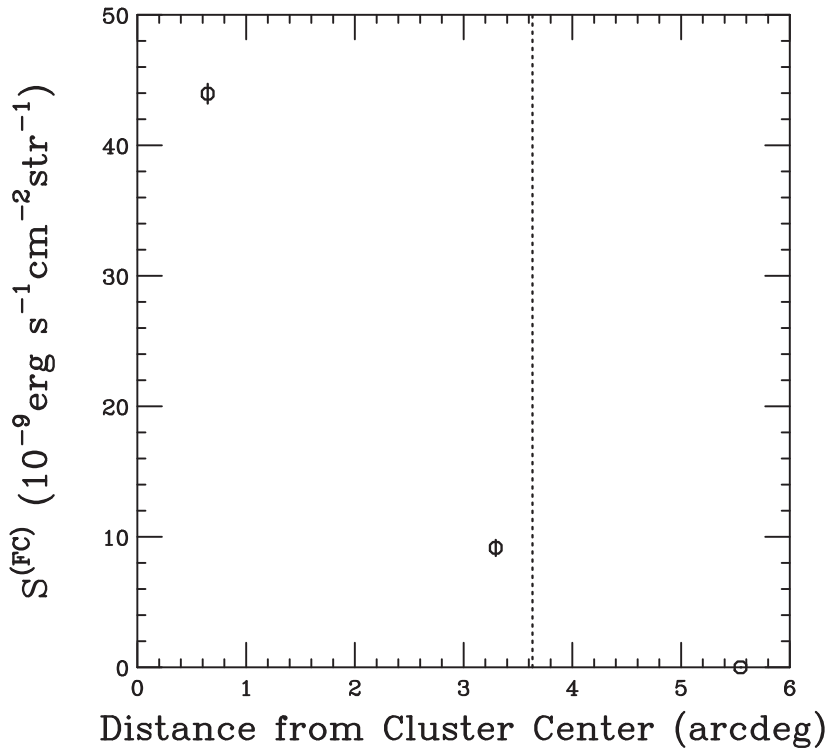

Figure 5.19: Best-fit surface brightness and their 1σ statistical uncertainty of the Fornax cluster component using the data in table 5.6. The vertical dotted line indicates the distance of Fornax A from the cluster center.

Table 5.7: Fitting result of the cluster component[ab].

Sequence	Absorption	Fornax cluster		Galactic halo		CXB	χ^2/d.o.f.
ID	$N_{\rm H} \times 10^{20}$	$kT^{\rm (FC)}$	$S^{\rm (FC)} \times 10^{-9}$	$kT^{\rm (GH)}$	$S^{\rm (GH)} \times 10^{-9}$	$S^{\rm (CXB)} \times 10^{-8}$	
	(1)	(2)	(3)	(4)	(5)	(6)	
Common	—	1.07 ± 0.01	—	0.18 ± 0.01	7.17 ± 0.62	5.74 ± 0.10	344.4/192
702002010	1.34	—	43.96 ± 0.43	—	—	—	—
703038010	1.77	—	9.15 ± 0.61	—	—	—	—
802040010	1.33	—	$<5 \times 10^{-16}$	—	—	—	—

[a] The best-fit parameters for (1) interstellar extinction $N_{\rm H}$ (cm^{-2}), (2) plasma temperature $kT^{\rm (FC)}$ (keV) and (3) surface brightness $S^{\rm (FC)}$ (erg s^{-1} cm^{-2} str^{-1}) of the Fornax cluster, (4) plasma temperature $kT^{\rm (GH)}$ (keV) and (5) surface brightness $S^{\rm (GH)}$ (erg s^{-1} cm^{-2} str^{-1}) of the Galactic halo, and (6) surface brightness $S^{\rm (CXB)}$ (erg s^{-1} cm^{-2} str^{-1}) of the CXB.

[b] The error ranges indicate 1 σ statistical uncertainty. The values without errors are those fixed in the fitting.

5.1.5.2 Galaxy Component

We refer to Kim et al. (1998); Kim & Fabbiano (2003); Konami et al. (2010) for the characterization of the diffuse X-ray emission associated with NGC 1316. Kim et al. (1998) and Kim & Fabbiano (2003) revealed, using the high-resolution X-ray imagers on-board the ROSAT and Chandra X-ray Observatory respectively, that diffuse X-ray emission exists in smoothed X-ray images after removing point-like sources. The morphology of the diffuse emission is elongated in the direction normal to the jet launching direction at its root. The extent of the diffuse emission is quite limited: the brightness drops by an order in 10″ in the radial profile (see figure 6 in Kim & Fabbiano 2003). The spectrum was modeled with a thermal plasma of a temperature of kT =0.5–0.6 keV.

Konami et al. (2010) used the same XIS data presented here (sequence ID 801015010 in figure 5.6) to analyze the X-ray spectrum of the diffuse emission in NGC 1316. Despite the limited imaging capability of Suzaku, they identified the spectrum of the diffuse plasma emission with it most prominent features of MgXI and Si XIII emission lines. These features are absent in their background region taken from 5′ away from the center of the galaxy, in which the spectrum was explained only by background emission. Figure 5.20 shows the brightness profile of direction from the galaxy to the western lobe. The effect of the galaxy component decrease at a distance of $\sim 7\ '$ from the galaxy. In our spectral analysis of the lobe below, we masked the circle of a 7′ radius around the galaxy, we therefore can safely assume that our diffuse X-ray spectrum in the lobe is free from the contamination by the galaxy component.

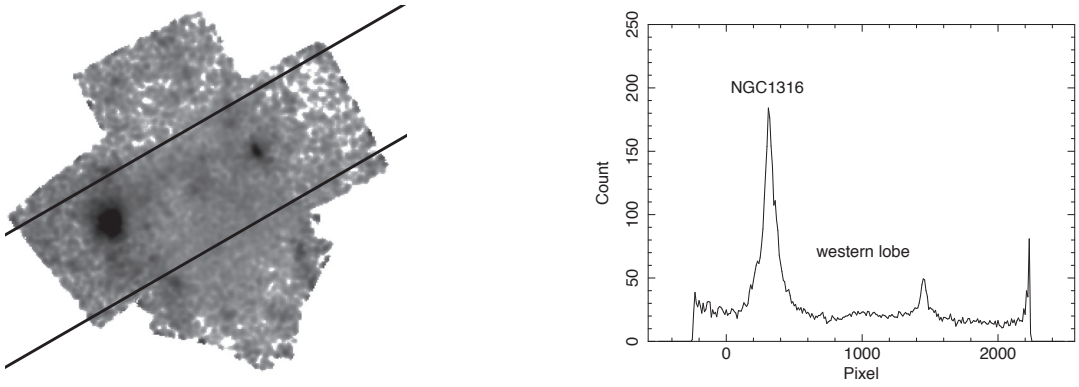

Figure 5.20: Cross-section (left) and profile (right) of the brightness of the western lobe. The pixel scale is 1.04″ pixel^{-1}.

5.1.5.3 Lobe Component

For the lobe component, we started with the spectrum extracted from an interior of the western lobe (the elliptical region "M" in figure 5.6a). Figure 5.21 (a) shows the NXB-subtracted spectrum. We first tried fitting with a model consisting only of the background emission components, i.e., the Galactic halo, the CXB, and unresolved point-like source emission. For the Galactic halo and the CXB components, we used the best-fit parameters derived in the off-lobe regions (table 5.7). Figure 5.21 (b) shows the residuals to the fit, in which a large data excess is seen peaking at ∼0.9 keV

In a close-up view of the spectrum in the soft-band (the inset in figure 5.21(a), several emission features are recognized. While the O VII and O VIII lines respectively at 0.57 and 0.65 keV are from the Galactic halo component with kT =0.2 keV, the Ne IX line at 0.91 keV and Fe L series lines at ∼1 keV should be from a thermal plasma of a higher temperature. We thus introduced a thermal plasma component represented by the `mekal` model with free parameters of the plasma temperature ($kT^{(\mathrm{lobe,T})}$) and the surface brightness ($S^{(\mathrm{lobe,T})}$) and a fixed parameter of the 0.3 solar abundance. The residuals improved substantially as shown in figure 5.21 (c) and yielded a statistically-acceptable result.

Following the previous work (Tashiro et al. 2009), we further added the lobe non-thermal component for the inverse Compton emission. The free parameter is the surface brightness ($S^{(\mathrm{lobe,NT})}$) and the photon index was fixed to –1.68 (Isobe et al. 2006). The fitting improved slightly with little change in the best-fit parameters of the lobe thermal component. The residuals are shown in figure 5.21 (d). The best-fit parameters of the non-thermal component is consistent with previous works (Isobe et al. 2006; Tashiro et al. 2009) except for a lower normalization of the power-law component in our work. This is probably due to a different method in estimating the contribution of point-like sources. The count rate statistics of all the aforementioned components are summarized in table 5.8, while the best-fit spectral parameters are given in table 5.9.

In order to investigate the spatial extent and variation of the lobe thermal emission, we defined three sets of source regions for spatially-resolved spectroscopy. For the first set, we divided the inside and outside of the lobe radially into four sections R1–R4 with R3+R4 being the region "M". For the second set, we divided the "M" region into north and source ("MN" and "MS", respectively). For the third set, we divided the "M" region into east and west ("ME" and "MW", respectively). For these sets of regions, we conducted the spectral

modeling in the same approach with the region "M". The result is summarized in table 5.8 for the count rate statistics and table 5.9 for the best-fit parameters.

Table 5.8: Count rate statistics in the lobe component[ab].

Region	Total	NXB	GH	CXB	PS	Lobe[c]
R1	$29.37^{+0.21}_{-0.21}$	$9.07^{+9.07}_{-9.07}{}^{+0.31}_{-0.31}$	$0.56^{+0.05}_{-0.05}$	$7.01^{+0.67}_{0.67}$	$3.71^{+0.20}_{-0.20}$	$9.02^{+0.22}_{-0.22}{}^{+0.77}_{-0.77}$
R1N	$28.28^{+0.30}_{-0.30}$	$8.86^{+8.86}_{-8.86}{}^{+0.47}_{-0.47}$	$0.59^{+0.05}_{-0.05}$	$7.51^{+0.72}_{0.72}$	$0.33^{+0.03}_{-0.04}$	$10.99^{+0.31}_{-0.31}{}^{+0.86}_{-0.86}$
R1S	$19.13^{+0.19}_{-0.19}$	$5.71^{+5.71}_{-5.71}{}^{+0.28}_{-0.28}$	$0.33^{+0.03}_{-0.03}$	$4.15^{+0.40}_{0.40}$	$4.31^{+0.23}_{-0.23}$	$4.62^{+0.19}_{-0.19}{}^{+0.54}_{-0.54}$
R2	$32.97^{+0.22}_{-0.22}$	$9.01^{+9.01}_{-9.01}{}^{+0.32}_{-0.32}$	$0.62^{+0.05}_{-0.05}$	$7.55^{+0.72}_{0.72}$	$4.62^{+0.24}_{-0.24}$	$11.17^{+0.23}_{-0.23}{}^{+0.83}_{-0.83}$
R2N	$16.37^{+0.18}_{-0.18}$	$4.29^{+4.29}_{-4.29}{}^{+0.25}_{-0.25}$	$0.31^{+0.03}_{-0.03}$	$3.87^{+0.37}_{0.37}$	$2.65^{+0.15}_{-0.15}$	$5.26^{+0.18}_{-0.18}{}^{+0.47}_{-0.47}$
R2S	$23.64^{+0.21}_{-0.21}$	$6.51^{+6.51}_{-6.51}{}^{+0.30}_{-0.30}$	$0.44^{+0.04}_{-0.04}$	$5.31^{+0.51}_{0.51}$	$3.16^{+0.17}_{-0.17}$	$8.22^{+0.21}_{-0.21}{}^{+0.61}_{-0.61}$
R3	$26.99^{+0.20}_{-0.20}$	$6.40^{+6.40}_{-6.40}{}^{+0.25}_{-0.25}$	$0.47^{+0.04}_{-0.04}$	$5.34^{+0.51}_{0.51}$	$4.79^{+0.25}_{-0.25}$	$9.99^{+0.21}_{-0.21}{}^{+0.62}_{-0.62}$
R3N	$10.78^{+0.13}_{-0.13}$	$2.60^{+2.60}_{-2.60}{}^{+0.17}_{-0.17}$	$0.19^{+0.02}_{-0.02}$	$2.06^{+0.20}_{0.20}$	$2.74^{+0.15}_{-0.15}$	$3.19^{+0.13}_{-0.13}{}^{+0.30}_{-0.30}$
R3S	$19.48^{+0.19}_{-0.19}$	$4.69^{+4.69}_{-4.69}{}^{+0.25}_{-0.25}$	$0.34^{+0.03}_{-0.03}$	$3.93^{+0.38}_{0.38}$	$2.60^{+0.14}_{-0.14}$	$7.92^{+0.19}_{-0.19}{}^{+0.47}_{-0.47}$
R4	$14.78^{+0.16}_{-0.16}$	$2.92^{+2.92}_{-2.92}{}^{+0.19}_{-0.19}$	$0.22^{+0.02}_{-0.02}$	$2.71^{+0.26}_{0.26}$	$3.50^{+0.19}_{-0.19}$	$5.42^{+0.16}_{-0.16}{}^{+0.37}_{-0.37}$
R4N	$6.53^{+0.11}_{-0.11}$	$1.19^{+1.19}_{-1.19}{}^{+0.12}_{-0.11}$	$0.08^{+0.01}_{-0.01}$	$1.10^{+0.11}_{0.11}$	$2.28^{+0.13}_{-0.13}$	$1.88^{+0.11}_{-0.11}{}^{+0.20}_{-0.20}$
R4S	$9.67^{+0.15}_{-0.15}$	$1.91^{+1.91}_{-1.91}{}^{+0.16}_{-0.16}$	$0.14^{+0.01}_{-0.01}$	$1.91^{+0.18}_{0.18}$	$1.29^{+0.08}_{-0.08}$	$4.43^{+0.15}_{-0.15}{}^{+0.25}_{-0.25}$
M	$39.98^{+0.25}_{-0.25}$	$9.03^{+9.03}_{-9.03}{}^{+0.31}_{-0.31}$	$0.67^{+0.06}_{-0.06}$	$7.71^{+0.74}_{0.74}$	$7.86^{+0.40}_{-0.40}$	$14.72^{+0.25}_{-0.25}{}^{+0.90}_{-0.90}$
MN	$16.71^{+0.16}_{-0.16}$	$3.64^{+3.64}_{-3.64}{}^{+0.20}_{-0.20}$	$0.27^{+0.02}_{-0.02}$	$3.06^{+0.29}_{0.29}$	$4.80^{+0.25}_{-0.25}$	$4.94^{+0.16}_{-0.16}{}^{+0.43}_{-0.43}$
MS	$27.77^{+0.23}_{-0.23}$	$6.38^{+6.38}_{-6.38}{}^{+0.29}_{-0.29}$	$0.48^{+0.04}_{-0.04}$	$5.55^{+0.53}_{0.53}$	$3.78^{+0.20}_{-0.20}$	$11.58^{+0.23}_{-0.23}{}^{+0.64}_{-0.64}$
ME	$22.00^{+0.18}_{-0.18}$	$4.70^{+4.70}_{-4.70}{}^{+0.23}_{-0.23}$	$0.36^{+0.03}_{-0.03}$	$4.33^{+0.41}_{0.41}$	$3.87^{+0.20}_{-0.20}$	$8.75^{+0.19}_{-0.19}{}^{+0.52}_{-0.52}$
MW	$20.41^{+0.19}_{-0.19}$	$4.83^{+4.83}_{-4.83}{}^{+0.24}_{-0.24}$	$0.34^{+0.03}_{-0.03}$	$3.86^{+0.37}_{0.37}$	$4.51^{+0.24}_{-0.24}$	$6.88^{+0.19}_{-0.19}{}^{+0.50}_{-0.50}$

[a] The count rate statistics in the 0.5–5.5 keV range with the FI sensors are given in the unit of 10^{-3} s^{-1}.

[b] The error ranges indicate 1 σ statistical uncertainty. For the NXB and PS components, 1 σ statistical uncertainty and 1 σ systematic uncertainty, for first and secondary errors, respectively.

[c] The lobe component is calculated as the subtraction of other components from the total rate.

Table 5.9: Best-fit parameters of lobe component for each region.

Region	Thermal		Non-thermal	χ^2/d.o.f.
	$kT^{(\mathrm{lobe,T})}$	$S^{(\mathrm{lobe,T})} \times 10^{-8}$	$S^{(\mathrm{lobe,NT})} \times 10^{-2}$	
	(1)	(2)	(3)	
R1	—	—	—	3799.2/317
	$0.84^{+-0.84}_{-0.84}$	$1.51^{+-1.51}_{-1.51}$	—	822.6/315
	$0.74^{+0.02}_{-0.02}$	$1.06^{+0.05}_{-0.05}$	$36.97^{+1.81}_{-1.80}$	374.8/314

R1N	—	—	—	2535.3/153
	$0.84\ ^{+-0.84}_{-0.84}$	$1.64\ ^{+-1.64}_{-1.64}$	—	609.1/151
	$0.68\ ^{+0.02}_{-0.02}$	$1.11\ ^{+0.06}_{-0.06}$	$46.36\ ^{+2.29}_{-2.28}$	224.8/150
R1S	—	—	—	1428.6/176
	$0.85\ ^{+0.02}_{-0.02}$	$1.40\ ^{+0.06}_{-0.06}$	—	281.7/174
	$0.78\ ^{+0.03}_{-0.03}$	$1.06\ ^{+0.07}_{-0.07}$	$27.63\ ^{+2.67}_{-2.65}$	168.6/173
R2	—	—	—	5499.8/352
	$0.86\ ^{+-0.86}_{-0.86}$	$1.89\ ^{+-1.89}_{-1.89}$	—	890.3/350
	$0.79\ ^{+0.01}_{-0.01}$	$1.40\ ^{+0.05}_{-0.05}$	$3.56\ ^{+0.16}_{-0.16}$	373.7/349
R2N	—	—	—	2134.3/150
	$0.80\ ^{+0.01}_{-0.01}$	$1.92\ ^{+0.06}_{-0.06}$	—	277.0/148
	$0.73\ ^{+0.02}_{-0.04}$	$1.53\ ^{+0.07}_{-0.07}$	$2.79\ ^{+0.25}_{-0.24}$	142.0/147
R2S	—	—	—	3280.4/214
	$1.06\ ^{+-1.06}_{-1.06}$	$1.96\ ^{+-1.96}_{-1.96}$	—	556.5/212
	$0.85\ ^{+0.02}_{-0.02}$	$1.27\ ^{+0.06}_{-0.06}$	$4.07\ ^{+0.21}_{-0.21}$	267.9/211
R3	—	—	—	4849.5/289
	$0.86\ ^{+-0.86}_{-0.86}$	$2.11\ ^{+-2.11}_{-2.11}$	—	1014.3/287
	$0.77\ ^{+0.02}_{-0.02}$	$1.40\ ^{+0.06}_{-0.06}$	$4.49\ ^{+0.18}_{-0.18}$	327.4/286
R3N	—	—	—	1507.0/126
	$0.79\ ^{+0.02}_{-0.02}$	$2.06\ ^{+0.08}_{-0.08}$	—	240.9/124
	$0.72\ ^{+0.03}_{-0.02}$	$1.64\ ^{+0.09}_{-0.09}$	$2.76\ ^{+0.27}_{-0.28}$	139.6/123
R3S	—	—	—	3266.0/173
	$2.21\ ^{+-2.21}_{-2.21}$	$2.66\ ^{+-2.66}_{-2.66}$	—	436.8/171
	$0.82\ ^{+0.02}_{-0.02}$	$1.21\ ^{+0.07}_{-0.07}$	$5.41\ ^{+0.23}_{-0.23}$	213.7/170
R4	—	—	—	2399.5/139
	$0.88\ ^{+-0.88}_{-0.88}$	$2.39\ ^{+-2.39}_{-2.39}$	—	437.9/137
	$0.81\ ^{+0.02}_{-0.02}$	$1.68\ ^{+0.09}_{-0.09}$	$4.35\ ^{+0.27}_{-0.27}$	156.4/136
R4N	—	—	—	782.3/65
	$0.80\ ^{+0.02}_{-0.02}$	$2.42\ ^{+0.13}_{-0.13}$	—	95.0/63
	$0.75\ ^{+0.03}_{-0.06}$	$2.05\ ^{+0.15}_{-0.15}$	$2.43\ ^{+0.43}_{-0.42}$	61.4/62
R4S	—	—	—	1737.2/73
	$2.25\ ^{+-2.25}_{-2.25}$	$3.12\ ^{+-3.12}_{-3.12}$	—	190.1/71
	$0.85\ ^{+0.03}_{-0.03}$	$1.47\ ^{+0.11}_{-0.11}$	$6.09\ ^{+0.35}_{-0.35}$	73.2/70
M	—	—	—	7232.7/409
	$0.86\ ^{+-0.86}_{-0.86}$	$2.20\ ^{+-2.20}_{-2.20}$	—	1437.5/407

	$0.78\ ^{+0.01}_{-0.01}$	$1.50\ ^{+0.05}_{-0.05}$	$4.43\ ^{+0.15}_{-0.15}$	475.3/406
MN	—	—	—	2277.8/188
	$0.80\ ^{+0.01}_{-0.01}$	$2.21\ ^{+0.07}_{-0.07}$	—	316.6/186
	$0.73\ ^{+0.02}_{-0.02}$	$1.79\ ^{+0.08}_{-0.08}$	$2.74\ ^{+0.23}_{-0.23}$	174.6/185
MS	—	—	—	4922.0/242
	$1.12\ ^{+-1.12}_{-1.12}$	$2.42\ ^{+-2.42}_{-2.42}$	—	909.9/240
	$0.84\ ^{+0.02}_{-0.02}$	$1.28\ ^{+0.06}_{-0.06}$	$5.54\ ^{+0.19}_{-0.19}$	258.4/239
ME	—	—	—	4529.8/237
	$0.86\ ^{+-0.86}_{-0.86}$	$2.28\ ^{+-2.28}_{-2.28}$	—	958.1/235
	$0.77\ ^{+0.02}_{-0.02}$	$1.51\ ^{+0.06}_{-0.06}$	$4.91\ ^{+0.19}_{-0.19}$	266.2/234
MW	—	—	—	2763.4/193
	$0.87\ ^{+-0.87}_{-0.87}$	$2.10\ ^{+-2.10}_{-2.10}$	—	527.3/191
	$0.80\ ^{+0.02}_{-0.02}$	$1.46\ ^{+0.07}_{-0.07}$	$3.98\ ^{+0.23}_{-0.23}$	205.8/190

[a] The best-fit parameters for the (1) plasma temperature $kT^{(\mathrm{FC})}$ (keV) and (2) 0.5–2 keV surface brightness $S^{(\mathrm{FC})}$ (erg s^{-1} cm^{-2} str^{-1}) of the thermal emission, and (3) 2–10 keV surface brightness $S^{(\mathrm{FC})}$ (erg s^{-1} cm^{-2} str^{-1}) of the non-thermal emission of the lobe component. Two models with and without the non-thermal component were employed. The photo-electric absorption column was fixed to 2.06 $\times$ 10^{-20} cm^{-2}, and the power-law index of the non-thermal component was fixed to -1.68. The surface brightness is measured in the 0.5–2.0 keV range for the thermal components and 2.0–10.0 keV range for the non-thermal components.

[b] The error ranges indicate 1 σ statistical uncertainty.

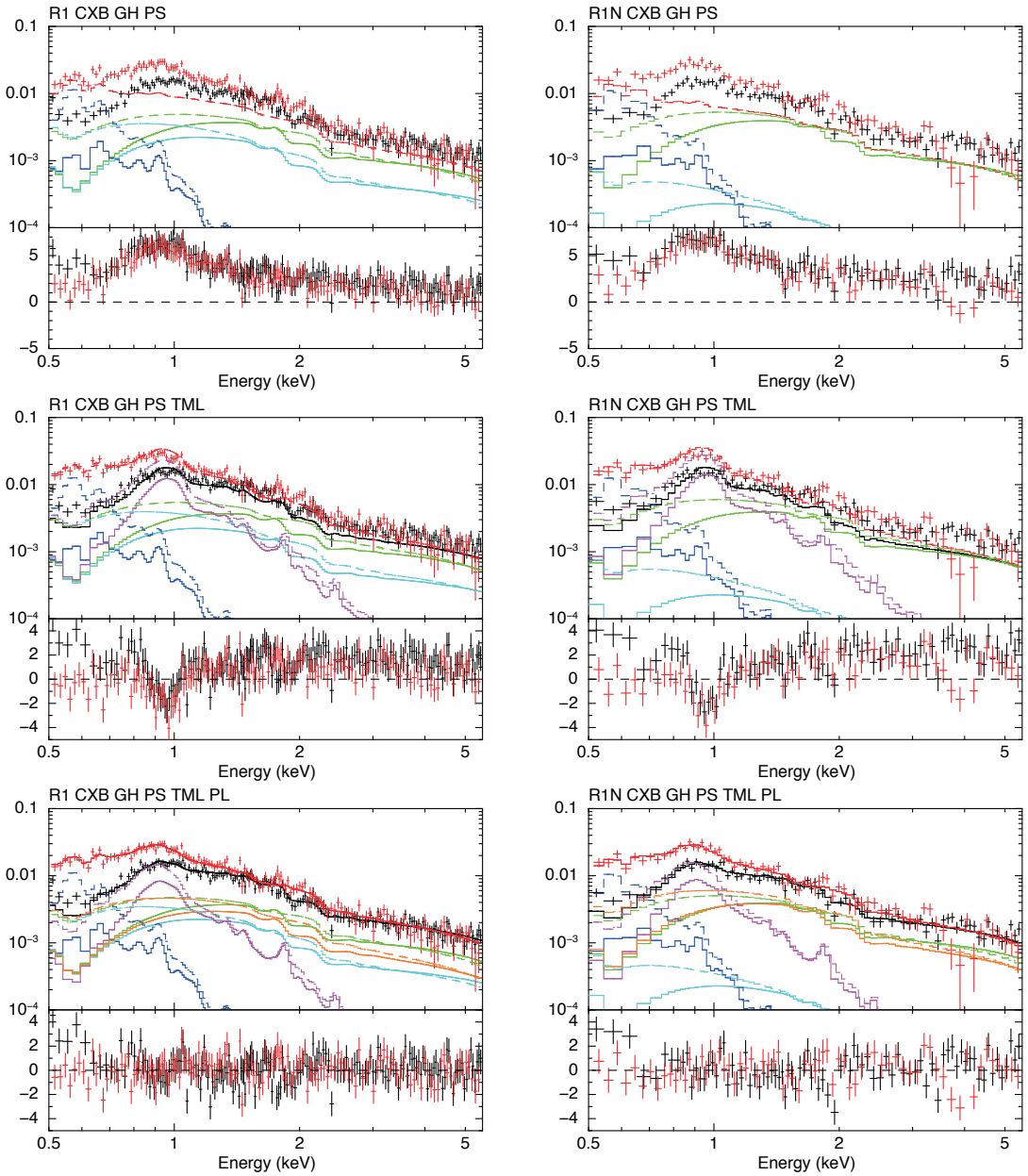

Figure 5.21: Best-fit spectra for R1 (left) and R1N (right). The FI spectrum is shown with black data and solid line models, while the BI spectrum is shown with red data and dashed line models. (top) The NXB-subtracted spectra together with the model consisting only of the background emission components (Galactic halo (blue), CXB (green), and unresolved point-like sources(cyan)). (middle) The model consists of the background emission and the lobe thermal emission components (purple). (bottom) The model consists of the background emission and the lobe thermal and non-thermal emission (orange). components.

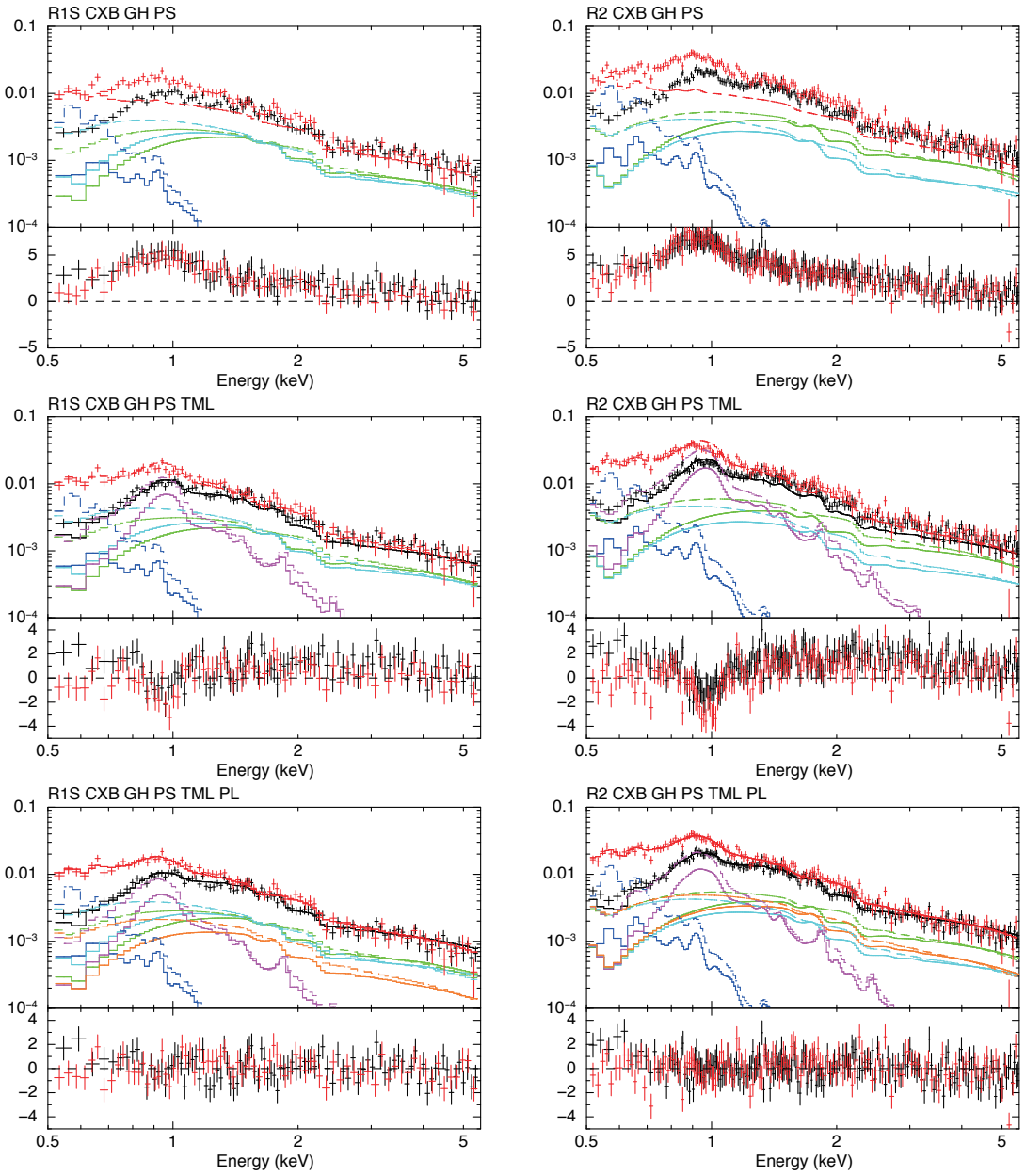

Figure 5.22: Best-fit spectra for R1S (left) and R2 (right).

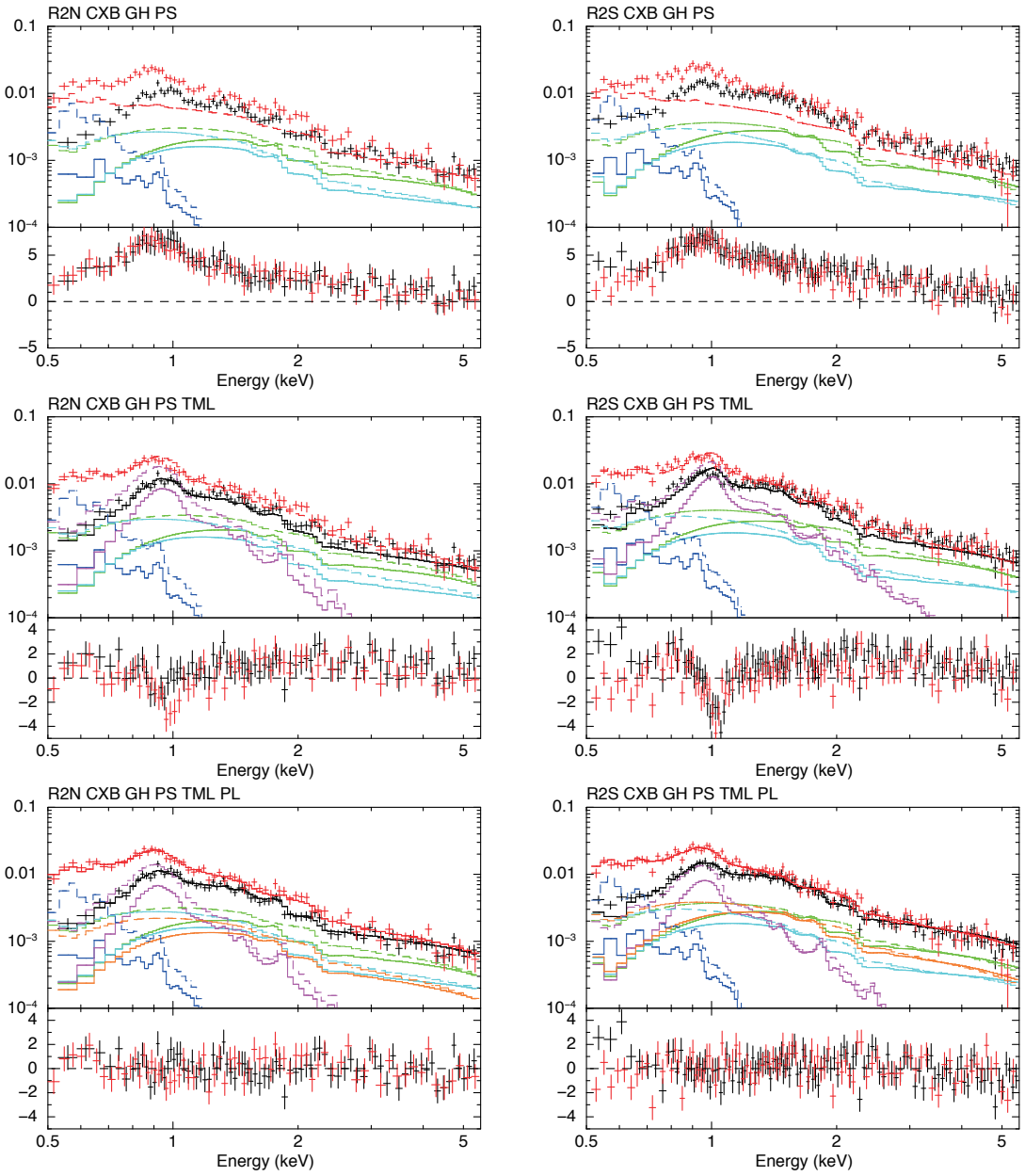

Figure 5.23: Best-fit spectra for R2N (left) and R2S (right).

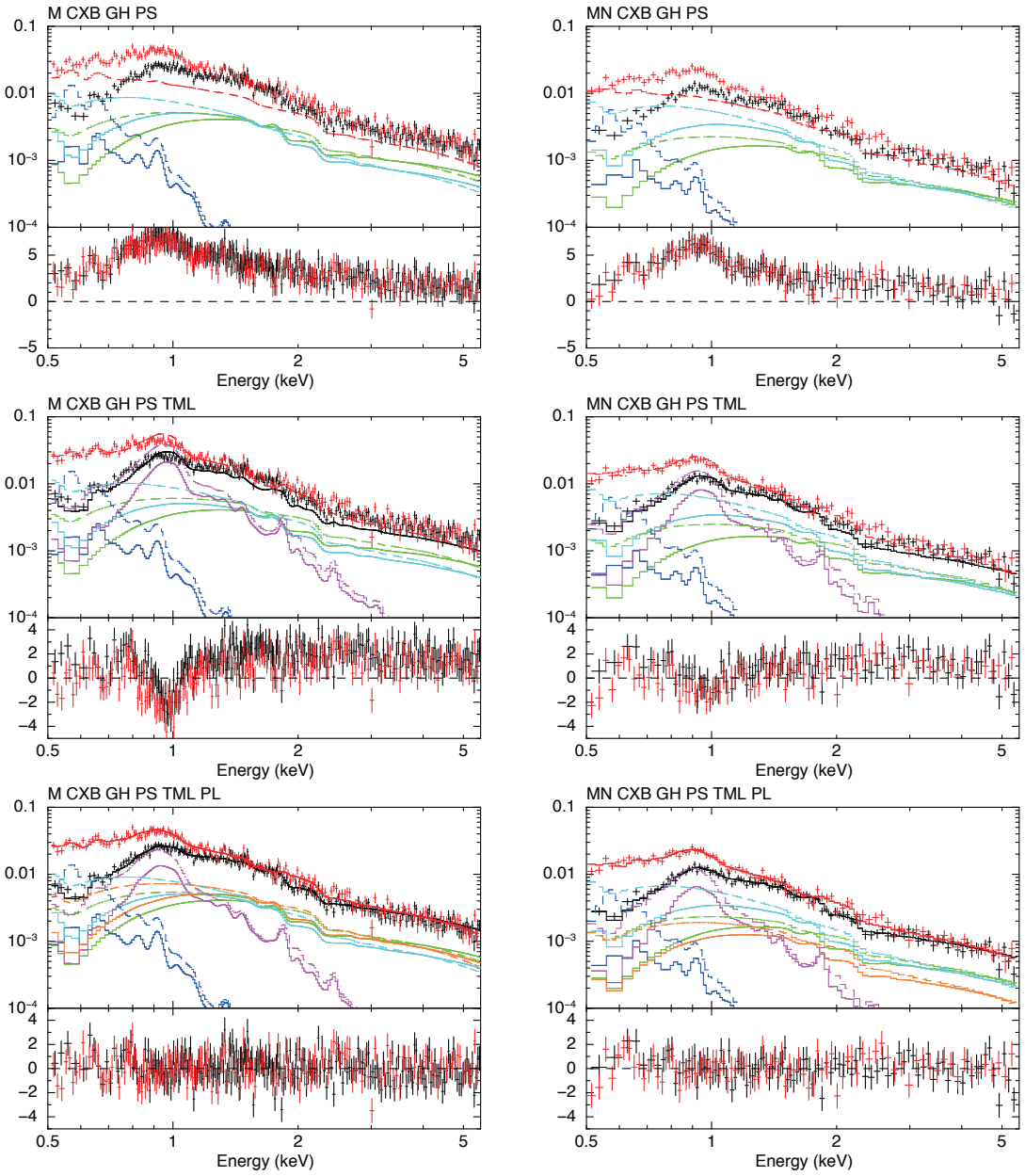

Figure 5.24: Best-fit spectra for R3 (left) and R3N (right).

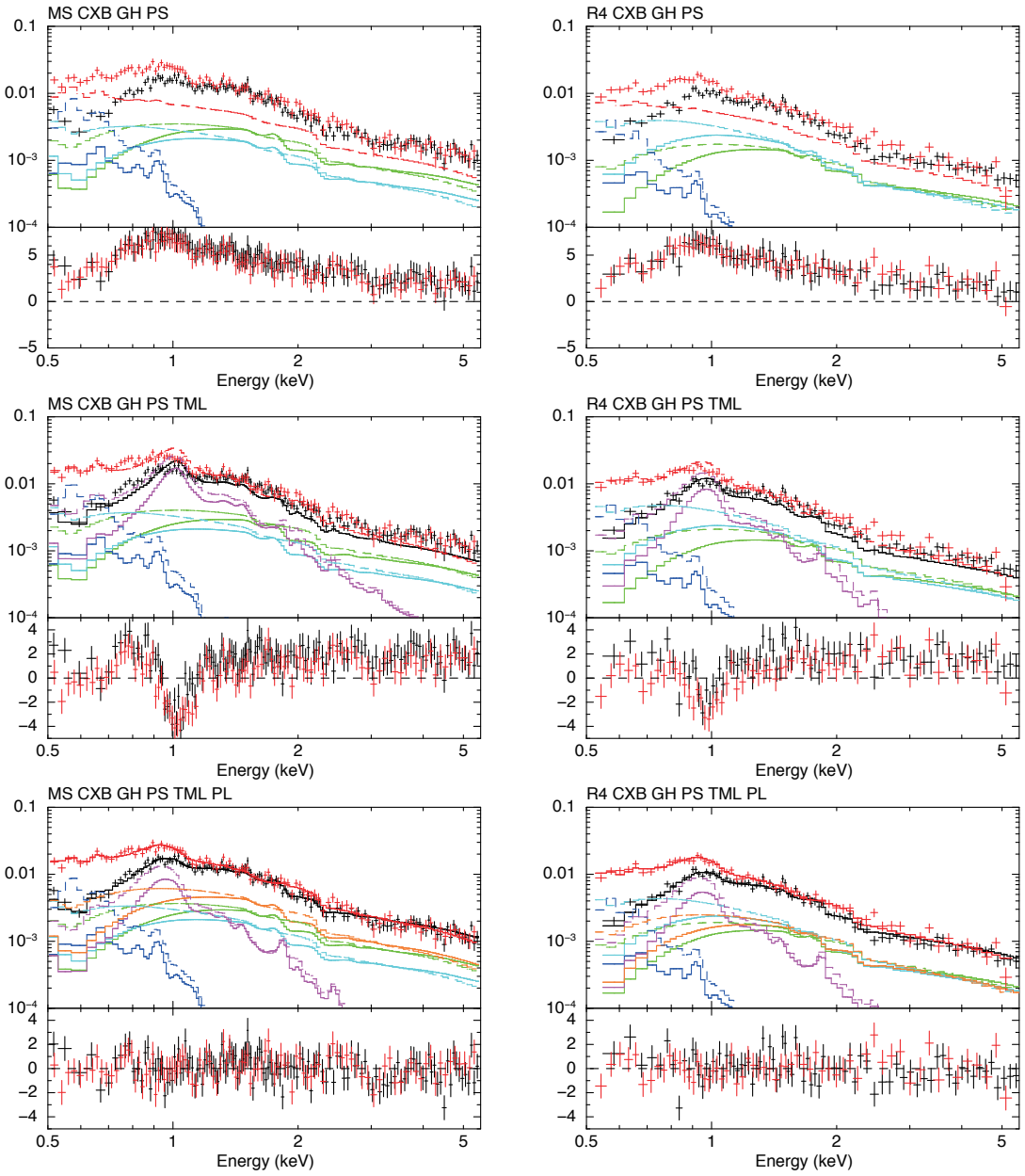

Figure 5.25: Best-fit spectra for R3S (left) and R4 (right).

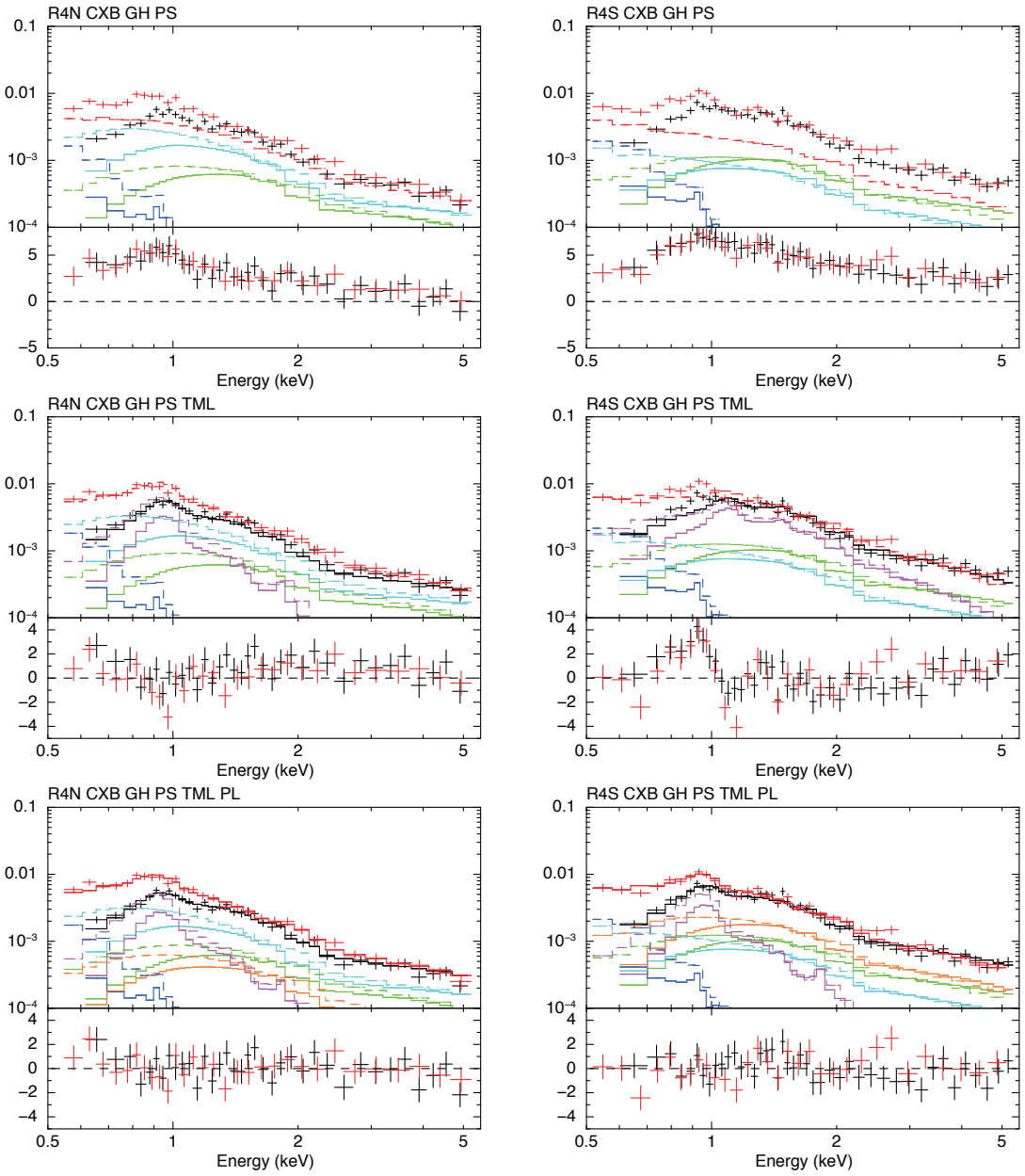

Figure 5.26: Best-fit spectra for R4N (left) and R4S (right).

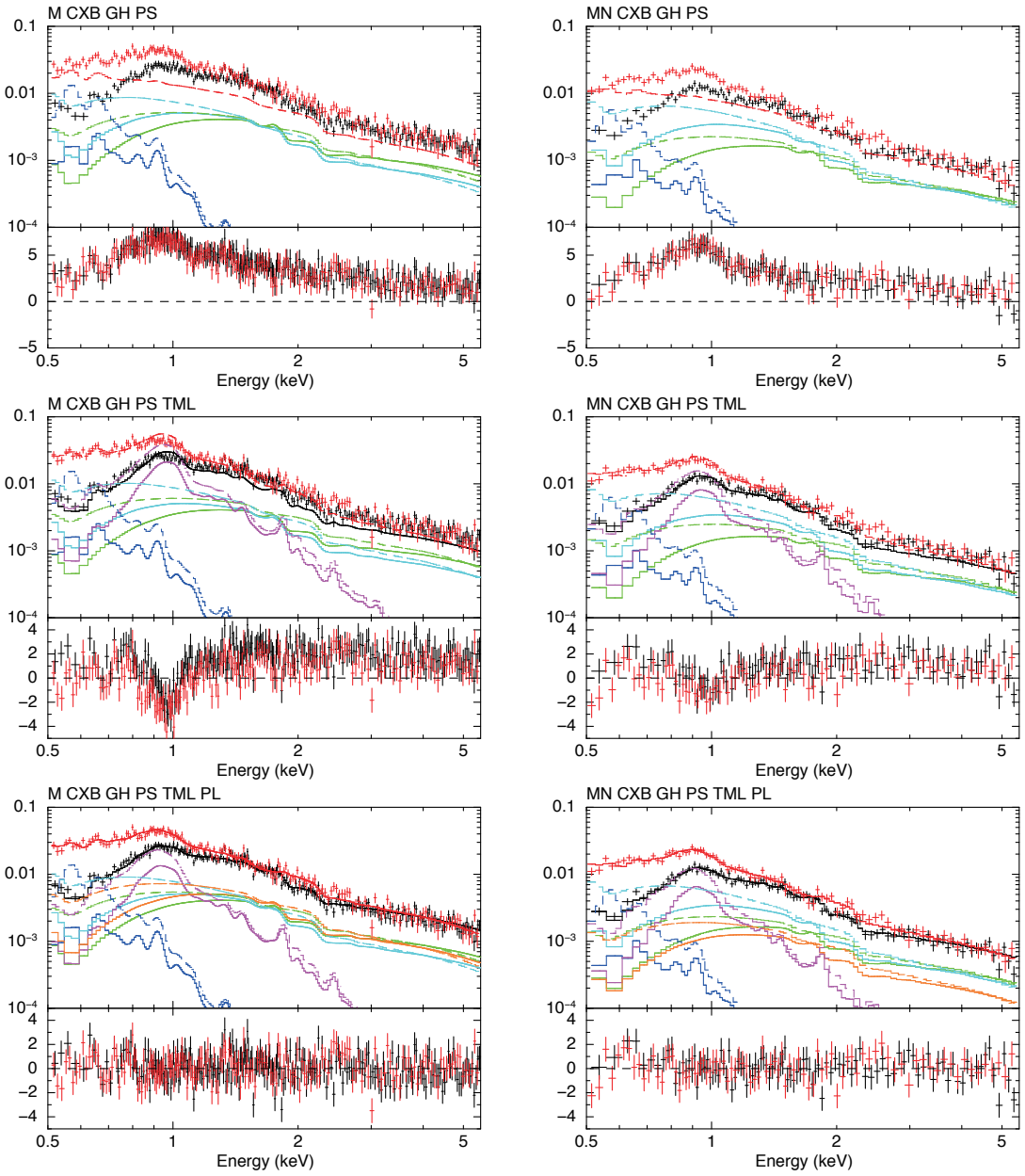

Figure 5.27: Best-fit spectra for M (left) and MN (right).

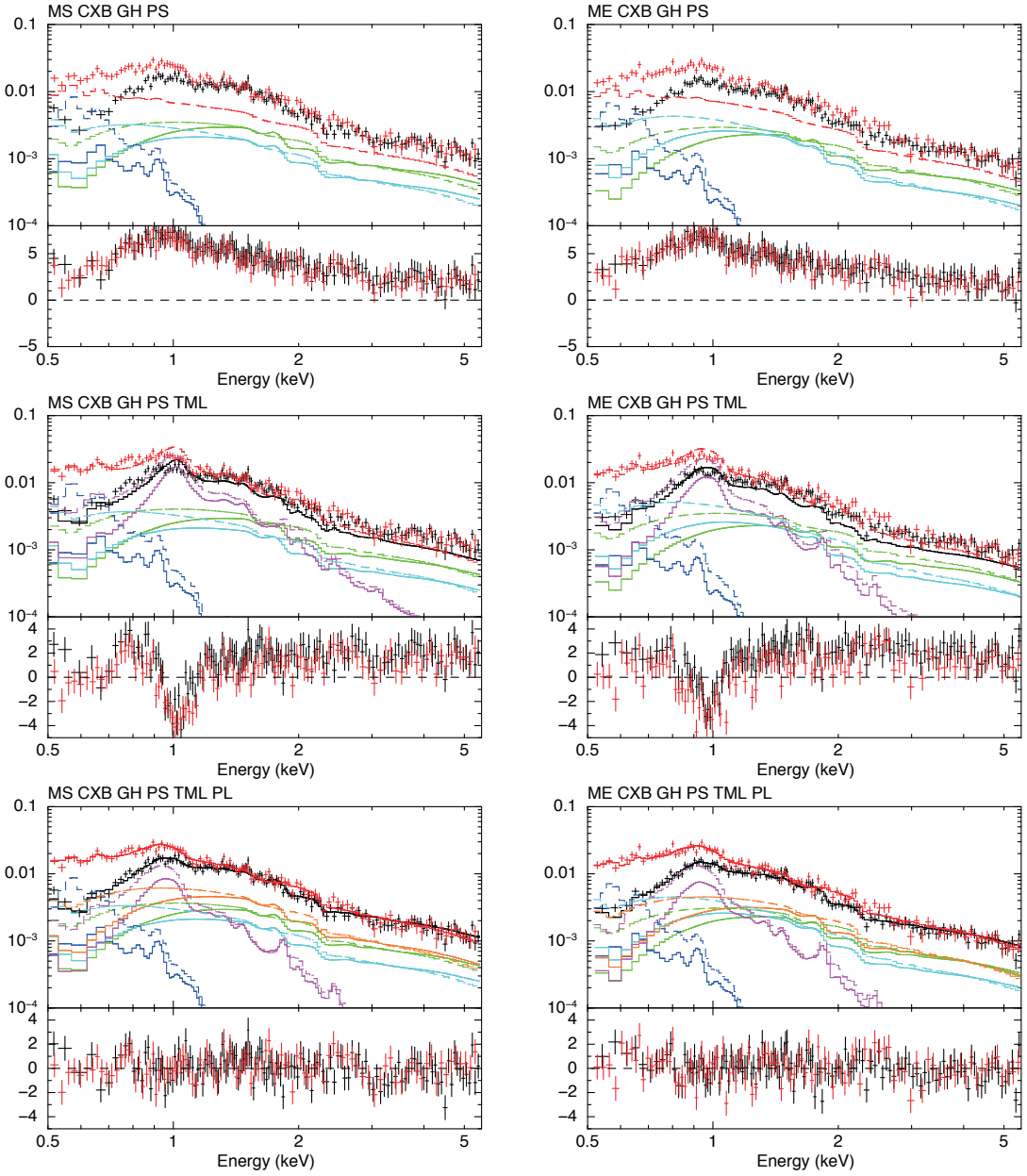

Figure 5.28: Best-fit spectra for MS (left) and ME (right).

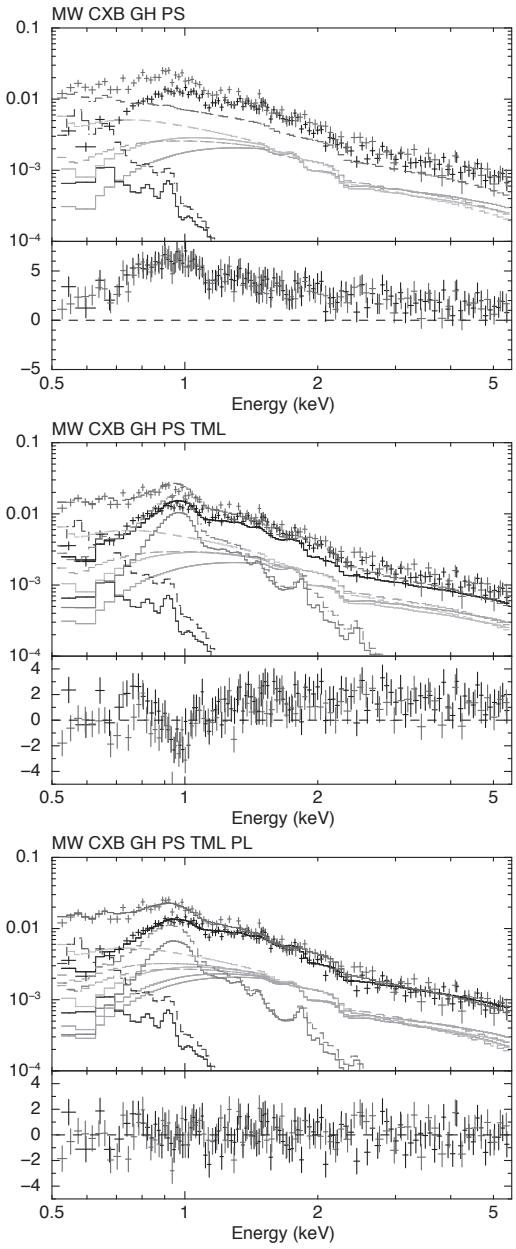

Figure 5.29: Best-fit spectra for MW.

5.2 Discussion

5.2.1 Presence of Lobe Thermal Emission

Our Suzaku observations have confirmed the presence of the diffuse thermal emission in the western lobe of Fornax A. We investigated its spatial distribution and revealed that the emission is associated to the lobe. This thin thermal plasma cannot be explained neither by Galactic halo, Fornax cluster, nor NGC 1316 interstellar plasmas, for following three lines of evidence.

First, we found the Ne IX and Fe L series emission features in the X-ray spectrum (figure 5.21M), which cannot be explained by the Galactic halo emission with a typical plasma temperature of $\sim$0.2 keV. Second, we measured the radial profile of the cluster component (figure 5.19) to estimate the expected surface brightness at the position of Fornax A ($\sim 8 \times 10^{-9}$ erg s^{-1} cm^{-2} str^{-1}) should be less than a half of the observed surface brightness in the lobe (table 5.7). Third, the spatial distribution of the lobe component is distinctively different from the galaxy component (figure 5.6). The extent of the galaxy component is very small of $\lesssim 10''$. The image (figure 5.6) clearly shows that the peak of the component is not at the galaxy but at the center of the western lobe.

5.2.2 Total Energy of Lobe Thermal and Non-thermal Emissions in the Entire Lobe

Upon the confirmation of the presence of the diffuse thermal emission of the lobe, we estimate its total energy. The best-fit `mekal` normalization $N_{\rm mekal}$ relates to the electron density $n_{\rm e}$ as

$$n_{\rm e} = \sqrt{\frac{4\pi D_{\rm A}(1+z)^2 \times 10^{14} N_{\rm mekal}}{Vf}}, \tag{5.1}$$

in which $D_{\rm A}$ is the angular distance (18.6 Mpc), z is the red-shift (4.65×10^{-4}; Tashiro et al. (2009)), and V is the emitting volume, and f is the volume filling factor. We assume a sphere as the emitting region with an angular radius of θ =12$'$ (Tashiro et al. 2009) as the emitting volume, thus $V = 4\pi(D_{\rm A}\theta)^3/3$. Adopting the best-fit value in the region "M", we derived the electron density $n_{\rm e}^{\rm T} = 1.87 \times 10^{-4}/\sqrt{f}$ cm^{-3} and the thermal energy density $u_{\rm th} = 3n_{\rm e}kT = 7.02 \times 10^{-13}$ erg cm$^{-3}/\sqrt{f}$.

The non-thermal emission was clearly resolved through the X-ray spectral analysis. That allowed us to estimate the energy densities of the non-thermal electrons ($u_{\rm e}$) and the magnetic field ($u_{\rm m}$) according to Harris & Grindlay (1979). The energy densities of electrons and magnetic field are calculated as $u_{\rm e} = (3.27 \pm 0.11) \times 10^{-13}$ erg cm^{-3} and $u_{\rm m} = (0.77 \pm 0.03) \times 10^{-13}$ erg cm^{-3}, respectively. Here, we evaluated $u_{\rm e}$ for the electrons with a Lorenz factor of $\gamma = 10^3$–10^5, which corresponds to the observed synchrotron radio and/or IC X-ray emission. The error is due to the statistical error of the X-ray flux density. The ratio of the two energy densities is $u_{\rm e}/u_{\rm m} = 4.3 \pm 0.3$.

5.2.3 Radial Profile of Lobe Emission in the entire lobe

We next study the two diffuse emissions by spectral fitting for the annulus in the regions R1–R4 (table 5.9) centered at the western lobe (figure 5.6). Figure 5.30 shows the radial profiles of (a) the plasma temperature, (b) the electron density and, (c) the surface brightness of the diffuse thermal emission, (d) the surface brightness of the diffuse non-thermal emission, and (e) 1.5 GHz intensity (Fomalont et al. 1989).

Evey physical parameter derived from the thermal emission (kT, $n_{\rm e}^{\rm T}$ and $S^{\rm lobe,T}$) exhibits significant association with the lobe. On the other hand, the brightness profile of the non-thermal X-ray emission (figure 5.30d) drops more sharply than that of the radio lobe extent shown by the 1.5 GHz emission profile (figure 5.30e). This is consistent with the claim by Tashiro et al. (2001). Comparing the two diffuse emissions, we note that the brightness profile of the thermal X-ray emission (figure 5.30c) is more extended than that of the non-thermal emission. In order to test whether the emission has a spherical or shell-type (sphere with a void sphere inside) emitting volume, we also plotted the projected model radial profiles of a fully-resolved case (figure 5.30e) and those convolved with a point spread function of the XIS (figure 5.30c). We assumed here that the emission is completely optically-thin and with uniform emissivity. The observed profile of the thermal X-ray emission is consistent with the spherical distribution, and there is no indication of rim brightening suggesting a shell-like structure. We thus naturally conclude that the diffuse X-ray emission is filled in the lobe.

In addition, we derived the energy densities for thermal and non-thermal plasma using the obtained physical parameters. Figure 5.31 shows the three energy densities; $u_{\rm th}$ (diamonds), $u_{\rm e}$ (circles), and $u_{\rm m}$ ("x" shaped) for each annulus region. Those value of the densities in the inner lobe two regions range within 10^{-13}–10^{-14} erg s^{-1} cm^{-3}. As for the

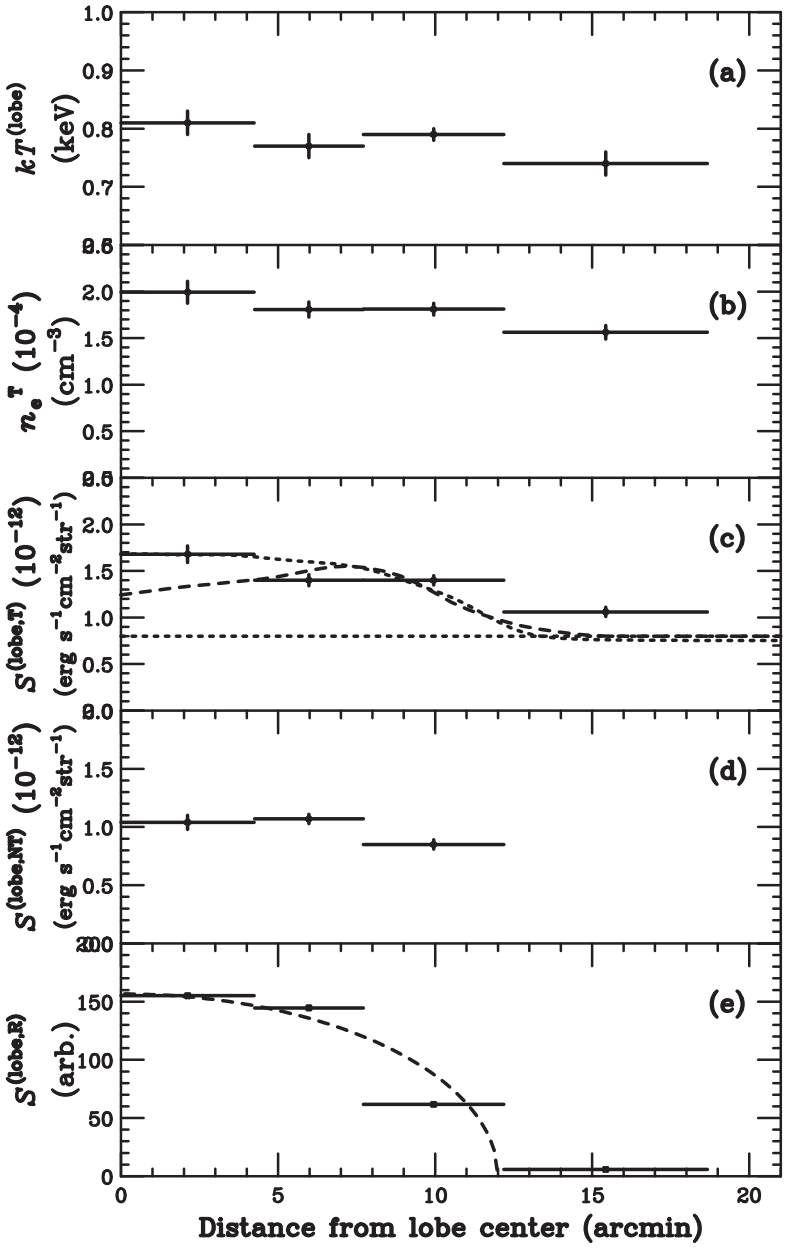

Figure 5.30: Radial profiles of (a) the plasma temperature $kT^{(\mathrm{lobe,T})}$ and (b) the electron density $n_{\mathrm{e}}^{\mathrm{T}}$, (c) the surface brightness $S^{(\mathrm{lobe,T})}$ of the diffuse thermal emission, (d) the surface brightness $S^{(\mathrm{lobe,NT})}$ of the diffuse non-thermal emission and, (e) the 1.5 GHz total intensity (Fomalont et al. 1989) from the center of the western lobe. The horizontal error bars are the region size calculated as the logarithmic mean of the major and minor axes of the ellipses (R1–R4), while the vertical error bars are 1 σ statistical uncertainty. The dotted horizontal line in (c) indicates the surface brightness of the Fornax cluster component $S^{(\mathrm{FC})}$ at the position of Fornax A as estimated from figure 5.19. The dotted curves in (c) and (e) show a fully-resolved (c) and PSF-convolved (e) radial profile of completely optically-thin emission of a filled sphere of a 12′ radius. While the dashed line in (c) show a sphere of a 12′ radius with a void sphere of a 8′ radius at the center (c).

thermal plasma, the $u_{\rm th}$ concentrates to the lobe center and decreases at the edge of the lobe. Comparing with the thermal plasma, we see that the energy density (=pressure) of non-thermal plasma slightly lower and more concentrated in the lobe center. It is notable that the energy density of the thermal plasma is comparable to the sum of energy densities of non-thermal electron and of magnetic field.

5.2.4 Comparison between the north and south halves

Here we compare the results between the northern and southern halves of the lobe. Figure 5.30 shows radial profiles of the derived physical parameters for north and south halves using the spectral fitting results for regions R1N–R4N and R1S–R4S. We recognize two remarkable differences between the northern and southern parts. First, the temperature of the thermal plasma of the northern lobe is $\sim$ 20% lower than that of the southern lobe, while the are constant in the northern lobe (figure 5.30a). Second, the non-thermal emission from the northern lobe is fairly dim, while that from the south half of lobe is very bright (figure 5.30d). Thus we suspect the hotter thermal plasma is related to the non-thermal (relativistic) electrons observed in the southern lobe.

Next, we calculated the energy densities for thermal and non-thermal plasma in the north and south halves using the same manner as § 5.2.2, 5.2.3. Resultant figure 5.33 showing the radial profiles of thermal, non-thermal electron, and magnetic field energy densities, indicates no difference in thermal energy densities in the north and south. This result strongly suggest thermal pressure balance between the two regions, in spite of the significant difference in temperature. Again we see the sum energy densities of non-thermal plasma and magnetic field is comparable to that of thermal plasma, even in the hot south region. In inner region of the southern lobe, the energy densities of electrons and magnetic field indicates an equitation, which supports that the non-thermal electron is not completely cooled but radiates its energy through the non-thermal emission processes.

5.2.5 Suggestions from the Results of Fornax A

Above results suggest that the southern half lobe, containing relative hot thermal plasma and relative high energy density non-thermal electrons, is still not relaxed but the north half has been relaxed. This strongly suggest younger south and older north portions of the lobe.

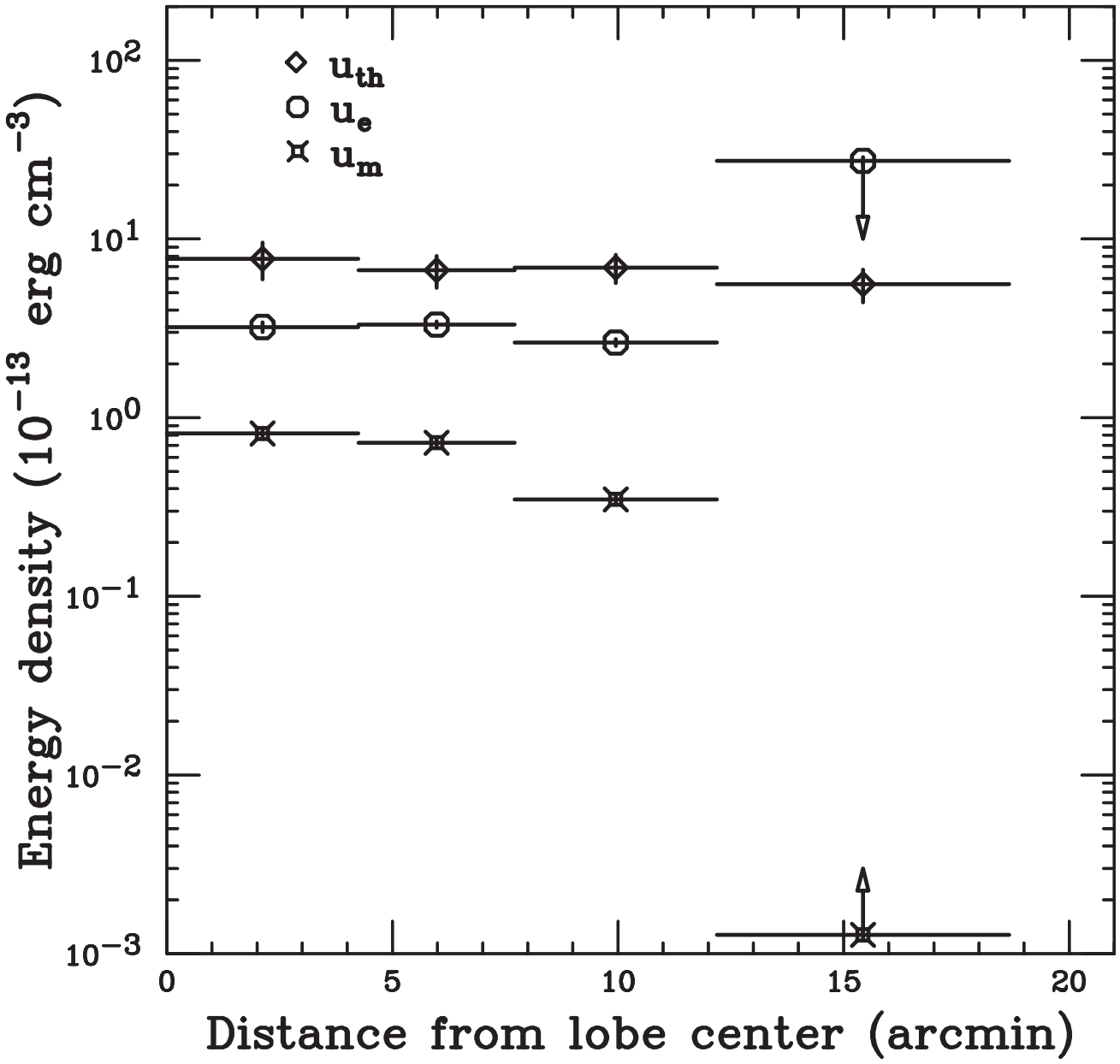

Figure 5.31: Radial profiles of the energy densities; thermal energy density ($u_{\rm th}$, diamonds), non-thermal electron energy density ($u_{\rm e}$, circles) and non-thermal magnetic energy density ($u_{\rm m}$, "x" shaped). The vertical label unit is erg cm^{-3}. These values are calculated using the spectral fit results of regions R1–R4. The vertical error bars are 1 σ statistical uncertainty.

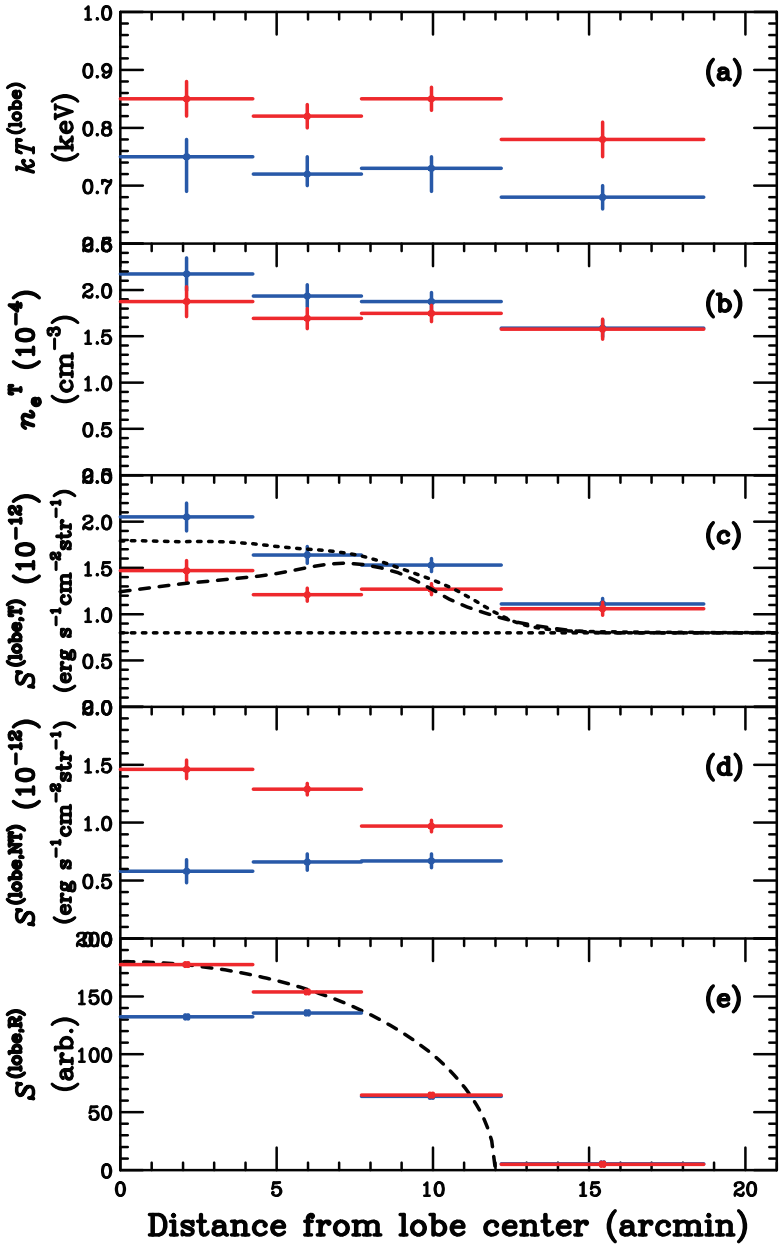

Figure 5.32: Radial profiles of the physical parameters for north (blue) and south (red) halves. These values are calculated using the spectral fit results of regions R1N–R4N and R1S–R4S. The symbols follow figure 5.30.

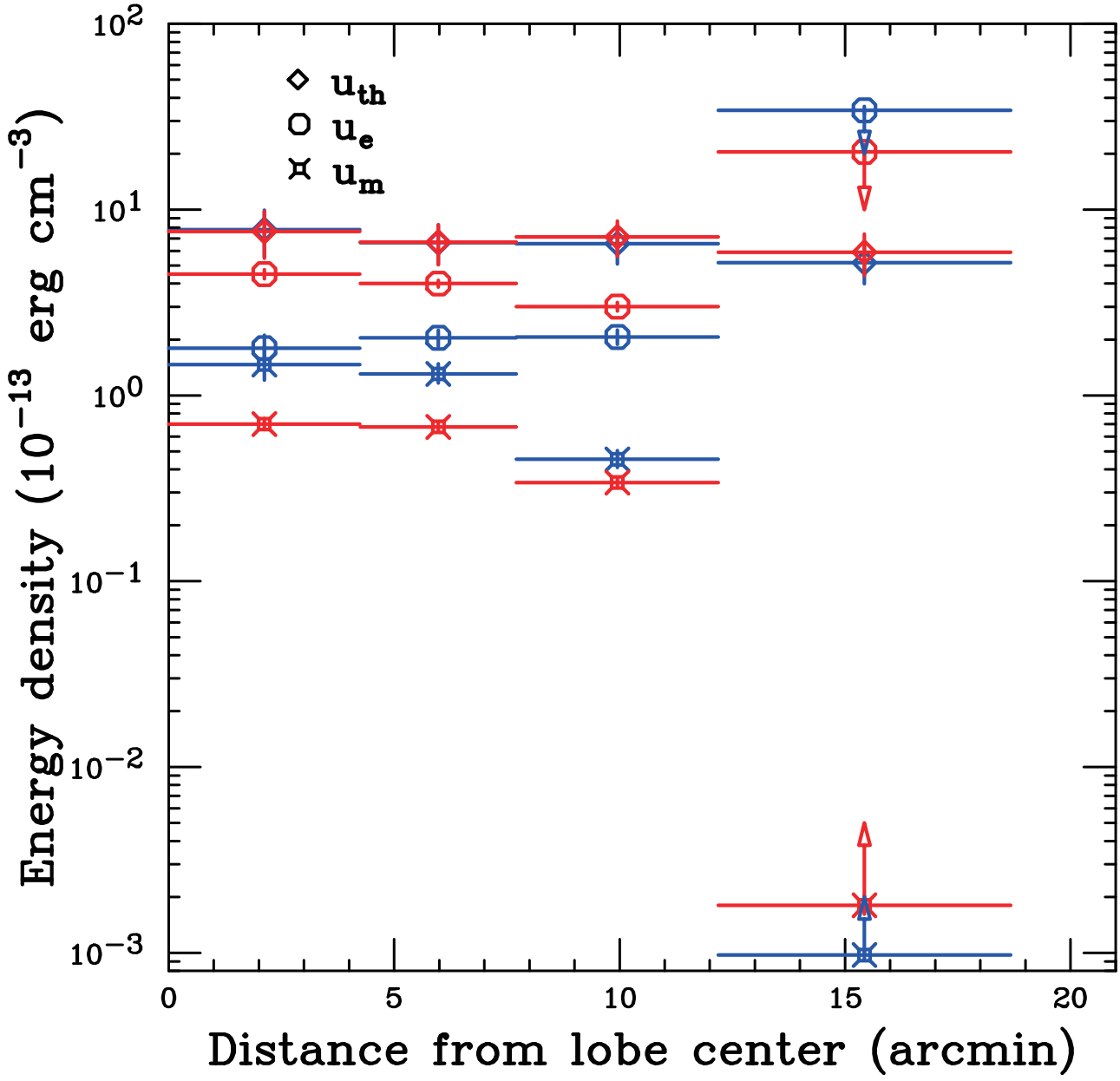

Figure 5.33: Radial profiles of the energy densities for north (blue) and south (red) halves. These values are calculated using the spectral fitting results of regions R1N–R4N and R1S–R4S. The symbols follow figure 5.31.

In addition, the radio polarimetry observation shows that the northern lobe has the uniform polarization, while the southern lobe has the filamentary structure, which inhibits local depolarizations (Fomalont et al. 1989). It is suggested that the region at the southern lobe is performed the turbulence of the plasma, which is activated by the jet recently. However, as indicate above, because the host galaxy NGC 1316 of Fornax A is dormant (Iyomoto et al. 1998), the jet is suggested to be inactive at present. According to the radio observations, the (dormant) jet from Fornax A was emitted in a direction toward the northern lobe (Geldzahler & Fomalont 1984).

How these observational results should be had interpreted? Here, we introduce a hypothesis that the jet had precessed between the northern and southern lobe and the nucleus of NGC 1316 became dormant after emitting the last jet toward the northern lobe. The north directed jet has not reached at the lobe region, and the latest electrons injected by the jet are still energetic in the southern lobe. We estimate the energy densities of the northern and southern lobes using the spectral fitting results from regions "MN" and "MS". The energy densities of the thermal emission of the northern and southern halves of the lobe are $u_{\rm th}^{N} = (7.09 \pm 1.53) \times 10^{-13}$ erg cm^{-3} and $u_{\rm th}^{S} = (7.01 \pm 1.52) \times 10^{-13}$ erg cm^{-3}, respectively. The energy densities of electron of the non-thermal emission of the northern and southern halves of the lobe are $u_{\rm e}^{N} = (2.03 \pm 0.17) \times 10^{-13}$ erg cm^{-3} and $u_{\rm e}^{S} = (4.09 \pm 0.14) \times 10^{-13}$ erg cm^{-3}, respectively. The energy densities of magnetic field of the non-thermal emission of the northern and southern lobe are $u_{\rm m}^{N} = (1.30^{+0.15}_{-0.12}) \times 10^{-13}$ erg cm^{-3} and $u_{\rm m}^{S} = (0.69 \pm 0.03) \times 10^{-13}$ erg cm^{-3}, respectively. Then we can derive the cooling time of thermal energy density of 4.5 Gyr to reduce the difference δu_{th} between $u_{th}^{\rm N}$ and $u_{th}^{\rm S}$. This is consistent with cooling time of non-thermal energy density of 1.8 Gyr, and supports the following interpretation. The jet had precessed between the north and south portions of the lobe and produced entire lobe region through the life of the jet activity. Within a few Gyr from present time, the latest had injected south portion of the lobe and then redirected to the north but has not injected to the north portion yet. After that, the nucleus has become inactive. Since the cooling time of thermal plasma (not difference between south and north) is as large as 75 Gyr, the historically layered thermal plasma filled the entire radio lobe. This interpretation will be examined by further observations including X-ray observation of the east lobe.

Chapter 6

Conclusion

We have studied the time-varying nature of the AGN jet using two completely different objects: OJ 287 of the binary super massive black hole and Fornax A of the radio lobe .

- From the differential view point using the binary super massive black hole OJ 287, we conclude followings.
  - We performed the observations of OJ 287 on the quiescent and the second flaring phase using Suzaku and broad band observatories. The second flaring phase observation is a first time.
  - The brightness of OJ 287 increased by a factor of 2 from the quiescent phase to the flaring phase. The X-ray spectrum of OJ 287 was harder in the flaring phase than in the quiescent phase.
  - Based on the synchrotron self-Compton model, the change of the multi-wavelength spectral energy distribution is interpreted as the increase of the electron energy density, without any notable change in either the magnetic field or the electron Lorentz factor.
  - Compared between the spectra of the first and second flaring phases of OJ 287, the jet and disk activity is varied periodically. The jet is interpreted to repeat to be a active and inactive phase in corporate with state transitions of the accretion disk.
- From the integral view point using the radio lobe Fornax A, we conclude followings.

- We performed Suzaku mapping observations of Fornax A with six pointings with an integrated exposure time of integrated exposure $\sim$ 300 ks.
- In this X-ray data analysis, we gave a considerable attention to estimation of several background. We estimate the levels of the NXB, Galactic halo, CXB, inter cluster medium, and point sources using Suzaku and XMM-Newton. With these efforts, the non-thermal emission was not only confirmed, thermal emission is but also discovered. In the center of the lobe, the 2–10 keV flux of the non-thermal emission is 0.25×10^{-12} erg s^{-1} cm^{-3}.
- We discovered the thermal emission distributed on the western lobe of Fornax A. The temperature and the 0.5–2 keV flux of the plasma are 0.78 keV and 4.3×10^{-12} erg s^{-1} cm^{-3}, respectively. Both of the temperature and flux are significantly higher than that of ambient environment.
- The feature of the distribution of the thermal plasma is not a shell-like structure but a spherical structure. The pressure of the thermal plasma is balance with the energy densities of a non-thermal emission in the lobe.
- We discovered the difference between the north and south halves in the lobe. In the south part, the temperature of the thermal plasma is higher than that of north part. The non-thermal flux in the south part is higher than that of the north part, which suggests more recent injection of jet to the southern portion of the lobe.

We interpret the jet activity combined with these results of OJ 287 and Fornax A. The two results described above, we revealed the dynamic state transitions of the AGN and the following the time-variation of the jet, from the differential and integral view points.

Bibliography

Abdo, A. A., Ackermann, M., Ajello, M., et al. 2009, *Astrophysical Journal*, 700, 597

Albert, J., Aliu, E., Anderhub, H., et al. 2008a, Nuclear Instruments and Methods in Physics Research A, 588, 424

Albert, J., Aliu, E., Anderhub, H., et al. 2007, *Astrophysical Journal Letter*, 666, L17

Albert, J., Aliu, E., Anderhub, H., et al. 2008b, *Astrophysical Journal*, 674, 1037

Alexander, P. 1987, *Monthly Notices of the Royal Astronomical Society*, 225, 27

Aliu, E., Anderhub, H., Antonelli, L. A., et al. 2009, Astroparticle Physics, 30, 293

Anders, E. & Grevesse, N. 1989, *Geochimica et Cosmochimica Acta*, 53, 197

ASCA Data Reduction Guide. 2011, ASCA Data Reduction Guide, http://heasarc.gsfc.nasa.gov/docs/asca/abc/abc.html

Bessell, M. S. 1979, *Publication of Astronomical Society of Pacific*, 91, 589

Boldt, E. 1987, in IAU Symposium, Vol. 124, Observational Cosmology, ed. A. Hewitt, G. Burbidge, & L. Z. Fang, 611–615

Ciprini, S. & Rizzi, N. 2008, in Blazar Variability across the Electromagnetic Spectrum

Croston, J. H., Kraft, R. P., Hardcastle, M. J., et al. 2009, *Monthly Notices of the Royal Astronomical Society*, 395, 1999

Ekers, R. D., Goss, W. M., Wellington, K. J., et al. 1983, *Astronomy & Astrophysics*, 127, 361

Fabian, A. C. 1994, *Annual Review of Astronomy and Astrophysics*, 32, 277

Fabian, A. C., Sanders, J. S., Allen, S. W., et al. 2003, *Monthly Notices of the Royal Astronomical Society*, 344, L43

Fabian, A. C., Sanders, J. S., Taylor, G. B., et al. 2006, *Monthly Notices of the Royal Astronomical Society*, 366, 417

Fanaroff, B. L. & Riley, J. M. 1974, *Monthly Notices of the Royal Astronomical Society*, 167, 31P

Feigelson, E. D., Laurent-Muehleisen, S. A., Kollgaard, R. I., & Fomalont, E. B. 1995, *Astrophysical Journal Letter*, 449, L149

Fiorucci, M. & Tosti, G. 1996, *Astronomy & Astrophysics Supplement*, 116, 403

Fomalont, E. B., Ebneter, K. A., van Breugel, W. J. M., & Ekers, R. D. 1989, *Astrophysical Journal Letter*, 346, L17

Fomin, V. P., Stepanian, A. A., Lamb, R. C., et al. 1994, Astroparticle Physics, 2, 137

Fossati, G., Maraschi, L., Celotti, A., Comastri, A., & Ghisellini, G. 1998, *Monthly Notices of the Royal Astronomical Society*, 299, 433

Fukazawa, Y., Mizuno, T., Watanabe, S., et al. 2009, *Publication of Astronomical Society of Japan*, 61, 17

Geldzahler, B. J. & Fomalont, E. B. 1984, *Astronomical Journal*, 89, 1650

Ghisellini, G., Celotti, A., Fossati, G., Maraschi, L., & Comastri, A. 1998, *Monthly Notices of the Royal Astronomical Society*, 301, 451

Giommi, P., Massaro, E., Chiappetti, L., et al. 1999, *Astronomy & Astrophysics*, 351, 59

Harris, D. E. & Grindlay, J. E. 1979, *Monthly Notices of the Royal Astronomical Society*, 188, 25

Harris, D. E. & Romanishin, W. 1974, *Astrophysical Journal*, 188, 209

Hillas, A. M. 1985, in International Cosmic Ray Conference, Vol. 3, International Cosmic Ray Conference, ed. F. C. Jones, 445–448

Hyodo, Y. 2009, Kyoto University

Idesawa, E., Tashiro, M., Makishima, K., et al. 1997, *Publication of Astronomical Society of Japan*, 49, 631

Ishida, M., e. a. 2007, Suzaku memo

Ishisaki, Y., Maeda, Y., Fujimoto, R., et al. 2007, *Publication of Astronomical Society of Japan*, 59, 113

Ishwara-Chandra, C. H. & Saikia, D. J. 1999, *Monthly Notices of the Royal Astronomical Society*, 309, 100

Isobe, N., Makishima, K., Tashiro, M., et al. 2006, *Astrophysical Journal*, 645, 256

Isobe, N., Seta, H., Gandhi, P., & Tashiro, M. S. 2011a, *Astrophysical Journal*, 727, 82

Isobe, N., Seta, H., & Tashiro, M. S. 2011b, *Publication of Astronomical Society of Japan*, 63, 947

Isobe, N., Tashiro, M., Sugiho, M., & Makishima, K. 2001, *Publication of Astronomical Society of Japan*, 53, 79

Isobe, N., Tashiro, M. S., Gandhi, P., et al. 2009, *Astrophysical Journal*, 706, 454

Iyomoto, N., Makishima, K., Tashiro, M., et al. 1998, *Astrophysical Journal Letter*, 503, L31

Jansen, F., Lumb, D., Altieri, B., et al. 2001, *Astronomy & Astrophysics*, 365, L1

Kaastra, J. S. 1992, An X-Ray Spectral Code for Optically Thin Plasmas., Tech. rep., SRON-Leiden

Kalberla, P. M. W., Burton, W. B., Hartmann, D., et al. 2005, *Astronomy & Astrophysics*, 440, 775

Kaneda, H., Tashiro, M., Ikebe, Y., et al. 1995, *Astrophysical Journal Letter*, 453, L13

Kataoka, J. 2000, Univ. of Tokyo

Kelley, R. L., Mitsuda, K., Allen, C. A., et al. 2007, *Publication of Astronomical Society of Japan*, 59, 77

Kidger, M. R. 2000, *Astronomical Journal*, 119, 2053

Kim, D.-W. & Fabbiano, G. 2003, *Astrophysical Journal*, 586, 826

Kim, D.-W., Fabbiano, G., & Mackie, G. 1998, *Astrophysical Journal*, 497, 699

Kokubun, M., Makishima, K., Takahashi, T., et al. 2007, *Publication of Astronomical Society of Japan*, 59, 53

Konami, S., Matsushita, K., Nagino, R., et al. 2010, *Publication of Astronomical Society of Japan*, 62, 1435

Konar, C., Hardcastle, M. J., Croston, J. H., & Saikia, D. J. 2009, *Monthly Notices of the Royal Astronomical Society*, 400, 480

Koyama, K., Tsunemi, H., Dotani, T., et al. 2007, *Publication of Astronomical Society of Japan*, 59, 23

Kushino, A., Ishisaki, Y., Morita, U., et al. 2002, *Publication of Astronomical Society of Japan*, 54, 327

Li, T.-P. & Ma, Y.-Q. 1983, *Astrophysical Journal*, 272, 317

Liedahl, D. A., Osterheld, A. L., & Goldstein, W. H. 1995, *Astrophysical Journal Letter*, 438, L115

Lumb, D. H., Warwick, R. S., Page, M., & De Luca, A. 2002, *Astronomy & Astrophysics*, 389, 93

Mewe, R., Gronenschild, E. H. B. M., & van den Oord, G. H. J. 1985, *Astronomy & Astrophysics Supplement*, 62, 197

Mewe, R., Lemen, J. R., & van den Oord, G. H. J. 1986, *Astronomy & Astrophysics Supplement*, 65, 511

Mitsuda, K., Bautz, M., Inoue, H., et al. 2007, *Publication of Astronomical Society of Japan*, 59, 1

Morrison, R. & McCammon, D. 1983, *Astrophysical Journal*, 270, 119

Nagai, H. 2006

Okumura, S. K., Momose, M., Kawaguchi, N., et al. 2000, *Publication of Astronomical Society of Japan*, 52, 393

Padovani, P. & Giommi, P. 1995, *Monthly Notices of the Royal Astronomical Society*, 277, 1477

Pursimo, T., Takalo, L. O., Sillanpää, A., et al. 2000, *Astronomy & Astrophysics Supplement*, 146, 141

Reber, G. 1944, *Astrophysical Journal*, 100, 279

Rolke, W. A., López, A. M., & Conrad, J. 2005, Nuclear Instruments and Methods in Physics Research A, 551, 493

Rosati, P., Tozzi, P., Giacconi, R., et al. 2002, *Astrophysical Journal*, 566, 667

Rybicki, G. B. & Lightman, A. P. 1979, Radiative processes in astrophysics, ed. Rybicki, G. B. & Lightman, A. P.

Serlemitsos, P. J., Soong, Y., Chan, K.-W., et al. 2007, *Publication of Astronomical Society of Japan*, 59, 9

Sillanpaa, A., Haarala, S., Valtonen, M. J., Sundelius, B., & Byrd, G. G. 1988, *Astrophysical Journal*, 325, 628

Sillanpaa, A., Takalo, L. O., Pursimo, T., et al. 1996a, *Astronomy & Astrophysics*, 305, L17

Sillanpaa, A., Takalo, L. O., Pursimo, T., et al. 1996b, *Astronomy & Astrophysics*, 315, L13

Skiff, B. A. 2007, VizieR Online Data Catalog, 2277, 0

Skrutskie, M. F., Cutri, R. M., Stiening, R., et al. 2006, *Astronomical Journal*, 131, 1163

Stickel, M., Fried, J. W., & Kuehr, H. 1989, *Astronomy & Astrophysics Supplement*, 80, 103

Strüder, L., Briel, U., Dennerl, K., et al. 2001, *Astronomy & Astrophysics*, 365, L18

Suzaku team. 2011, Suzaku technical discription, http://www.astro.isas.ac.jp/suzaku/doc/

Takahashi, T., Abe, K., Endo, M., et al. 2007, *Publication of Astronomical Society of Japan*, 59, 35

Takahashi, T., Kataoka, J., Madejski, G., et al. 2000, *Astrophysical Journal Letter*, 542, L105

Tashiro, M., Makishima, K., Iyomoto, N., Isobe, N., & Kaneda, H. 2001, *Astrophysical Journal Letter*, 546, L19

Tashiro, M. S., Isobe, N., Seta, H., Matsuta, K., & Yaji, Y. 2009, *Publication of Astronomical Society of Japan*, 61, 327

Tawa, N., Hayashida, K., Nagai, M., et al. 2008, *Publication of Astronomical Society of Japan*, 60, 11

Teshima, M. & The MAGIC Collaboration. 2008, The Astronomer's Telegram, 1500, 1

Turner, M. J. L., Abbey, A., Arnaud, M., et al. 2001, *Astronomy & Astrophysics*, 365, L27

Valtaoja, E., Teräsranta, H., Tornikoski, M., et al. 2000, *Astrophysical Journal*, 531, 744

Valtonen, M., Kidger, M., Lehto, H., & Poyner, G. 2008a, *Astronomy & Astrophysics*, 477, 407

Valtonen, M. J., Lehto, H. J., Nilsson, K., et al. 2008b, *Nature*, 452, 851

Valtonen, M. J., Nilsson, K., Sillanpää, A., et al. 2006, *Astrophysical Journal Letter*, 643, L9

Watanabe, M., Nakaya, H., Yamamuro, T., et al. 2005, *Publication of Astronomical Society of Pacific*, 117, 870

XMM-Newton Users Handbook. 2011, XMM-Newton Users Handbook

Acknowledgments

I had a precious time with many people throughout the five years as a graduate student. This thesis could not completed without their supports. I am deeply grateful to adviser Professor Makoto Tashiro, who triggered my interests to the X-ray astrophysics and the AGN jets as well as developing observation instruments. During my graduate course, I have experimented not only scientific data analysis, but also the development of a new X-ray instrument, X-ray microcalorimeter, which will be installed in the ASTRO-H satellite in the near future. It was a great opportunity to be able to participate in the project in such an interesting time. I also appreciate Naoki Isobe for introducing me the basics and detailed research on AGN jets.

For the multi-wavelength data presented in this thesis, I appreciate Kouichiro Nakanishi, Tomoka Tosaki, Kotaro Kohno, Yoshito Shimajiri, and Masayuki Fukuhara, for their great effort in obtaining radio data at NMA. In the optical observation using the Kanata telescope, I appreciate Makoto Uemura, Mahito Sasada, and Akira Arai. I also thank Lindfors Elina for kindly providing the data obtained with the KVA telescope. In the γ-ray observations using MAGIC, I appreciate Masaaki Hayashida, Masahiro Teshima and the MAGIC collaboration team. Masaaki Hayashida also gave many useful comments for my thesis work.

I express appreciation to all the members of our laboratory. I appreciate Associate Professor Yukikatsu Terada for giving lots of advice for data analysis and experiments. I also appreciate Keiichi Abe, Kaori Onda, Akira Endo, and Yuichi Yaji, whom I deeply respect as my preceding researchers. I thank Natsuki Kodaka and Kouichi Morigami, who are precious friends of mine. Among members of our laboratory, Wataru Iwakiri, Tomomi Kouzu, and Atsushi Harayama spend a long time to discuss about difficult problems of astrophysics. Yuya Shimoda, Shu Koyama, and Tetsuya Yasuda supported me in writing this thesis. With all the members of laboratory, I really enjoyed the research.

Lastly, I appreciate my family, who continued supporting me even in hard time. Thanks to my father for driving me back home from the university sometimes at midnight. Thanks to my mother for caring about me every day. Thanks to my sisters Kyoko and Sachiyo for helping me many times. Thanks to my family pets: Kizu, Uri, Tomakku, and Hakku for being very well. Thanks to Masahiro for giving an enormous amount of supports.